Title

Single-molecule 3D imaging of human plasma intermediate-density lipoproteins reveals a polyhedral structure

Journal

Biochimica et Biophysica Acta (BBA) - Molecular and Cell Biology of Lipids, 1864(3)

ISSN

1388-1981

Authors

Lei, Dongsheng
Yu, Yadong
Kuang, Yu-Lin
et al.

Publication Date

2019-03-01

DOI

10.1016/j.bbalip.2018.12.004

Peer reviewed

BBA - Molecular and Cell Biology of Lipids 1864 (2019) 260–270

Contents lists available at ScienceDirect

BBA - Molecular and Cell Biology of Lipids

journal homepage: www.elsevier.com/locate/bbalip

Single-molecule 3D imaging of human plasma intermediate-density lipoproteins reveals a polyhedral structure

Dongsheng Lei[a,1], Yadong Yu[a,1], Yu-Lin Kuang[b], Jianfang Liu[a], Ronald M. Krauss[b], Gang Ren[a,*]

[a] The Molecular Foundry, Lawrence Berkeley National Laboratory, Berkeley, CA 94720, USA
[b] Atherosclerosis Research, Children's Hospital Oakland Research Institute, Oakland, CA 94609, USA

ARTICLE INFO

Keywords:
3D structure
Intermediate-density lipoprotein
Cryo-electron microscopy
Individual-particle electron tomography
IPET

ABSTRACT

Intermediate-density lipoproteins (IDLs), the remnants of very-low-density lipoproteins via lipolysis, are rich in cholesteryl ester and are associated with cardiovascular disease. Despite pharmacological interest in IDLs, their three-dimensional (3D) structure is still undetermined due to their variation in size, composition, and dynamic structure. To explore the 3D structure of IDLs, we reconstructed 3D density maps from individual IDL particles using cryo-electron microscopy (cryo-EM) and individual-particle electron tomography (IPET, without averaging from different molecules). 3D reconstructions of IDLs revealed an unexpected polyhedral structure that deviates from the generally assumed spherical shape model (Frias et al., 2007; Olson, 1998; Shen et al., 1977). The polyhedral-shaped IDL contains a high-density shell formed by flat surfaces that are similar to those of very-low-density lipoproteins but have sharper dihedral angles between nearby surfaces. These flat surfaces would be less hydrophobic than the curved surface of mature spherical high-density lipoprotein (HDL), leading to a lower binding affinity of IDL to hydrophobic proteins (such as cholesteryl ester transfer protein) than HDL. This is the first visualization of the IDL 3D structure, which could provide fundamental clues for delineating the role of IDL in lipid metabolism and cardiovascular disease.

1. Introduction

Lipoproteins are molecular complexes that transport neutral lipids (cholesteryl esters and triglycerides) between tissues through the blood aqueous environment [4]. Human lipoproteins can be classified into high-density lipoproteins (HDLs), low-density lipoproteins (LDLs), intermediate-density lipoproteins (IDLs), very-low-density lipoproteins (VLDLs), and chylomicrons [5–8] based on their decreasing hydrated density in ultracentrifugation. All of these lipoproteins are composed of a central neutral lipid core and an outer shell of free cholesterol, phospholipids, and apolipoproteins [4]. Different lipoproteins utilize different apolipoproteins as scaffolds. Specifically, HDL primarily utilizes apolipoprotein A-I (apoA-I) as its scaffold protein; LDL, IDL and VLDL all use apolipoprotein B-100 (apoB-100, one of the largest proteins with molecular mass of ~550 kDa) as their major scaffold protein. IDL and VLDL also contain other proteins, including apolipoprotein Cs and E (with molecular mass of < ~10 kDa and ~34 kDa respectively) [9]. Chylomicrons contain apoB-48, i.e., the N-terminal 48% of apoB-100. IDLs, which are cholesterol-enriched VLDL lipolytic remnants, have been reported to be an independent risk factor for cardiovascular disease (CVD) [10,11]. In plasma, a portion of the IDL can be removed by LDL receptors on the liver surface, while other IDLs undergo further lipolysis to form LDLs [12,13]. Moreover, IDLs accumulate cholesteryl esters (CEs) from HDLs with the help of CE transfer protein (CETP) [14]. The directional CE transfer from HDL to IDL may be related to the directional interaction of CETP with lipoproteins, i.e., the hydrophobic N-terminal distal end of CETP predominantly interacts with HDL [15]. However, it is still undetermined whether the hydrophobic N-terminal distal end of CETP prefers to interact with HDL rather than IDL due to a higher level of surface hydrophobicity [16]. Electron microscopy (EM) studies showed that i) smaller HDL particles bind higher amounts of CETP; ii) the amount of CETP bound can be greater than the number of copies of apoA-I in HDL, e.g., five CETP molecules can be observed on the surface of a recombinant HDL that contains three apoA-Is,

Abbreviations: 3D, three-dimensional; CE, cholesteryl ester; CETP, cholesteryl ester transfer protein; CVD, cardiovascular disease; EM, electron microscopy; ET, electron tomography; FSC, Fourier shell correlation; HDL, high-density lipoprotein; IDL, intermediate-density lipoprotein; IPET, individual-particle electron tomography; LDL, low-density lipoprotein; TEM, transmission electron microscopy; VLDL, very-low-density lipoprotein

* Corresponding author.
E-mail address: gren@lbl.gov (G. Ren).
[1] These authors contributed equally to this work.

https://doi.org/10.1016/j.bbalip.2018.12.004
Received 16 January 2018; Received in revised form 25 November 2018; Accepted 9 December 2018
Available online 14 December 2018

suggesting a protein-lipid interaction mechanism, but not excluding a co-existent protein-protein interaction via either or both N and C-terminal distal ends of CETP [16]. There may also be binding involving lipoprotein surface oligosaccharides. However, IDL has a lipid surface similar to HDL, but with larger diameter. It is possible that the CETP N-terminal end binds to the IDL surface, but with less binding affinity.

Although there is pharmacological interest in IDL for prevention and treatment of CVD and for understanding the lipid-transferring mechanism of CETP, the three-dimensional (3D) structure of IDL is still unclear to date. The complex composition and wide size variation of IDLs (diameters ranging from 23 to 30 nm [17,18]) have led to great challenges in studying their 3D structure via traditional structural biology methods, such as X-ray crystallography, nuclear magnetic resonance, and cryo-electron microscopy (cryo-EM) single-particle reconstruction. This is because these methods need either crystallization or a highly homogeneous particle structure, which are both challenging for lipoproteins. Although recent progress in single-particle reconstruction [19] has made it possible to study the 3D structures of particles with multiple different conformations, it is challenging to apply this method for studying IDL particles which can vary in size and protein or lipid composition.

To explore the 3D structure and structural dynamics of IDL, we imaged human plasma IDL particles by using cryo-electron tomography (cryo-ET), and then reconstructed their 3D density maps from each individual IDL particle by using individual-particle electron tomography (IPET) method [20]. To verify the observed 3D structural features of IDLs, we also imaged them under different temperatures (below and above the phase transition temperature of IDL core lipid), and obtained 3D reconstructions of IDLs bound with an anti-apoB-100 antibody. The results show that IDLs have a polyhedral shape which deviates from the generally assumed spherical shape model [1–3]. This information gives fundamental clues for further studies of IDL function and interaction with other proteins, such as CETP.

2. Results

2.1. Two-dimensional (2D) imaging of IDL particles by cryo-EM

An IDL sample from a healthy person was examined by cryo-EM techniques. The survey of cryo-EM micrographs (Fig. 1A) showed evenly distributed particles. Further examination (Fig. 1B) indicated that these particles vary greatly in size, ranging from 20 to 30 nm in diameter. Notably, in contrast to the generally held belief that IDLs are spherical emulsion-like particles [1–3], the particles, especially the smaller ones, displayed an angular shape with distinguishable surface vertices (indicated by arrows in Fig. 1A and B). The angular shape would be more likely to be observed by the cryo-EM technique with greater resolution than negative staining [21]. The consistency of IDL shape with the angular shape observed for VLDL [22] indicates that IDLs may have a polyhedral 3D shape similar to that of VLDL.

To verify that the observed angular shape is an intrinsic structural character of IDL instead of an artifact due to the crystallization of lipids in the IDL core (the IDL sample was frozen from 4 °C, which is below the lipid phase transition temperature of ~20 °C to ~40 °C), we repeated the above 2D imaging experiment using IDL samples frozen from ~40 °C to 45 °C, which is above the lipid phase transition temperature. The freezing process is so rapid (the temperature drops down in the order of 10^4 to 10^5 K/s) that the water molecules have insufficient time to form crystals, but are in an amorphous state [23,24]. It is reasonable to believe that the lipid molecules in IDL would unlikely have sufficient time to undergo phase transition, especially considering the phase transition time of lipids in the range from milliseconds to seconds time scale, such as ~2 s for dipalmitoyl phosphatidylcholine (DPPC) [25].

The cryo-EM micrographs of the IDL sample frozen at temperatures above the lipid phase transition temperature (Fig. 1C and D) essentially show the same particle diameter range (from 20 to 30 nm) and confirm the angular morphologies observed above (Fig. 1A and B). Moreover, the angular shape is also more significant among smaller-size particles. The consistent observations in these experiments suggest that the angular shape is not an artifact arising from crystallization of the lipid core but an intrinsic structural character of IDL.

According to measured surface angles and particle diameters from ~760 IDL particles, the surface angle of an IDL particle is in general linearly distributed with respect to particle diameter. By dividing particle size into four groups (20–22, 22–24, 24–26, and 26–28 nm), the average size of the smallest surface angle in each group was found to be ~79.4 ± 12.4°, ~76.4 ± 9.5°, ~72.1 ± 9.3° and ~69.8 ± 9.6°, respectively (Fig. 1E). This linear relationship can also be observed for VLDL in a recent TEM study [22]. The larger surface angles observed for IDL compared to those observed for VLDL indicate that IDL is more angular than VLDL (Fig. 1E). Taking the data points (surface angle vs particle diameter) of IDL and VLDL together, an overall negative linear relationship between surface angle and particle diameter was found, i.e., Angle = −0.77 × (Diameter, in nanometer) + 92.

2.2. 3D reconstruction of individual IDL particles by IPET

The 2D imaging analysis described above shows that IDLs are very heterogeneous in size and are thus not appropriate targets for single-particle 3D reconstruction. We therefore chose the IPET technique [20] to obtain 3D density maps of individual IDL particles.

For IPET 3D reconstruction, the IDL cryo-EM sample was imaged from a series of tilt angles ranging from −60° to 60° in 3.0° increments at a magnification of 50 k× (each pixel corresponds to 0.24 nm) (Fig. 2A) using a Zeiss Libra 120 cryo-TEM equipped with Gatan UltraScan 4 K × 4 K CCD. After contrast transfer function (CTF) correction of the tilt images, particles were picked out from images and then submitted to IPET 3D reconstruction, in which image alignments were iteratively refined to achieve an ab initio 3D density map (no human involved initial model was used). Only particles whose overall shape was visible through the entire tilt range were selected. The step-by-step refinement procedure and the intermediate results of a representative IDL particle are shown in Fig. 2B. The final 3D density map of this particle was achieved at a 3D resolution of ~9.7 nm based on Fourier shell correlation (FSC) and a criterion of 0.5 (Fig. 2E; details are provided in the Materials and methods section). This map (low-pass filtered at 8.0 nm) shows a polyhedral-shaped particle with a diameter of ~26 nm (Fig. 2C, and D). Furthermore, the particle has an outer shell whose density is higher than that of the core, as shown by the slices of the final map at different heights (Fig. 2F and G). The average thickness of the shell is ~3 nm, which is similar to that of a phospholipid monolayer (for example, a thickness of ~2.5 nm for DPPC [26]). However, the thickness of the shell appears uneven, even after the density map was low-pass filtered at 8.0 nm. The uneven thickness of the shell may be related to the distribution of protein on IDL surface.

IPET processing was performed for a total of 16 IDL particles (Fig. 2, **Supplementary Figs. S2–S15**, Supplementary Video 1, Supplementary Table 1). The second 3D density map is presented (Fig. 2H–M). This particle was selected because it was also visible in raw tilt images (Fig. 2H, left panel). As in the reconstruction of the first particle, the alignment of tilt images of the second IDL particle was iteratively refined by using IPET to achieve an ab initio 3D density map (Fig. 2H). The final map at a 3D resolution of ~9.6 nm showed that this particle is ~27 nm in diameter and is also polyhedral as for the first IDL particle (Fig. 2I and J). Moreover, the slices of the final map at different heights (Fig. 2L and M) confirm the presence of a low-density core and a high-density polyhedral shell in the IDL.

A total of 16 density maps were obtained for 16 individual IDL particles. Seven representative maps are displayed in increasing order of sizes in Fig. 2N. Each map shows a polyhedral shape (Fig. 2N) formed by generally flat faces. To better represent the observed polyhedral shapes, we modeled these maps as polyhedrons. The polyhedrons were

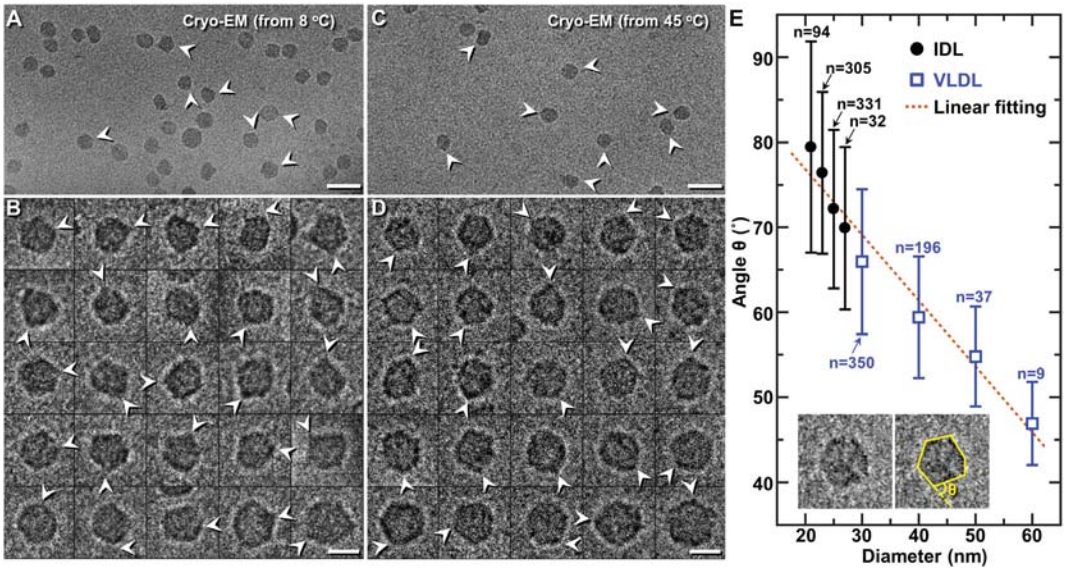

Fig. 1. Cryo-EM images of IDL particles. (**A**) A survey cryo-EM image of IDL, which was incubated at 8 °C before plunge-freezing. (**B**) 25 representative IDL particles at 8 °C. (**C**) A survey cryo-EM image of IDL, which was incubated at 45 °C before plunge-freezing. (**D**) 25 representative IDL particles at 45 °C. Arrowheads indicate the vertices on the IDL particles. (**E**) ~760 IDL particles at 8 °C were separated into 21-, 23-, 25-, and 27-nm-diameter groups (n = number of particles in each group). The average smallest surface angles of IDLs in each group are ~79, 76, 72, and 70°, respectively. The error bars represent the standard deviations. By combining previous data points of VLDL (shown in blue) [22], the surface angle was shown to have a negative linear relationship to particle diameter (angle = −0.77 × diameter (in nanometer) + 92). The inset shows one representative IDL particle and how its circumference and the smallest surface angle θ were identified. Survey images of A and C were high-pass filtered at 400 nm. Particle images in B and D were band-pass filtered between 1 and 40 nm. Scale bars: 50 nm in A and C; 20 nm in B and D.

determined by following protocol: i) markers were manually placed on the density map to represent vertices, ii) the vertices were then connected to represent the edges between neighboring flat faces, and iii) the edges were finally grouped to represent the flat faces (Fig. 2O). In this process, the edges with a dihedral angle (between flat faces forming the edge) larger than 20° were all measured for analysis. The obtained models have ~9–12 flat faces, and a few of the neighboring faces form dihedral angles near 90°. Notably, the density around the edges was generally higher than that within the flat surface (Fig. 2P and Q). Considering that protein is the highest-density component within an IDL particle, the spatial distribution of high densities may reflect the structure of the apolipoprotein(s) contained within IDL.

2.3. 3D reconstruction of individual IDL-antibody complexes by IPET

To confirm that the observed polyhedral-shaped particles are IDL which uses apoB-100 as its scaffold protein, we selected an anti-apoB-100 antibody (mAB012) as a first antibody used to determine apoB-100 location by incubating it with the IDL sample, and then examined the IDL-antibody mixture using cryo-EM to test the binding of the antibody to the polyhedral particles.

The survey of cryo-EM micrographs of the IDL-antibody mixture showed the existence of angular-shaped particles (Fig. 3A), as was observed in the IDL alone samples. Zoomed-in (magnified) views of these particles show that the smaller particles have more highly angular shapes (Fig. 3B), consistent with the morphology of IDL that is not bound to antibody. More importantly, some angular-shaped particles appear to be attached to a Y- or rod-shaped density whose dimensions are similar to those of the antibody (Fig. 3C). The results confirm that these angular-shaped particles contain apoB-100, as expected for IDLs, and suggest that IDLs maintain their polyhedral 3D structure after binding to antibody.

To further verify that antibody-bound IDLs maintain their polyhedral 3D structure, 3D reconstructions of IDL-antibody complexes were performed. Again, due to the structural heterogeneity of the complexes, the IPET method was used to reconstruct the 3D density map of individual IDL-antibody complexes as performed above for IDL particles alone.

Cryo-EM samples of the IDL-antibody mixtures were imaged at a series of tilt angles from −60 ° to 60 ° in 1.5 ° increments (Fig. 4A) by an FEI Tecnai TF20 cryo-TEM equipped with a Gatan K2 Summit direct electron detection camera. The tilt images were acquired at a magnification of 19 k× (each pixel corresponds to 0.19 nm) and a total dose of ~90 $e^-/Å^2$. IPET 3D reconstruction was performed on CTF-corrected images followed by iterative alignment refinement to achieve a final ab initio 3D density map. The particles were screened to include only those in which the bound antibody was visible throughout the entire tilt series (Fig. 4B, left panel). The step-by-step refinement procedures and the intermediate results for the first IDL-antibody complex are shown in Fig. 4B. The final 3D density map was generated at a 3D resolution of ~6.7 nm based on FSC analysis and a criterion of 0.5 (Fig. 4E). The final map (low-pass filtered at 8.0 nm) shows a polyhedral-shaped particle (diameter of ~27 nm) with a Y-shaped protrusion (length of ~12 nm) (Fig. 4C and D). The polyhedral-shaped particle is IDL, and the Y-shaped protrusion is considered to be the bound antibody. Furthermore, this IDL is also composed of a low-density core and a high-density shell (Fig. 4F and G), as observed for IDL particles without antibody.

By repeating the above IPET process, a second 3D density map of an IDL-antibody complex was reconstructed (Fig. 4H–M). The final 3D density map at a 3D resolution of ~6.2 nm shows that the second complex is a polyhedral-shaped particle (diameter of ~27 nm) with a ~16-nm-long protrusion (Fig. 4I and J).

A total of seven density maps were reconstructed from seven representative individual IDL-antibody complexes, in which the anti-apoB-100 antibodies shown as the protrusions on surfaces of each complex confirmed that the polyhedral-shaped particles contained apoB-100 (Fig. 4N, **Supplementary Figs. S16–S20**, Supplementary Video 1, Supplementary Table 1). The polyhedral-shaped particles have similar sizes to that of IDL-alone particles (Fig. 2), and the smaller particles show sharper surface angles (Fig. 4O), consistent with the observed morphology of antibody-free IDLs.

The protrusions on polyhedral-shaped IDLs were ~12–17 nm long

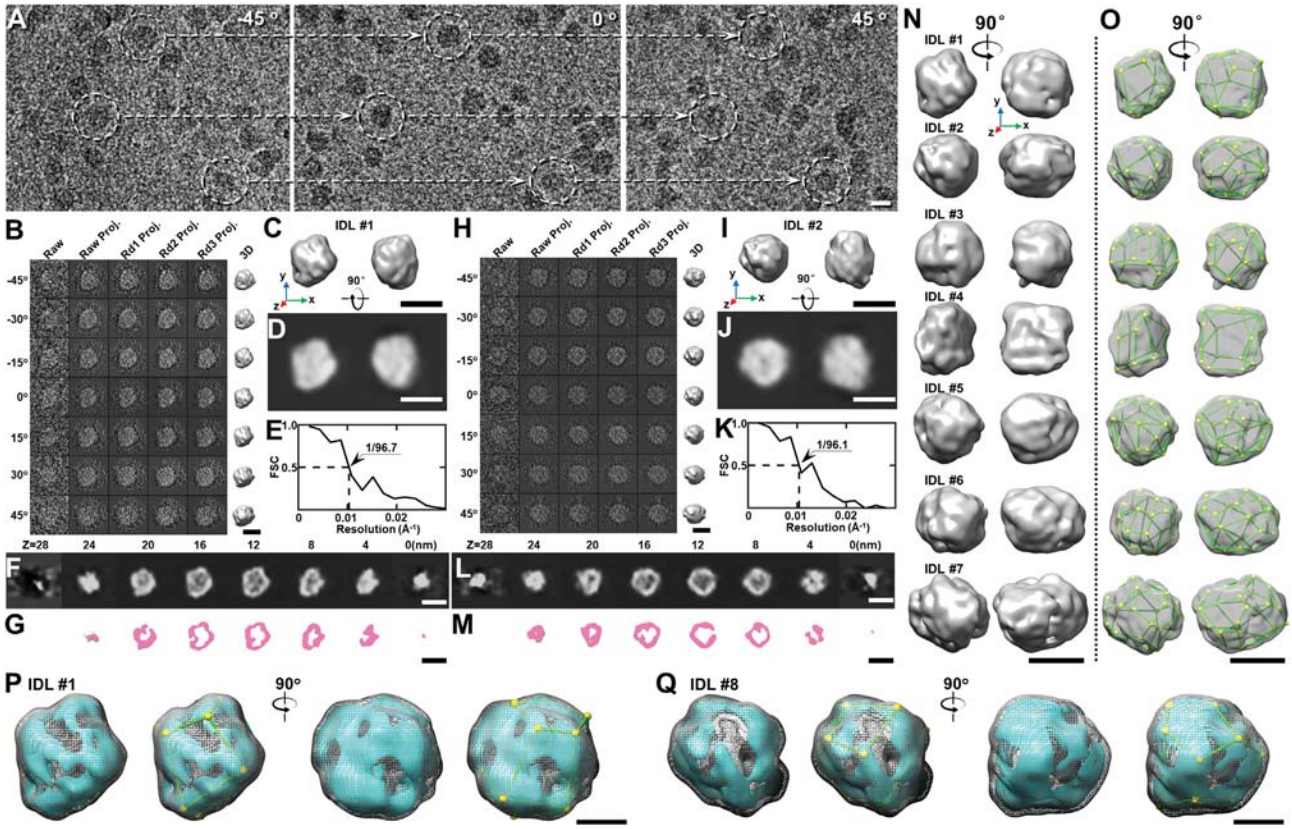

Fig. 2. 3D reconstruction of IDL particles by IPET. (**A**) The IDL cryo-EM sample was imaged from a series of tilt angle for 3D reconstruction (band-pass filtered between 2 and 400 nm). (**B**) The tilt images (after CTF correction) of the first targeted individual IDL particle were gradually aligned to a common center via an iterative refinement process to achieve a 3D reconstruction by using IPET. Representative tilt images (image contrast reversed), projections of the raw, intermediate, and final 3D reconstruction of the particle at seven tilt angles are displayed. (**C**) Two orthogonal views of the final 3D reconstruction (low-pass filtered at 8 nm). (**D**) 2D projections of final 3D reconstruction in the same view directions as in subfigure C. (**E**) The resolution of the IPET 3D density map was ~9.7 nm by FSC analyses (based on two density maps reconstructed from odd- and even-numbered tilt images). (**F**) Projection of slices of the 3D map at different Z heights. (**G**) Iso-surface of slices of the 3D map at different Z heights. (**H–M**) IPET 3D reconstruction of the second IDL particle. (**N**) 3D density maps of seven representative IDL particles. (**O**) The same maps as shown in N overlapped with polyhedral models, which represent the overall shape of these particles. (**P**) The 3D density map of the first IDL particle displayed at two different contour levels (high contour level in cyan surface and low contour level in gray mesh). The high contour map represents high-density components in IDL, such as the apolipoproteins. (**Q**) The 3D density map of another representative IDL particle. Scale bars: 20 nm in A through O; 10 nm in P and Q.

and were invariably perpendicular to the IDL surface. Considering that these protrusions are likely to correspond to antibodies, it seems that their estimated 3–4 nm thickness is not resolved by the map, whose resolution is ~5.5–6.5 nm. The reasons for observation of the antibody have been discussed in a previous IPET study of VLDL [22], i.e., i) the resolution from FSC analysis is likely underestimated, ii) the definition of resolution from FSC analysis is different from that of standard resolution, iii) visualizing a single object is easier than distinguishing two nearby points.

The locations at which polyhedral-shaped IDLs bind anti-apoB-100 antibodies gave us potential information about the location of apoB-100 on IDL. The 3D maps of IDL have shown that the edges of IDL particles have highest densities and are likely where apoB-100 is located (Fig. 2P and Q). Consistently, the 3D maps of IDL-antibody complexes show that IDL only bound antibody through its edges or vertices, but not faces (two representative IDL-antibody complexes are shown in Fig. 4P and Q). These results confirm that apoB-100 is located at the edges of polyhedral-shaped IDLs and the faces of IDLs are mainly composed of lipids.

2.4. 3D reconstruction of individual IDL-antibody-IDL complexes by IPET

As an antibody, mAB012, can bind two IDL particles simultaneously, the antibody can be used as a marker to identify the IDL through antibody-antigen interactions (Fig. 5A). To further confirm the observed IDL-antibody-IDL complexes seen in 2D micrographs, 3D density maps of individual IDL-antibody-IDL complexes were reconstructed by IPET as described above for IDL-antibody complexes.

The tilt images of a representative targeted IDL-antibody-IDL complex were iteratively aligned by using IPET to achieve an ab initio 3D density map (Fig. 5B). This particle was selected since the two IDLs are visible in raw tilt images at low tilt angles (Fig. 5B, left panel); the antibody is barely visible in several tilt images. The final 3D density map was generated at a 3D resolution of ~6.1 nm based on FSC analysis and a criterion of 0.5 (Fig. 5E). The map (low-pass filtered at 8.0 nm) shows two polyhedral-shaped particles of diameter ~27 nm bridged by a Y-shaped particle with a length of ~14 nm (Fig. 5C). The polyhedral-shaped particles, the Y-shaped particle, and their binding were all further verified by the 2D projections of the final map (Fig. 5D).

A total of three density maps were obtained from three individual IDL-antibody-IDL complexes (Fig. 5, **Supplementary Figs. S21–S22**, Supplementary Video 1, Supplementary Table 1). These maps all show two polyhedral-shaped particles bridged by a Y- or a rod-shaped density (Fig. 5F and G). The Y- or rod-shaped densities always appear to be bound to polyhedral-shaped particles and to be oriented in a direction perpendicular to the particles, as for the antibodies bound to IDL in the IDL-antibody complexes described above.

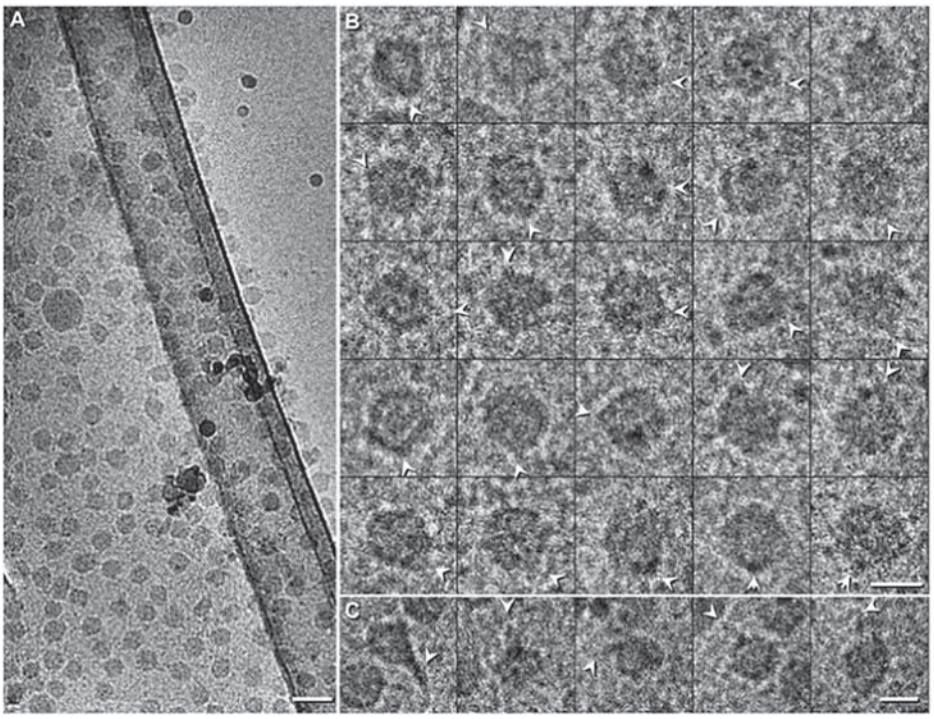

Fig. 3. Cryo-EM images of IDL-antibody mixture. (**A**) A survey cryo-EM image of the IDL-antibody mixture (high-pass filtered at 400 nm). Particles were unevenly distributed in vitreous ice. Zoom-in views of these particles show (**B**) 25 representative polyhedral-shaped particles and (**C**) five representative particles with Y- or rod-shaped protrusions (antibody). Particle images were band-pass filtered between 1 and 400 nm. Arrowheads indicate the vertices on the particles in B, and the protrusions in C. Scale bars: 50 nm in A; 20 nm in B and C.

2.5. 3D reconstruction of individual antibodies by IPET

Despite the previous successful application of IPET to the study of the 3D structures of various proteins, it is not clear whether small proteins such as antibodies can be reconstructed using IPET based on cryo-ET data. During the validation of IPET reconstruction using IMOD (details in the Discussion section), we observed that individual antibodies could be seen in the IMOD reconstruction. However, most antibodies displayed a rod shape rather than the generally accepted Y-shape. To check the resolution capability of IPET and validate the 3D structure of individual antibodies, we also used IPET to obtain 3D reconstructions of individual antibodies.

By repeating the above IPET 3D reconstruction, the tilt images of individual antibodies (low-pass filtered at 1 nm) were submitted to IPET 3D reconstruction (Fig. 5J). The final 3D density map was achieved by IPET at a resolution of ~6.0 nm (Fig. 5M). The map filtered at 8.0 nm shows an ~17 nm Y-shaped particle (Fig. 5K and L). One arm of the Y-shaped particle is positioned some distance from the other two arms, allowing us to measure its diameter as ~8 nm. The observed particle shape, particle size and domain size all agree with those reported for antibodies, suggesting that this Y-shaped particle is an antibody.

To further confirm the resolution capability of IPET, four additional individual antibodies were also processed by IPET 3D reconstruction (**Supplementary Figs. S23–S26**, Supplementary Video 1, Supplementary Table 1). Four of the five obtained reconstructions show a clear Y-shape (Fig. 5N). Only one reconstruction resembled an overall L shape; this may be due to the high flexibility of antibody structure. To further test the consistency of these reconstructions with known antibody structure, an antibody model (the crystal structure of human immunoglobulin G1, PDB entry 1HZH [27]) was flexibly docked into the reconstructions. The docking shows that the overall size and shape of the reconstructions are consistent with the structure of immunoglobulin G1 (Fig. 5O). It should be noted that during docking, the two domains of reconstruction with similar size and less spherical shape ("L-" or "8-" shape) were treated as F_{ab} domains, considering that F_{ab} domains may become larger and less spherical due to glycosylation. Although we are not completely confident about this treatment, it should not change the basic result. These results confirm that IPET is able to capture structural features of small particles in cryo-ET.

The above experiments suggest that the observed IDL-antibody-IDL complexes are formed through the binding of an antibody molecule to two IDL particles simultaneously rather than by nonspecific interactions. Furthermore, the observation of IDL-antibody-IDL complexes indirectly suggests that the antibody used for labeling IDL was still functional and visible in 3D.

3. Discussion

By using cryo-EM, cryo-ET and IPET techniques, we examined human plasma IDL particles under various conditions, i.e., above and below the phase transition temperature of lipid, and in the presence and absence of bound antibody. The TEM images showed that IDL is highly heterogeneous in both size and shape. The 3D density maps of individual IDL particles, IDL-antibody complexes, and IDL-antibody-IDL complexes all suggested that IDLs have a polyhedral 3D structure, and this is an intrinsic structural character of IDL which would not be affected by temperature and antibody binding. Besides, this structural character is more significant among small IDLs than large IDLs.

3.1. Polyhedral shape of IDL

The cryo-EM images at above the phase transition temperature of IDL showed that the polyhedral nature of IDL was not related to the crystallization of lipids in the IDL core. However, it may still be questioned whether the high temperature specimen was being properly held above the phase transition temperature prior to vitrification or whether a phase-transition could occur during the actual vitrification process.

To confirm that the specimen was being held above the transition temperature before entering the liquid ethane bath instead of i) rapid evaporative cooling of the specimen during incubation at our humidity of 80%, and/or ii) the tip of the tweezer holding the grid may lead to specimen cooling, we used a thermometer to measure the temperature of the chamber, the tweezer, the EM grid and the specimen (sample solution) under our experimental conditions, e.g. 80% humidity under the setting temperatures of 45 °C and 8 °C respectively. The experiments

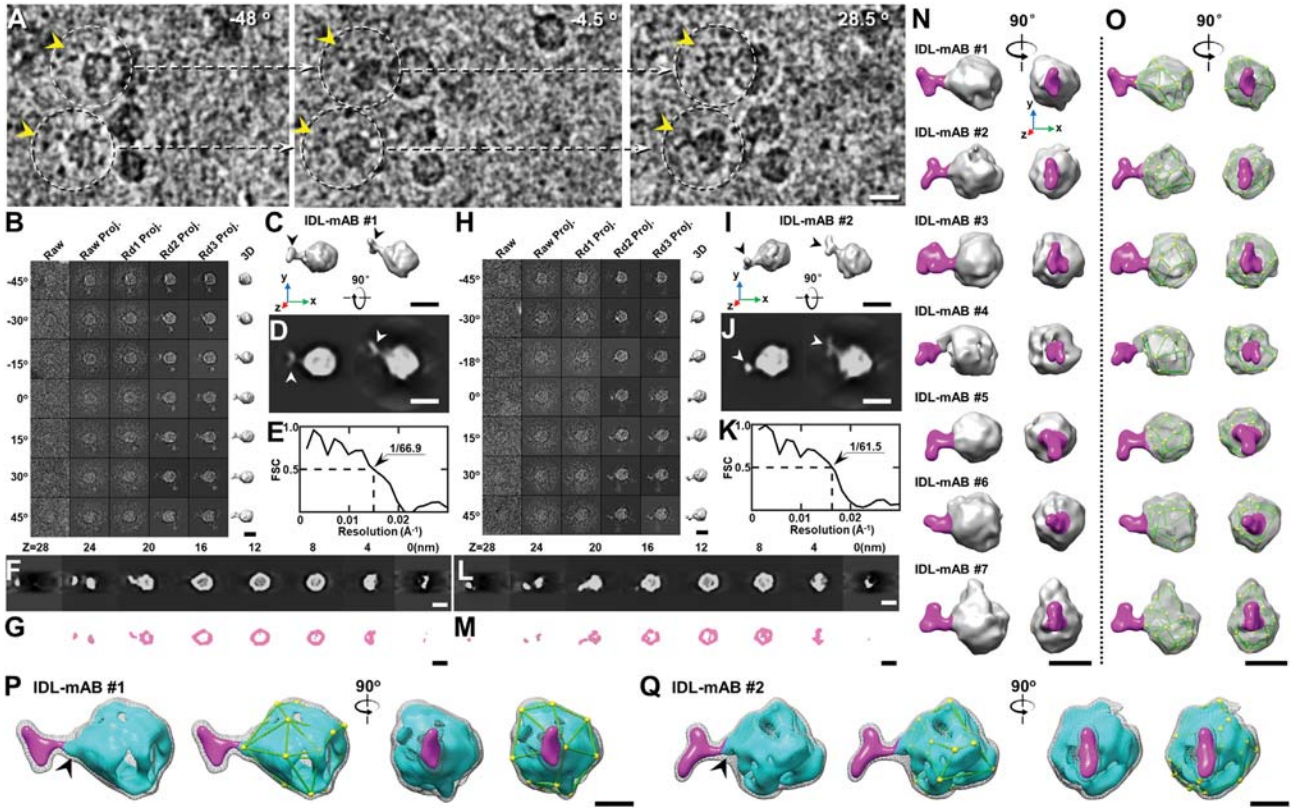

Fig. 4. 3D reconstruction of IDL-antibody complexes by IPET. (**A**) The IDL-antibody cryo-EM samples were imaged from a series of tilt angles for 3D reconstruction (band-pass filtered between 5 and 150 nm). (**B**) The tilt images (after CTF correction) of the first targeted IDL-antibody complex were gradually aligned to a common center via an iterative refinement process to achieve a 3D reconstruction by using IPET. Representative tilt images (image contrast reversed), projections of the raw, intermediate, and final 3D reconstruction of the particle at seven tilt angles are displayed. (**C**) Two orthogonal views of the final 3D reconstruction (low-pass filtered at 8 nm); the arrow indicates the antibody. (**D**) 2D projections of final 3D reconstruction in the same view directions as in subfigure C. (**E**) The resolution of the IPET 3D reconstruction was ~6.7 nm by FSC analyses (based on two density maps reconstructed from odd- and even-numbered tilt images). (**F**) Projection of slices of the 3D map at different Z heights. (**G**) Iso-surface of slices of the 3D map at different Z heights. (**H–M**) IPET 3D reconstruction procedure of the second IDL-antibody complex. (**N**) 3D density maps of seven IDL-antibody particles. (**O**) The same maps as shown in N overlapped with polyhedral models, which represent the overall shape of the IDLs. The densities arising from the antibody are shown in pink. (**P**) The 3D density map of the first IDL-antibody complex displayed at two different contour levels (high contour level in cyan surface and low contour level in gray mesh); the antibody portion is shown in pink. The high contour map represents the high-density components in IDL, such as the apolipoproteins. (**Q**) The 3D density map of the second IDL-antibody complex. Scale bars: 20 nm in A through O; 10 nm in P and Q.

showed that the measured temperatures of the chamber, tweezer, EM grid and the specimen (sample solution) were 46.2 °C, 45.6 °C, 43.2 °C and 42.2 °C, respectively when the setting chamber temperature was 45 °C and the humidity was 80% (**Supplementary Fig. S27**). In comparison, when the setting chamber temperature was 8 °C and the humidity was 80%, the measured temperatures of the chamber, tweezer, EM grid and specimen (sample solution) were 7.9 °C, 7.9 °C, 7.5 °C and 7.3 °C, respectively (**Supplementary Fig. S28**). The temperature variation was within ~6–8% of the setting temperature. These experiments confirmed that the chamber can, indeed, hold the sample temperature at above phase transition temperature prior to vitrification.

During the process of vitrification, the freezing of sample solution is sufficiently rapid to prevent lipid phase-transition based on our sample preparation protocol that has been well tested by others, including the structural changes in dengue virus which was captured when the specimen was incubated at 37 °C by cryo-EM [28,29]. This is because the sample temperature drops down to liquid nitrogen temperature within milliseconds (in the order of 10^4 to 10^5 K/s) during the freezing process. As a result, the water molecules do not have sufficient time to form crystals, but are rather in an amorphous state [23,24]. The starting temperature of the samples, ~42 °C to 45 °C, is significantly above the phase transition temperature of IDL, which should be similar to the phase transition temperature of LDL, 28–33 °C [30,31]. The phase transition time for lipid is in the range from milliseconds to seconds [32,33], such as ~2 s for dipalmitoyl phosphatidylcholine (DPPC) [25], but could even be minutes or hours to have transition fully completed on cooling [34]. The transition time is significantly longer than the freezing process. It is reasonable to believe that the lipid molecules in IDL would be unlikely to have sufficient time to undergo phase transition. Moreover, previous cryo-EM studies based on synthetic lipid vesicles showed the phase transition phenomena could not occur during the cryo-EM specimen process due to the short time scale of sample cooling and vitrification (< 1 ms) [35]. Thus, the polyhedral nature of IDL was not related to the crystallization of lipids in the IDL core.

3.2. Validation of IPET 3D reconstruction

Cryo-ET has shown its capability to achieve 3D reconstruction with resolution beyond 2 nm by sub-volume averaging, such as in the studies of the 26S proteasome [36] and the nuclear pore complex [37]. Although the averaging increases the resolution of 3D reconstruction by reducing noise and filling the missing wedges, it could also average away the flexible portions of an imaged structure. Thus, in the study of flexible proteins, 3D reconstruction based on individual protein particles represents a fundamentally more advanced technique.

To verify our 3D reconstructions obtained using IPET, another widely used software, IMOD [38], was used to perform 3D reconstruction using the same IDL-antibody cryo-ET data that were used

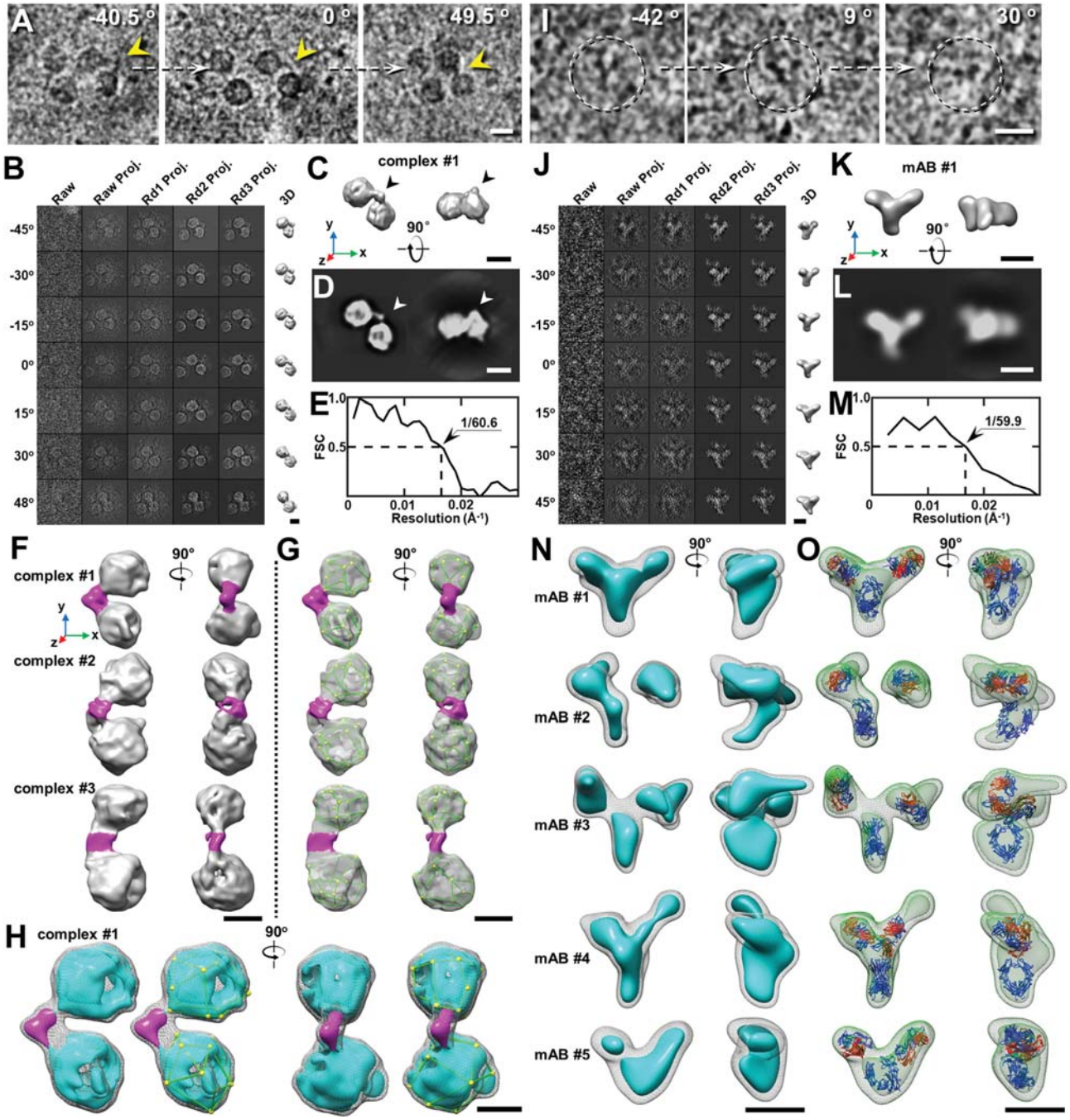

Fig. 5. 3D reconstruction of IDL-antibody-IDL complexes and antibodies alone by IPET. (**A**) Three representative views of the tilt series of an IDL-antibody cryo-EM sample showing IDL-antibody-IDL complexes (band-pass filtered between 2 and 400 nm). Arrows indicate the antibody. (**B**) The tilt images (after CTF correction) of the first targeted IDL-antibody-IDL complex were submitted to IPET reconstruction. Seven representatives tilt images (image contrast reversed) of this particle, and corresponding projections of the raw, intermediate, and final 3D reconstruction are displayed. (**C**) Two orthogonal views of the final 3D reconstruction (low-pass filtered at 8 nm). (**D**) 2D projections of final 3D reconstruction in the same view directions as in subfigure C. (**E**) The resolution of the IPET reconstruction was ~6.1 nm by FSC analyses (based on two density maps reconstructed from odd- and even-numbered tilt images). (**F**) 3D density maps of three IDL-antibody-IDL particles. (**G**) The same maps as shown in F overlapped with polyhedral models, which represent the overall shape of the IDLs. The densities arising from the antibody are shown in pink. (**H**) 3D density map of one representative IDL-antibody-IDL complex displayed at two different contour levels (high contour level in cyan and low contour level in gray); the antibody portion is shown in pink. (**I**) Three representative views of a targeted antibody particle. (**J–M**) The procedure of IPET 3D reconstruction of the antibody particle. (**N**) 3D density maps of five antibody particles displayed at two different contour levels (high contour level in cyan surface and low contour level in gray mesh). (**O**) These antibody density maps flexibly docked with the crystal structure of human immunoglobulin G1 antibody; the heavy and light chains are shown in blue and orange, respectively. Scale bars: 20 nm in A through I; 10 nm in J through O.

in IPET. The final IMOD 3D reconstruction (**Supplementary Fig. S1B**, low-pass filtered at 10.0 nm) and the 2D projection of the final 3D (**Supplementary Fig. S1A**, low-pass filtered at 2.0 nm) both validate the existence of IDLs. Among ~40 IDL particles, ~75% were bound with Y- or rod-shaped antibodies (the IDL:antibody molar ratio was 1:2.3). The observation of IDL and IDL-antibody complexes also by using the third party software IMOD confirms the capability of IPET for 3D reconstruction of individual IDLs and IDL-antibody complexes.

Although the IMOD 2D projection (**Supplementary Fig. S1A**) and 3D reconstruction (**Supplementary Fig. S1B**) also showed the angular-shaped IDL particles as observed in the IPET 3D reconstructions and projections, zoom-in views of those particles' 3D reconstructions show the quality of the 3Ds is relatively low. As a result, we had to low-pass filter at 10 nm in order to show the 3D structure. Besides, a significant missing-wedge artifact can be observed on the IMOD 3D reconstructions (**Supplementary Fig. S1C to S1F**). The results suggest that the IPET 3Ds have a higher resolution/quality than those from IMOD because the IPET 3D is more consistent with the raw micrographs. The capability of IPET 3D reconstructions was also validated with other macromolecules, including antibodies [39,40], CETP bound to liposomes [16], VLDL alone and VLDL bound to antibody [22], 84-base-pair double-stranded DNA [41], DNA origami [42], contactin-associated protein-like 2 alone and its complex with contactin 2 [43], and neurexin 1α [44]. Our success in obtaining higher-resolution 3D reconstruction of single proteins may be a benefit from a unique strategy in our IPET method, i.e., using local small-sized images rather than large whole micrographs for 3D reconstruction, which could reduce the alignment error due to image distortion [20].

Before IPET 3D reconstruction, the CTF of 2D tilt series was corrected by TOMOCTF software [45], in which phase flipping was used based on the strip-wise tilt-aware method. The phase flipping method is a typical and safe option for CTF correction that has been used for a long period in cryo-EM and cryo-ET [46,47], and that can avoid the enhancement of noise and generation of the strong high resolution artifacts by using a large B-factor in the amplitude correction option during CTF correction [48]. It was suspected that the observed polyhedral shape and high-density shells of IDL were related to the amplitude corrections. We therefore conducted the CTF amplitude correction on the IDL-antibody raw images. The raw images of two representative particles in Fig. 4 were submitted for amplitude correction by the Wiener filter under two parameters of 0.5 and 0.25 using TOMOCTF software [45], in which the parameters should avoid noise-overshooting as suggested in the program. The images after amplitude correction showed a similar image contrast to that of the phase flipped ones, but looked noisier (**Supplementary Figs. S29 and S30**). More importantly, the IPET 3D reconstructions showed that the density maps were nearly identical to those without CTF amplitude corrections (Fig. 4). The polyhedral shape and high-density shells of IDL were still clear and well maintained. These results suggest that the amplitude correction did not provide additional benefit to the image and 3D reconstruction in our case.

Notably, the above TOMOCTF amplitude correction was only conducted on the spatial frequencies beyond the first maximum of the CTF [45]. One could still question whether the uncorrected amplitude of low frequencies impact the result significantly. An accurate CTF correction on the low-resolution amplitude is impossible theoretically. This is because the amplitude of CTF at low resolution significantly overlaps the amplitude of the central electron beam (including non-scattering beam), which generates the highest amplitude and image background. Although the CTF at low-resolution turns to zero, the overlap causes the low resolution amplitude to be higher than any of the maximal peaks of CTF. As a result, a perfect CTF correction by multiplying by the reciprocal of the low resolution CTF would infinitely weight the background and reduce the image contrast. The effects of the central beam can be roughly reduced by high-pass filtering, but cannot be eliminated completely.

To demonstrate the effect of the low-resolution amplitude on the 3D reconstruction, we conducted the following three tests. The first test was to reduce the contribution of the low-resolution amplitude via high-pass filtering on the 2D images at the first maximum of the CTF (green lines in **Supplementary Figs. S31A and S32A**). In this case, both the contribution of the center beam and the CTF effects on the low-resolution amplitude were mostly eliminated (green lines in **Supplementary Figs. S31C and S32C**). Although the particles in the filtered 2D images were nearly invisible (third columns in **Supplementary Figs. S31B and S32B**), the 3D reconstructions showed that the polyhedral shape and high density shell were still remained though they became weaker (third column in **Supplementary Figs. S31D and S32D**). The densities of the surface binding antibody (shown in the pink color) and core neutral lipids were enhanced.

The last two tests were to enhance the contribution of the low-resolution amplitude at two levels via manipulating the low-resolution amplitudes by two curves respectively, i.e., the reciprocal of the low resolution averaged CTF and its square root (the blue and yellow lines in **Supplementary Figs. S31A and S32A**). The 2D images showed that, although the particle contrasts were enhanced, the background became uneven (**Supplementary Figs. S31B and S32B**). The 3D reconstruction from the images multiplied by the square root of the reciprocal of the low resolution averaged CTF (**Supplementary Figs. S31A–B and S32A–B**) showed the polyhedral shapes of IDLs were still maintained and the high densities were still presented in the shell (fourth columns in **Supplementary Figs. S31D and S32D**). However, the density of the binding antibody became weaker. The existence of antibody on the surface of IDLs had been confirmed by the raw 2D images and 3D reconstruction of IMOD. By further increasing the low-resolution amplitude (blue lines in **Supplementary Figs. S31C and S32C**) via multiplying the image amplitudes by the reciprocal of low resolution averaged CTF (blue lines in **Supplementary Figs. S31A and S32A**), the background of the 2D images turned more uneven (last columns in **Supplementary Figs. S31B and S32B**). Although the polyhedral shape and the high density shell were still barely maintained in the 3D reconstructions, the densities of the binding antibody became even weaker and nearly invisible (last columns in **Supplementary Figs. S31D and S32D**). These results suggest that correction of the low resolution CTF amplitude can also increase the amplitude of the center beam and background. The enhancement of central beam contribution can eliminate the density of the binding antibody. Thus, the usage of low-resolution amplitude correction needs caution. In brief, based on above tests we believe that the polyhedral shape and high-density shells are intrinsic structural features of IDL, instead of low resolution CTF artifacts.

3.3. Polyhedral structure of IDL and VLDL

The 3D reconstructions obtained in this study show that IDL displays a polyhedral structure that is similar to the previously observed structure of VLDL [22]. Moreover, smaller IDL and VLDL are predominantly polyhedral, as suggested by the negative linear relationship between the surface angles and the diameters of IDL and VLDL, i.e., angle $= -0.77 \times$ (diameter) + 92.

The smaller IDLs or VLDLs are, the more polyhedral they are. In theory, a spherical object has the smallest surface for a given volume. If we reduce the core volume, but maintain the surface area, the particle would become more edgy, so that the smaller particles would be more edgy. Similarly, as IDLs and VLDLs become smaller due to the loss of core lipids during lipolysis but maintain their surface areas, they become increasingly polyhedral. Otherwise, a gap between the IDL core and its surface would be formed, which is an unrealistic conformation in the aqueous environment of the blood. Considering that the edge has high density, apoB and other apolipoproteins, such as apoE and apoCs, are more likely to be located at the edges of IDL particles.

The above theoretical prediction is based on an assumption that the surface area of protein in IDL is maintained when particle size changes. This assumption is not always fulfilled, because the apolipoproteins in IDL may undergo conformational changes or glycosylation, or even be removed during lipolysis. To address this problem and get a better understanding of IDL structure, future studies using multiple antibodies or mass-spectroscopy are needed to identify the presence and location of all proteins in IDLs during lipolysis.

3.4. IDL surface structure and its potential biological relevance

The 3D reconstructions of IDL obtained in this work show that the flat surfaces of polyhedral-shaped IDLs are relatively lower in density than the edges. Based on our 3D reconstructions of IDL-antibody complexes, it is the edge, not the surface, of IDL that binds to anti-apoB-100 antibody mAB012. These results suggest that the apolipoproteins of IDL are mainly located on the edges, while the flat surfaces of IDLs are mainly formed by lipids.

The lipids on a flat surface would have less hydrophobic portions (fatty acid chains) exposed to the aqueous environment than lipids on a curved surface. On the other hand, the amphipathic apolipoproteins at the edges of IDLs could protect the hydrophobic edges of flat lipid surfaces from the aqueous environment. As a result, our proposed model for IDL surface structure, i.e., flat lipid monolayer surfaces wrapped by apolipoprotein edges, is an energetically preferred model in the plasma compared with models with curved lipid monolayers or lipid bilayers.

Considering that with greater surface curvature, the more hydrophilic phospholipid-charged head groups are farther apart and the more inner hydrophobic portions of lipids are exposed to solution [49], the flat lipid surfaces of IDL are less hydrophobic than the curved lipid surfaces. The spherical form of mature HDL (after cholesterol esterification by lecithin cholesterol acyltransferase), the majority of plasma HDL, has been reported repeatedly [15,50–56]. Therefore, IDL would have weaker binding affinity than HDL with hydrophobic proteins. This hypothesis is consistent with previous TEM observations wherein the N-terminal distal end of CETP, which is hydrophobic, binds to HDL, while the C-terminal distal end of CETP, which is less hydrophobic, binds to VLDL, IDL or LDL [15,16,57]. Considering smaller HDL binds more CETP molecules than large HDL [16], which suggests that CETP binds HDL via protein-lipid interaction, this hypothesis indicates that the CETP N-terminal end binds directionally to HDL via hydrophobic interactions with the HDL lipid surface. The directional binding of CETP to lipoproteins could facilitate the directional transfer of CE from HDL to LDL, IDL or VLDL. Moreover, this hypothesis is also consistent with the finding that the majority of CETP in plasma is bound with HDLs, possibly related to the higher hydrophobicity of HDL than other lipoproteins. Future studies of the detailed organization of lipids and proteins on lipoprotein surfaces are needed to confirm the hydrophobic interaction between the CETP N-terminal end and lipoproteins, and to determine whether additional protein-protein interactions are required for the directional binding of the CETP C-terminal end.

IDL is presumably a precursor of LDL; however, LDL has been shown to have a discoidal shape [58] and thus appears to have an entirely different structure from that of IDL. It remains unclear how such a structural transformation could occur and how different apolipoproteins play roles in this transformation. One possibility is that the IDLs that form LDL have a different structure. As far as we know, no such intermediate between IDL and LDL has been observed in plasma, possibly because in the steady state these particles have already been converted to LDL. In that case, the IDL observed in this study would represent remnants that are more slowly cleared; these remnants may not be the precursors of classical LDL. Individuals with very high LDL levels may accumulate IDL precursors in plasma due to LDL receptor clearance defects; if so, their IDL particles might present an appearance that differs from that of the IDL particles found in normal individuals. Thus, future study of IDLs from individuals with very high LDL levels is warranted. Comparison of this type of IDL with normal IDL and LDL, especially their protein composition, could provide fundamental clues to uncovering the mechanism of IDL reshaping.

In this study, we explored the 3D structure of IDL by reconstructing the 3D density maps from each individual IDL particle and IDL-antibody complex using the IPET technique. The results show that IDL particles have a polyhedral shape, and are composed of low-density cores and high-density shells. The shell is formed by several flat surfaces connected by high density edges. The edges, but not the surface, bound with anti-apoB-100 antibody, suggesting the IDL surface is composed of flat lipids framed by amphipathic apolipoproteins. The polyhedral-shaped IDL has a structure similar to that of VLDL, consistent with a precursor-product relationship. However, both VLDL and IDL differ significantly in structure from the commonly accepted discoidal shape of LDL, and contain more apoE and apoCs than those present in LDL, and thus the structural changes that accompany the formation of LDL from VLDL and IDL precursors will require future study.

4. Materials and methods

4.1. IDL and antibody

Human IDLs were isolated from the plasma of a healthy individual by non-equilibrium density gradient ultracentrifugation at 40,000 rpm for 6 h at 17 °C in a Beckman SW41 rotor [17]. Mouse monoclonal antibody mAB012, whose epitope is located within the first 20 N-terminal residues of human apoB-100, was obtained from Chemicon (EMD Millipore Corporation, CA, USA). The antigen-antibody complex was then prepared by incubating IDLs and mAB012 in a molar ratio of 1:2.3 at 4 °C overnight.

4.2. Preparation of cryo-EM specimens

Cryo-EM samples of IDL and IDL-antibody mixture were prepared using a Leica EM GP plunge freezer (Leica, Buffalo Grove, IL, USA) equipped with a chamber for controlling the temperature and humidity during sample preparation. Prior to specimen preparation, the IDL sample was pre-incubated at temperatures below (8 °C) and above (45 °C) the lipid phase transition temperature (from ~20 to 40 °C) in a water bath for at least 30 min. The temperature of the plunge-freezer chamber was pre-set to the pre-incubation temperature, and the relative humidity was maintained at 80%. During specimen preparation, an aliquot (~3 μL) of pre-incubated IDL or IDL-antibody mixture solution (molar ratio 1:2.3) was applied to a glow-discharged lacey carbon grid (LC200-Cu, Electron Microscopy Sciences, Hatfield, PA, USA). The grid was flash-frozen after blotting by filter paper, and finally transferred to liquid nitrogen for storage.

4.3. Cryo-EM un-tilted data acquisition

Cryo-EM un-tilted images were acquired by using a Zeiss Libra 120 Plus TEM (for IDL and IDL-antibody mixture) and a FEI Tecnai TF20 TEM (IDL-antibody mixture). On the Zeiss Libra 120 Plus TEM which was operated at 120 kV high tension, the images were acquired at a magnification of 50 k× (each pixel corresponds to 0.24 nm) using a Gatan UltraScan 4 K × 4 K CCD and an in-column energy filter. A 75-μm-diameter condenser aperture was used to select only the central portion of the electron source, and a 50-μm-diameter objective aperture was used to increase micrograph contrast. On the FEI Tecnai TF20 TEM which was operated at 200 kV high tension, the images were acquired at a magnification of 19 k× (each pixel corresponds to 0.19 nm) using a Gatan K2 Summit direct electron detection camera.

4.4. Cryo-ET data acquisition

Tilt image series of IDL cryo-EM samples were collected from −60° to +60° in 3° increments using a Zeiss Libra 120 Plus TEM (Carl Zeiss NTS) equipped with an in-column energy filter and a Gatan UltraScan 4 K × 4 K CCD. During data acquisition, the Gatan tomography module (Gatan Inc., Pleasanton, CA, USA) operated in Advanced Tomography mode was used to track the specimen and maintain defocus at ~2.0 μm. The acquired tilt image series at magnification of 50 k× (each pixel corresponds to 0.24 nm) represents a total dose of ~60 $e^-/Å^2$.

Tilt image series of IDL-antibody mixture cryo-EM samples were collected from −60° to +60° at 1.5° increments on an FEI Tecnai TF20 TEM equipped with a Gatan K2 Summit direct electron detection camera. During data acquisition, the UCSF Tomography software package was used to automatically track the specimen and maintain defocus at ~7 μm. The acquired tilt image series at magnification of 19 k× (each pixel corresponds to 0.19 nm) represents a total dose of ~90 $e^-/Å^2$.

4.5. IPET 3D reconstruction

The acquired tilt image series were first aligned using IMOD [38]. CTF correction was then performed via TOMOCTF [45]. A subregion was extracted from the full-size tilt series to generate a particle tilt series that contained only a single particle. "Focused" 3D reconstruction was performed on the particle tilt series to alleviate the effects due to image distortion, tilt-axis variation, and tilt angle offset. In the IPET reconstruction [20], the particle tilt series was first back-projected into an ab initio 3D density map as the initial model. The refinement was then iteratively applied to improve the translational alignment of each tilted particle image to the computed projection. During the refinement, automatically generated Gaussian low-pass filters, soft-boundary circular masks and particle-shaped soft-boundary masks were sequentially employed to suppress noise around the particle. An improved model was then reconstructed based on the refined alignment at the end of each refinement. The 3D density map was reconstructed by Fourier-space back-projection (without weighting). Post-3D reconstruction processing was conducted to estimate the data in the missing wedge using our newly developed algorithm (manuscript in preparation). All obtained density maps were low-pass filtered at 8 nm using EMAN [59] and displayed using UCSF Chimera [60].

The resolution of 3D reconstructions was estimated by FSC analysis of two reconstructions that were separately generated using the odd- and even-numbered images of the aligned particle tilt series. Note that the generation of the FSC curve did not take into account the missing wedge since the missing data were estimated in our approach. The frequency where the FSC valve first drops to 0.5 was used to define the resolution of the IPET reconstruction. We used the 0.5 FSC criterion because this method, which is used to determine the resolution of single-particle reconstruction, gave lower resolution than other criteria.

4.6. Building of IDL surface model

To better present the overall polyhedral shape of IDL particles, each IDL particle was simplified to a polyhedron model. The protocol for building up these models is as follows: i) manually place markers on the surface of the density map (low-pass filtered at 8.0 nm) to represent vertices, ii) connect the vertices to represent the edges between flat faces of particle, and iii) finally group the edges to represent the flat faces. In this process, the edges with dihedral angles larger than 20° (angle between two nearby flat faces forming the edge) were identified.

4.7. Validation of IPET 3D reconstruction

IMOD [38], a widely used tomography 3D reconstruction program, was used to reconstruct the IDL-antibody tomography. In the absence of gold nanoparticles, fiducial markers were generated using the patch tracking function of IMOD. Based on these markers, images were aligned until achieving accuracy better than 1.3 nm. The aligned images were then submitted to weighted back-projection in IMOD to construct a 3D tomogram.

4.8. Docking of antibody model

To estimate the consistency between antibody density maps reconstructed by IPET and the structure of antibody mAB012, we docked an antibody model into the density maps. The crystal structure of human immunoglobulin G1 (PDB entry 1HZH [27]), which is the same class of antibody as mAB012, was chosen as the initial model. The F_{ab} and F_c domains of the model were then separately docked into the density map envelope. During docking, the two domains of the density map that have similar size and shape (an "L-" or "8-" shape, less spherical than the other domain) were treated as F_{ab} domains.

Supplementary data to this article can be found online at https://doi.org/10.1016/j.bbalip.2018.12.004.

Contributions

This project was initiated by RMK, YK and GR. YY prepared the TEM samples. YY, DL, JL and GR acquired the data. DL, YY, JL and GR processed the data and performed the IPET 3D reconstructions. DL and YY drafted the initial manuscript, which was revised by DL, YY, YK, JL, RMK and GR.

Competing financial interests

The authors declare no competing financial interests.

Transparency document

The Transparency document associated with this article can be found, in online version.

Acknowledgments

We would like to thank Drs. Shawn Zheng, Michael Braunfeld and David Agard of the University of California, San Francisco for their support in cryo-EM data acquisition and motion correction of K2 images. We also thank Dr. Changyu Huang for the assistant in the temperature measurement experiments, and Dr. Jinping Li and Mr. Thomas Gregory Horton for comments and editing. This material is based upon work that was supported by the National Science Foundation under Grant DMR-1344290. Work at the Molecular Foundry was supported by the Office of Science of the Office of Basic Energy Sciences of the U.S. Department of Energy under Contract No. DE-AC02-05CH11231. G.R. is supported by the National Heart, Lung, and Blood Institute of the National Institutes of Health (no. R01HL115153) and the National Institute of General Medical Sciences of the National Institutes of Health (no. R01GM104427).

Additional information

Correspondence and requests for materials should be addressed to G.R.

Data deposition

The cryo-ET 3D density maps are available in the EM data bank as EMD-9069 to 9084 (for IDL particles), EMD-9085 to 9091 (for IDL-antibody complexes), EMD-9092 to 9094 (for IDL-antibody-IDL complexes), and EMD-9095 to 9099 (for antibodies). Details of these density maps and their corresponding EMDB entry numbers are listed in Supplementary Table 1.

References

[1] J.C. Frias, M.J. Lipinski, S.E. Lipinski, M.T. Albelda, Modified lipoproteins as contrast agents for imaging of atherosclerosis, Contrast Media Mol. Imaging 2 (2007) 16–23.
[2] R.E. Olson, Discovery of the lipoproteins, their role in fat transport and their significance as risk factors, J. Nutr. 128 (1998) 439s–443s.
[3] B. Shen, A. Scanu, F. Kezdy, Structure of human serum lipoproteins inferred from compositional analysis, Proc. Natl. Acad. Sci. U. S. A. 74 (1977) 837.

[4] P. Nilsson-Ehle, A.S. Garfinkel, M.C. Schotz, Lipolytic enzymes and plasma lipoprotein metabolism, Annu. Rev. Biochem. 49 (1980) 667–693.
[5] J.E. Vance, Assembly and secretion of lipoproteins, New Compr. Biochem. 36 (2002) 505–526.
[6] J. Baynes, M.H. Dominiczak, Medical Biochemistry, Elsevier Health Sciences, 2009.
[7] N. Rifai, G.R. Warnick, M.H. Dominiczak, Handbook of Lipoprotein Testing, Amer. Assoc. for Clinical Chemistry, 2000.
[8] M.H. Dominiczak, M.J. Caslake, Apolipoproteins: metabolic role and clinical biochemistry applications, Ann. Clin. Biochem. 48 (2011) 498–515.
[9] P.-O. Attman, P. Alaupovic, M. Tavella, C. Knight-Gibson, Abnormal lipid and apolipoprotein composition of major lipoprotein density classes in patients with chronic renal failure, Nephrol. Dial. Transplant. 11 (1996) 63–69.
[10] R.W. Mahley, Atherogenic lipoproteins and coronary artery disease: concepts derived from recent advances in cellular and molecular biology, Circulation 72 (1985) 943–948.
[11] M.F. Reardon, P.J. Nestel, I.H. Craig, R.W. Harper, Lipoprotein predictors of the severity of coronary artery disease in men and women, Circulation 71 (1985) 881–888.
[12] P.A. Mayes, K.M. Botham, Cholesterol synthesis, transport, and excretion, Harper's illustrated, Biochemistry (2003) 219–227.
[13] E.J. Schaefer, S. Eisenberg, R.I. Levy, Lipoprotein apoprotein metabolism, J. Lipid Res. 19 (1978) 667–687.
[14] H. Okamoto, A. Miyai, T. Sasase, N. Furukawa, M. Matsushita, T. Nakano, K. Nakajima, Cholesteryl ester transfer protein promotes the formation of cholesterol-rich remnant like lipoprotein particles in human plasma, Clin. Chim. Acta 375 (2007) 92–98.
[15] L. Zhang, F. Yan, S. Zhang, D. Lei, M.A. Charles, G. Cavigiolio, M. Oda, R.M. Krauss, K.H. Weisgraber, K.A. Rye, H.J. Pownall, X. Qiu, G. Ren, Structural basis of transfer between lipoproteins by cholesteryl ester transfer protein, Nat. Chem. Biol. 8 (2012) 342–349.
[16] M. Zhang, R. Charles, H. Tong, L. Zhang, M. Patel, F. Wang, M.J. Rames, A. Ren, K.A. Rye, X. Qiu, D.G. Johns, M.A. Charles, G. Ren, HDL surface lipids mediate CETP binding as revealed by electron microscopy and molecular dynamics simulation, Sci. Rep.-UK 5 (2015) 8741.
[17] T.A. Musliner, C. Giotas, R.M. Krauss, Presence of multiple subpopulations of lipoproteins of intermediate density in normal subjects, Arteriosclerosis 6 (1986) 79–87.
[18] D.S. Kelley, D. Siegel, M. Vemuri, B.E. Mackey, Docosahexaenoic acid supplementation improves fasting and postprandial lipid profiles in hypertriglyceridemic men, Am. J. Clin. Nutr. 86 (2007) 324–333.
[19] X.C. Bai, G. McMullan, S.H. Scheres, How cryo-EM is revolutionizing structural biology, Trends Biochem. Sci. 40 (2015) 49–57.
[20] L. Zhang, G. Ren, IPET and FETR: experimental approach for studying molecular structure dynamics by cryo-electron tomography of a single-molecule structure, PLoS One 7 (2012) e30249.
[21] J.R. Patsch, S. Sailer, H. Braunsteiner, T. Forte, Electron microscopic characterization of lipoproteins from patients with familial type III hyperlipoproteinaemia, Eur. J. Clin. Investig. 6 (1976) 307–310.
[22] Y.D. Yu, Y.L. Kuang, D.S. Lei, X.B. Zhai, M. Zhang, R.M. Krauss, G. Ren, Polyhedral 3D structure of human plasma very low density lipoproteins by individual particle cryo-electron tomography, J. Lipid Res. 57 (2016) 1879–1888.
[23] D. Cheng, D.R.G. Mitchell, D.-B. Shieh, F. Braet, Practical considerations in the successful preparation of specimens for thin-film cryo-transmission electron microscopy, in: A. Mendez-Vilas (Ed.), Current Microscopy Contributions to Advances in Science and Technology, FORMATEX, Badajoz, Spain, 2012, pp. 880–890.
[24] A. Robards, V. Sleytr, Low temperature methods in biological electron microscopy, Practical Methods in Electron Microscopy, Elsevier Press, Amsterdam, 1985.
[25] M. Caffrey, D. Bilderback, Kinetics of the main phase transition of hydrated lecithin monitored by real-time X-ray diffraction, Biophys. J. 45 (1984) 627–631.
[26] D. Vaknin, K. Kjaer, J. Als-Nielsen, M. Lösche, Structural properties of phosphatidylcholine in a monolayer at the air/water interface, Biophys. J. 59 (1991) 1325–1332.
[27] E.O. Saphire, P.W. Parren, R. Pantophlet, M.B. Zwick, G.M. Morris, P.M. Rudd, R.A. Dwek, R.L. Stanfield, D.R. Burton, I.A. Wilson, Crystal structure of a neutralizing human IGG against HIV-1: a template for vaccine design, Science 293 (2001) 1155–1159.
[28] X. Zhang, J. Sheng, P. Plevka, R.J. Kuhn, M.S. Diamond, M.G. Rossmann, Dengue structure differs at the temperatures of its human and mosquito hosts, Proc. Natl. Acad. Sci. U. S. A. 110 (2013) 6795–6799.
[29] G. Fibriansah, T.S. Ng, V.A. Kostyuchenko, J. Lee, S. Lee, J. Wang, S.M. Lok, Structural changes in dengue virus when exposed to a temperature of 37 degrees C, J. Virol. 87 (2013) 7585–7592.
[30] R. Prassl, M. Pregetter, H. Amenitsch, M. Kriechbaum, R. Schwarzenbacher, J.M. Chapman, P. Laggner, Low density lipoproteins as circulating fast temperature sensors, PLoS One 3 (2008) e4079.
[31] R.J. Deckelbaum, G.G. Shipley, D.M. Small, Structure and interactions of lipids in human plasma low density lipoproteins, J. Biol. Chem. 252 (1977) 744–754.
[32] L. Bagatolli, E. Gratton, Two-photon fluorescence microscopy observation of shape changes at the phase transition in phospholipid giant unilamellar vesicles, Biophys. J. 77 (1999) 2090–2101.
[33] K. Dierksen, D. Typke, R. Hegerl, J. Walz, E. Sackmann, W. Baumeister, Three-dimensional structure of lipid vesicles embedded in vitreous ice and investigated by automated electron tomography, Biophys. J. 68 (1995) 1416–1422.
[34] J. Seddon, R. Templer, Polymorphism of lipid-water systems, Handbook of Biological Physics, vol. 1, 1995, pp. 97–160.
[35] D.P. Siegel, W.J. Green, Y. Talmon, The mechanism of lamellar-to-inverted hexagonal phase transitions: a study using temperature-jump cryo-electron microscopy, Biophys. J. 66 (1994) 402–414.
[36] S. Asano, Y. Fukuda, F. Beck, A. Aufderheide, F. Forster, R. Danev, W. Baumeister, Proteasomes. A molecular census of 26S proteasomes in intact neurons, Science 347 (2015) 439–442.
[37] A. von Appen, J. Kosinski, L. Sparks, A. Ori, A.L. DiGuilio, B. Vollmer, M.T. Mackmull, N. Banterle, L. Parca, P. Kastritis, K. Buczak, S. Mosalaganti, W. Hagen, A. Andres-Pons, E.A. Lemke, P. Bork, W. Antonin, J.S. Glavy, K.H. Bui, M. Beck, In situ structural analysis of the human nuclear pore complex, Nature 526 (2015) 140–143.
[38] J.R. Kremer, D.N. Mastronarde, J.R. McIntosh, Computer visualization of three-dimensional image data using IMOD, J. Struct. Biol. 116 (1996) 71–76.
[39] L. Zhang, H. Tong, M. Garewal, G. Ren, Optimized negative-staining electron microscopy for lipoprotein studies, Biochim. Biophys. Acta 1830 (2013) 2150–2159.
[40] X. Zhang, L. Zhang, H. Tong, B. Peng, M.J. Rames, S. Zhang, G. Ren, 3D structural fluctuation of IgG1 antibody revealed by individual particle electron tomography, Sci. Rep.-UK 5 (2015) 9803.
[41] L. Zhang, D. Lei, J.M. Smith, M. Zhang, H. Tong, X. Zhang, Z. Lu, J. Liu, A.P. Alivisatos, G. Ren, Three-dimensional structural dynamics and fluctuations of DNA-nanogold conjugates by individual-particle electron tomography, Nat. Commun. 7 (2016) 11083.
[42] D. Lei, A.E. Marras, J. Liu, C. Huang, L. Zhou, C.E. Castro, H. Su, G. Ren, 3D structural dynamics of DNA Origami Bennett linkages using individual-particle electron tomography, Nat. Commun. 9 (2018) 592.
[43] Z. Lu, M.V. Reddy, J. Liu, A. Kalichava, J. Liu, L. Zhang, F. Chen, Y. Wang, L.M. Holthauzen, M.A. White, S. Seshadrinathan, X. Zhong, G. Ren, G. Rudenko, Molecular architecture of contactin-associated protein-like 2 (CNTNAP2) and its interaction with contactin 2 (CNTN2), J. Biol. Chem. 291 (2016) 24133–24147.
[44] Z. Lu, Y. Wang, F. Chen, H. Tong, M.V. Reddy, L. Luo, S. Seshadrinathan, L. Zhang, L.M. Holthauzen, A.M. Craig, G. Ren, G. Rudenko, Calsyntenin-3 molecular architecture and interaction with neurexin 1alpha, J. Biol. Chem. 289 (2014) 34530–34542.
[45] J.J. Fernandez, S. Li, R.A. Crowther, CTF determination and correction in electron cryotomography, Ultramicroscopy 106 (2006) 587–596.
[46] G. Zanetti, J.D. Riches, S.D. Fuller, J.A. Briggs, Contrast transfer function correction applied to cryo-electron tomography and sub-tomogram averaging, J. Struct. Biol. 168 (2009) 305–312.
[47] Q. Xiong, M.K. Morphew, C.L. Schwartz, A.H. Hoenger, D.N. Mastronarde, CTF determination and correction for low dose tomographic tilt series, J. Struct. Biol. 168 (2009) 378–387.
[48] P.A. Penczek, Image restoration in cryo-electron microscopy, Methods Enzymol. 482 (2010) 35–72.
[49] M.A. Charles, J.P. Kane, New molecular insights into CETP structure and function: a review, J. Lipid Res. 53 (2012) 1451–1458.
[50] A. Kontush, M. Lindahl, M. Lhomme, L. Calabresi, M.J. Chapman, W.S. Davidson, Structure of HDL: particle subclasses and molecular components, High Density Lipoproteins, Springer, 2015, pp. 3–51.
[51] F.H. Rached, M.J. Chapman, A. Kontush, HDL particle subpopulations: focus on biological function, Biofactors 41 (2015) 67–77.
[52] R.A. Silva, R. Huang, J. Morris, J. Fang, E.O. Gracheva, G. Ren, A. Kontush, W.G. Jerome, K.A. Rye, W.S. Davidson, Structure of apolipoprotein A-I in spherical high density lipoproteins of different sizes, Proc. Natl. Acad. Sci. U. S. A. 105 (2008) 12176–12181.
[53] M.C. Phillips, New insights into the determination of HDL structure by apolipoproteins: thematic review series: high density lipoprotein structure, function, and metabolism, J. Lipid Res. 54 (2013) 2034–2048.
[54] A.Y. Shih, S.G. Sligar, K. Schulten, Maturation of high-density lipoproteins, J. R. Soc. Interface 6 (2009) 863–871.
[55] R. Huang, R.A. Silva, W.G. Jerome, A. Kontush, M.J. Chapman, L.K. Curtiss, T.J. Hodges, W.S. Davidson, Apolipoprotein A-I structural organization in high-density lipoproteins isolated from human plasma, Nat. Struct. Mol. Biol. 18 (2011) 416–422.
[56] M. Zhang, X. Zhai, J. Li, J.J. Albers, S. Vuletic, G. Ren, Structural basis of the lipid transfer mechanism of phospholipid transfer protein (PLTP), Biochim. Biophys. Acta Mol. Cell Biol. Lipids 1863 (2018) 1082–1094.
[57] G. Cilpa-Karhu, M. Jauhiainen, M.L. Riekkola, Atomistic MD simulation reveals the mechanism by which CETP penetrates into HDL enabling lipid transfer from HDL to CETP, J. Lipid Res. 56 (2015) 98–108.
[58] G. Ren, G. Rudenko, S.J. Ludtke, J. Deisenhofer, W. Chiu, H.J. Pownall, Model of human low-density lipoprotein and bound receptor based on cryoEM, Proc. Natl. Acad. Sci. U. S. A. 107 (2010) 1059–1064.
[59] S.J. Ludtke, P.R. Baldwin, W. Chiu, EMAN: semiautomated software for high-resolution single-particle reconstructions, J. Struct. Biol. 128 (1999) 82–97.
[60] E.F. Pettersen, T.D. Goddard, C.C. Huang, G.S. Couch, D.M. Greenblatt, E.C. Meng, T.E. Ferrin, UCSF chimera–a visualization system for exploratory research and analysis, J. Comput. Chem. 25 (2004) 1605–1612.

Supplementary Information

for

Single-molecule 3D imaging of human plasma intermediate-density lipoproteins reveals a polyhedral structure

Dongsheng Lei, Yadong Yu, Yu-Lin Kuang, Jianfang Liu, Ronald M. Krauss, Gang Ren

Supplementary Figures

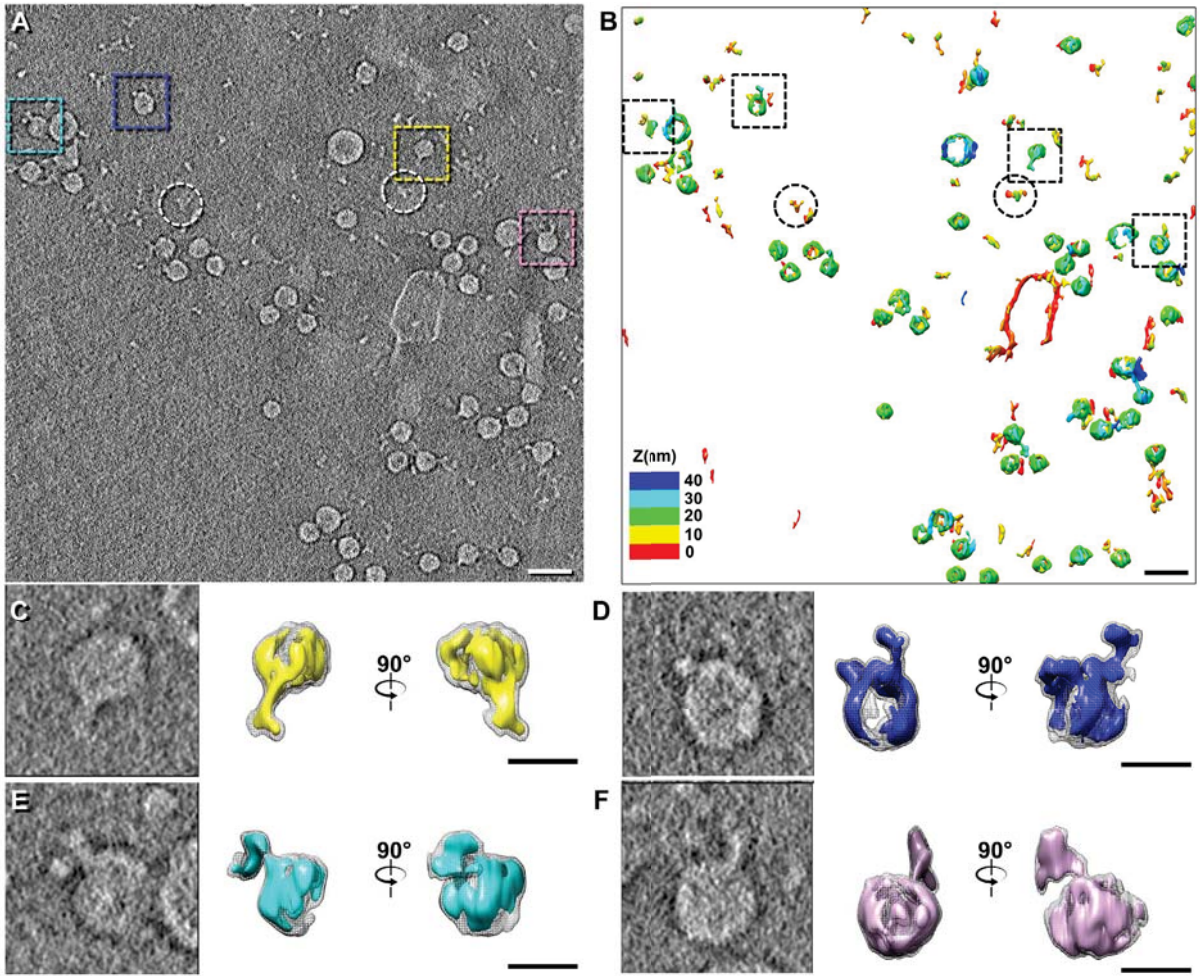

Supplementary Figure S1 | Validation of the 3D reconstruction using the third-party software IMOD (**A**) 2D projection of the whole tomogram of an IDL-antibody complex reconstructed using IMOD (low-pass filtered at 2 nm). (**B**) The whole tomogram is displayed in iso-surface rendering and colored from red to blue based on Z height (low-pass filtered at 10 nm). The tomogram contains ~40 polyhedral-shaped particles, ~75% of which are bound to antibodies (indicated by the presence of a Y- or rod-shaped protrusion). The observation of antibodies (anti-apoB-100, mAB012) and their bounding to these polyhedral-shaped particles confirms that the polyhedral-shaped particles contain apoB-100 and should therefore be IDL. Representative IDL-antibody complexes and antibodies alone are indicated by squares and circles, respectively. (**C-F)** 2D projections and 3D views of four representative IDL-antibody complexes. The 3D views of these complexes are displayed at two different contour levels (high contour level in surface and low contour level in mesh). The high contour surfaces are colored based on their positions in A. Scale bar: 50 nm in A and B; 20 nm in C through F.

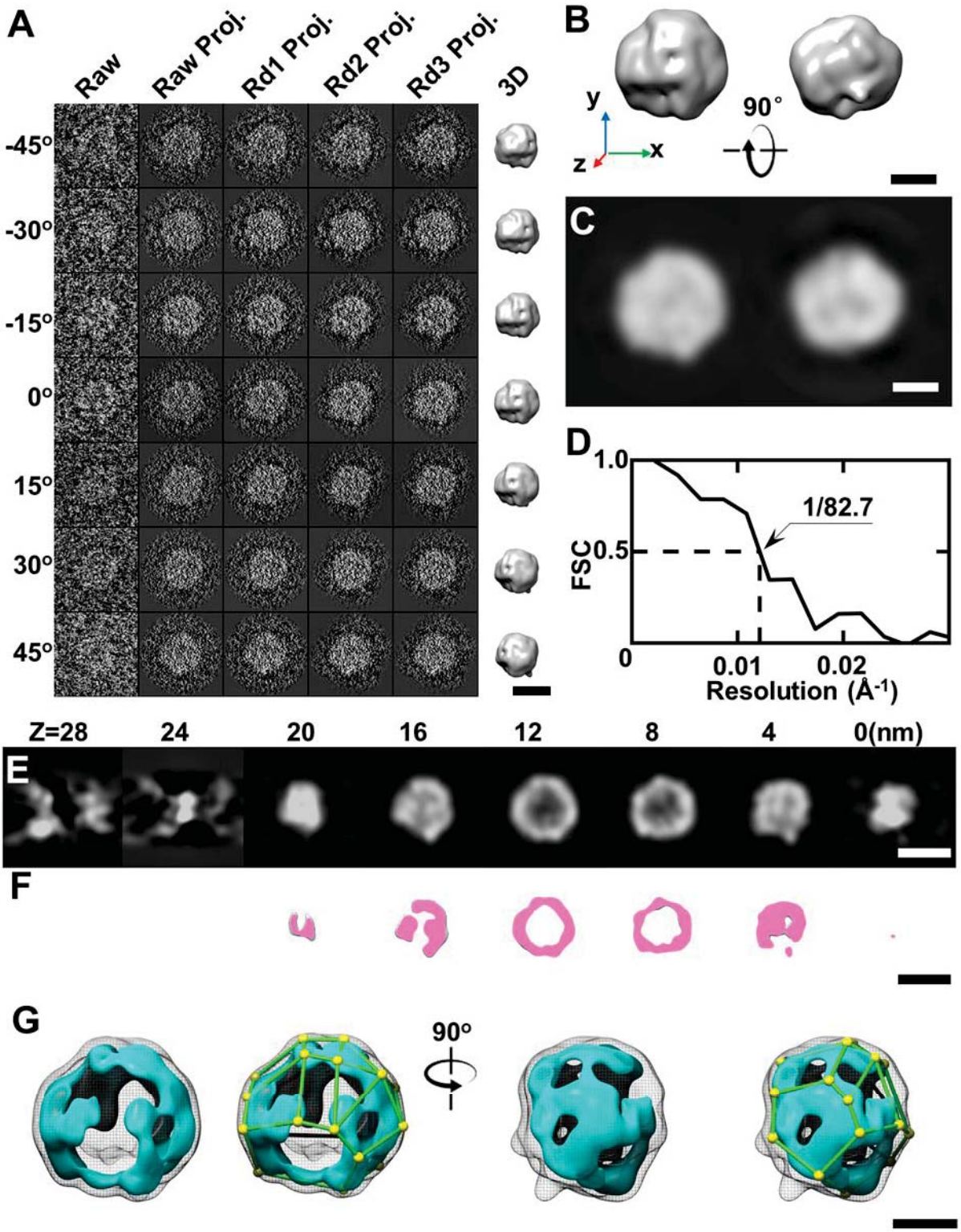

Supplementary Figure S2 | 3D reconstruction of the third IDL by IPET (**A**) Seven representative tilt images (image contrast reversed) of the third targeted individual IDL particle are displayed in the first column on the left. The tilt images were gradually aligned to a common center via an iterative refinement process to achieve a 3D reconstruction by using IPET. The projections of the raw,

intermediate and final 3D reconstructions are shown based on their corresponding tilt angles. (**B**) Two orthogonal views of the final 3D reconstruction (low-pass filtered at 8 nm). (**C**) 2D projections of final 3D reconstruction in the same view directions as in subfigure B. (**D**) The resolution of the IPET reconstruction was ~8.3 nm by FSC analyses (based on two density maps reconstructed from odd- and even-numbered tilt images). (**E**) Projection of the 3D map at different Z heights. (**F**) Iso-surface of the 3D map at different Z heights. (**G**) The final map displayed at two different contour levels (high contour level in cyan and low contour level in gray). Scale bars: 20 nm in A, E and F; 10 nm in B, C and G.

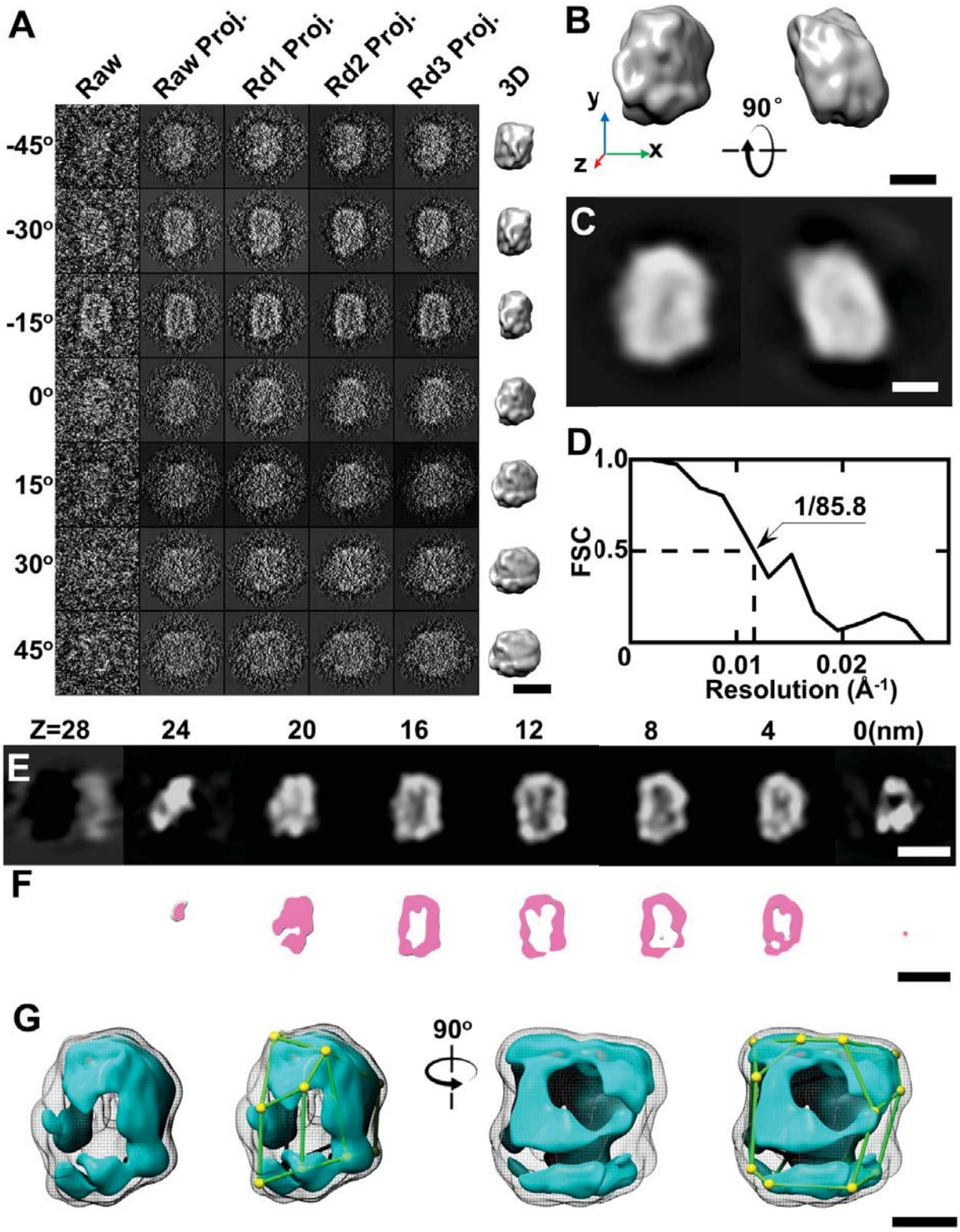

Supplementary Figure S3 | 3D reconstruction of the fourth IDL by IPET (**A**) Seven representative tilt images (image contrast reversed) of the fourth targeted individual IDL particle are displayed in the first column on the left. The tilt images were gradually aligned to a common center via an iterative refinement process to achieve a 3D reconstruction by using IPET. The projections of the raw,

intermediate and final 3D reconstructions are shown based on their corresponding tilt angles. (**B**) Two orthogonal views of the final 3D reconstruction (low-pass filtered at 8 nm). (**C**) 2D projections of final 3D reconstruction in the same view directions as in subfigure B. (**D**) The resolution of the IPET reconstruction was ~8.6 nm by FSC analyses (based on two density maps reconstructed from odd- and even-numbered tilt images). (**E**) Projection of the 3D map at different Z heights. (**F**) Iso-surface of the 3D map at different Z heights. (**G**) The final map displayed at two different contour levels (high contour level in cyan and low contour level in gray). Scale bars: 20 nm in A, E and F; 10 nm in B, C and G.

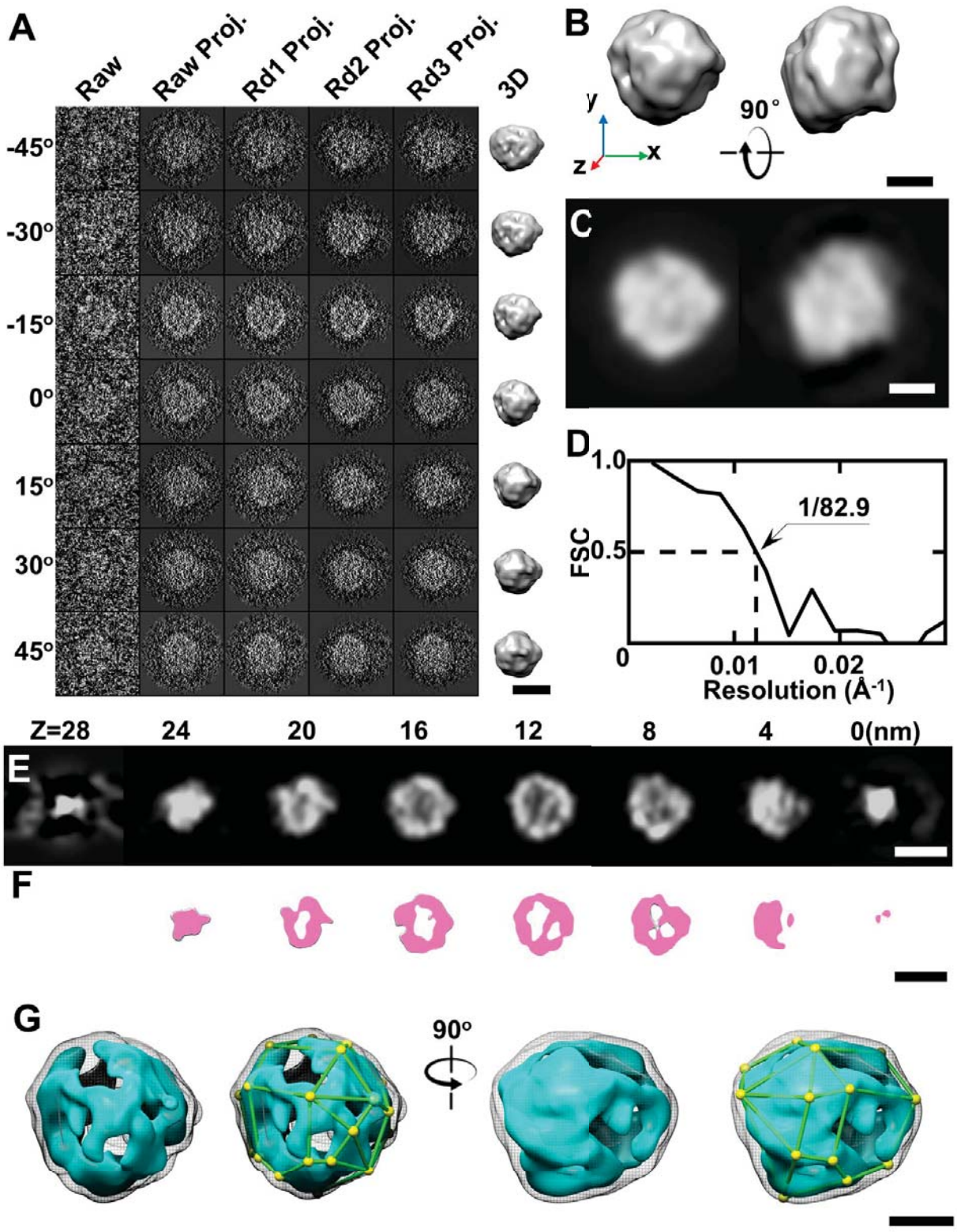

Supplementary Figure S4 | 3D reconstruction of the fifth IDL by IPET (**A**) Seven representative tilt images (image contrast reversed) of the fifth targeted individual IDL particle are displayed in the first column on the left. The tilt images were gradually aligned to a common center via an iterative refinement process to achieve a 3D reconstruction by using IPET. The projections of the raw,

intermediate and final 3D reconstructions are shown based on their corresponding tilt angles. (**B**) Two orthogonal views of the final 3D reconstruction (low-pass filtered at 8 nm). (**C**) 2D projections of the final 3D reconstruction in the same view directions as in subfigure B. (**D**) The resolution of the IPET reconstruction was ~8.3 nm by FSC analyses (based on two density maps reconstructed from odd- and even-numbered tilt images). (**E**) Projection of the 3D map at different Z heights. (**F**) Iso-surface of the 3D map at different Z heights. (**G**) The final map displayed at two different contour levels (high contour level in cyan and low contour level in gray). Scale bars: 20 nm in A, E and F; 10 nm in B, C and G.

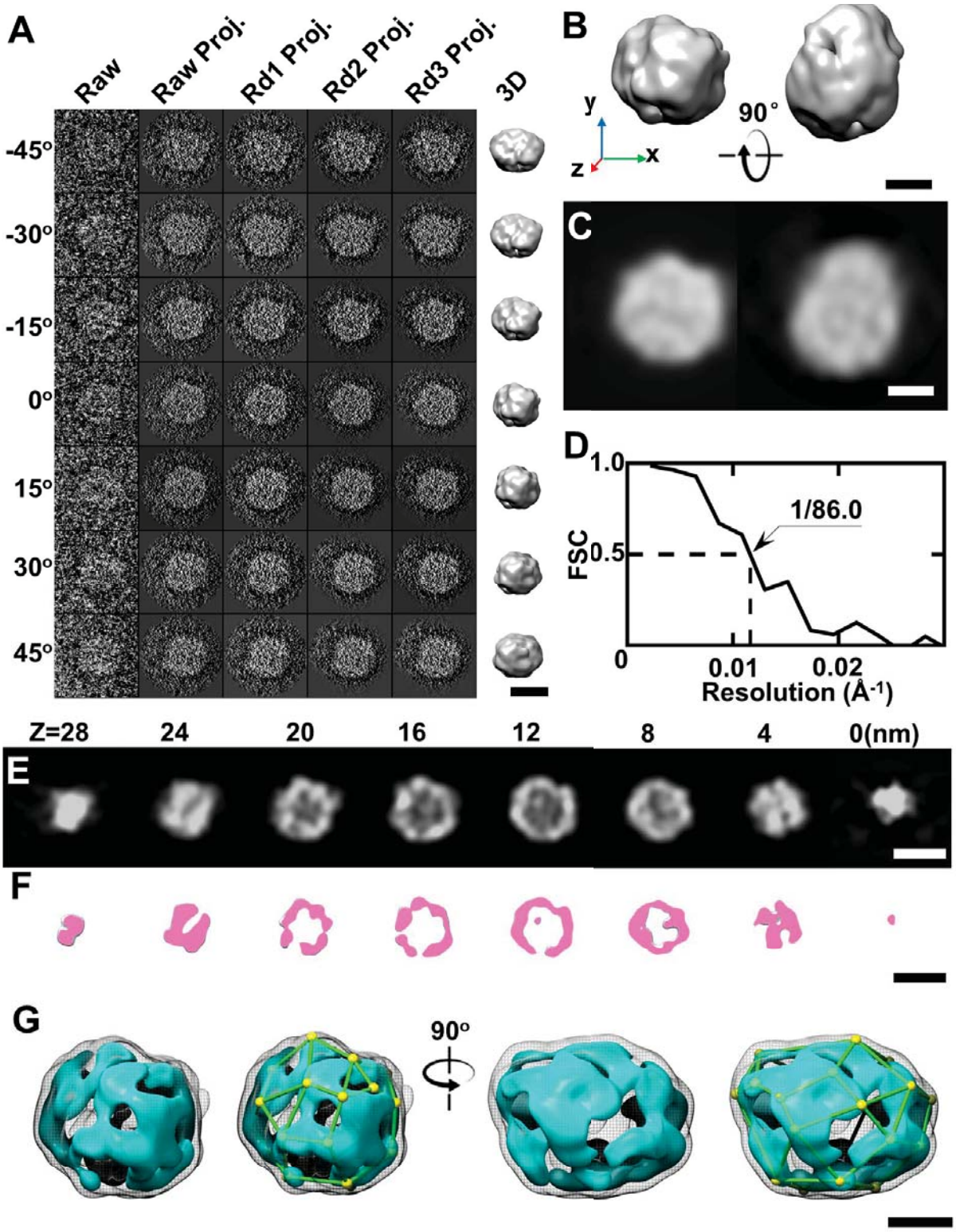

Supplementary Figure S5 | 3D reconstruction of the sixth IDL by IPET (**A**) Seven representative tilt images (image contrast reversed) of the sixth targeted individual IDL particle are displayed in the first column on the left. The tilt images were gradually aligned to a common center via an iterative refinement process to achieve a 3D reconstruction by using IPET. The projections of the raw, intermediate and final 3D reconstructions are shown based on their corresponding tilt angles. (**B**) Two

orthogonal views of the final 3D reconstruction (low-pass filtered at 8 nm). (**C**) 2D projections of the final 3D reconstruction in the same view directions as in subfigure B. (**D**) The resolution of the IPET reconstruction was ~8.6 nm by FSC analyses (based on two density maps reconstructed from odd- and even-numbered tilt images). (**E**) Projection of the 3D map at different Z heights. (**F**) Iso-surface of the 3D map at different Z heights. (**G**) The final map displayed at two different contour levels (high contour level in cyan and low contour level in gray). Scale bars: 20 nm in A, E and F; 10 nm in B, C and G.

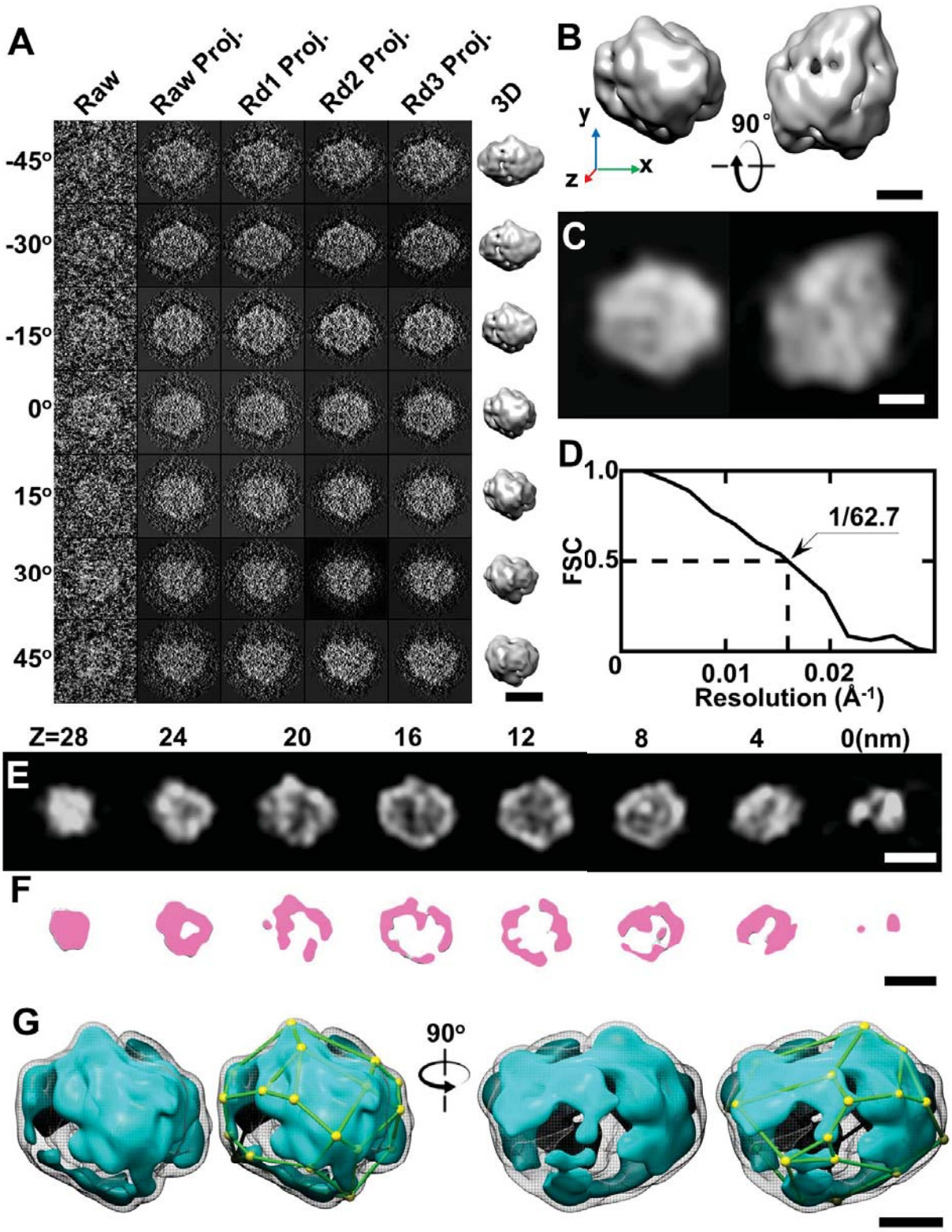

Supplementary Figure S6 | 3D reconstruction of the seventh IDL by IPET (**A**) Seven representative tilt images (image contrast reversed) of the seventh targeted individual IDL particle are displayed in the first column on the left. The tilt images were gradually aligned to a common center via an iterative refinement process to achieve a 3D reconstruction by using IPET. The projections of the raw,

intermediate and final 3D reconstructions are shown based on their corresponding tilt angles. (**B**) Two orthogonal views of the final 3D reconstruction (low-pass filtered at 8 nm). (**C**) 2D projections of the final 3D reconstruction in the same view directions as in subfigure B. (**D**) The resolution of the IPET reconstruction was ~6.3 nm by FSC analyses (based on two density maps reconstructed from odd- and even-numbered tilt images). (**E**) Projection of the 3D map at different Z heights. (**F**) Iso-surface of the 3D map at different Z heights. (**G**) The final map displayed at two different contour levels (high contour level in cyan and low contour level in gray). Scale bars: 20 nm in A, E and F; 10 nm in B, C and G.

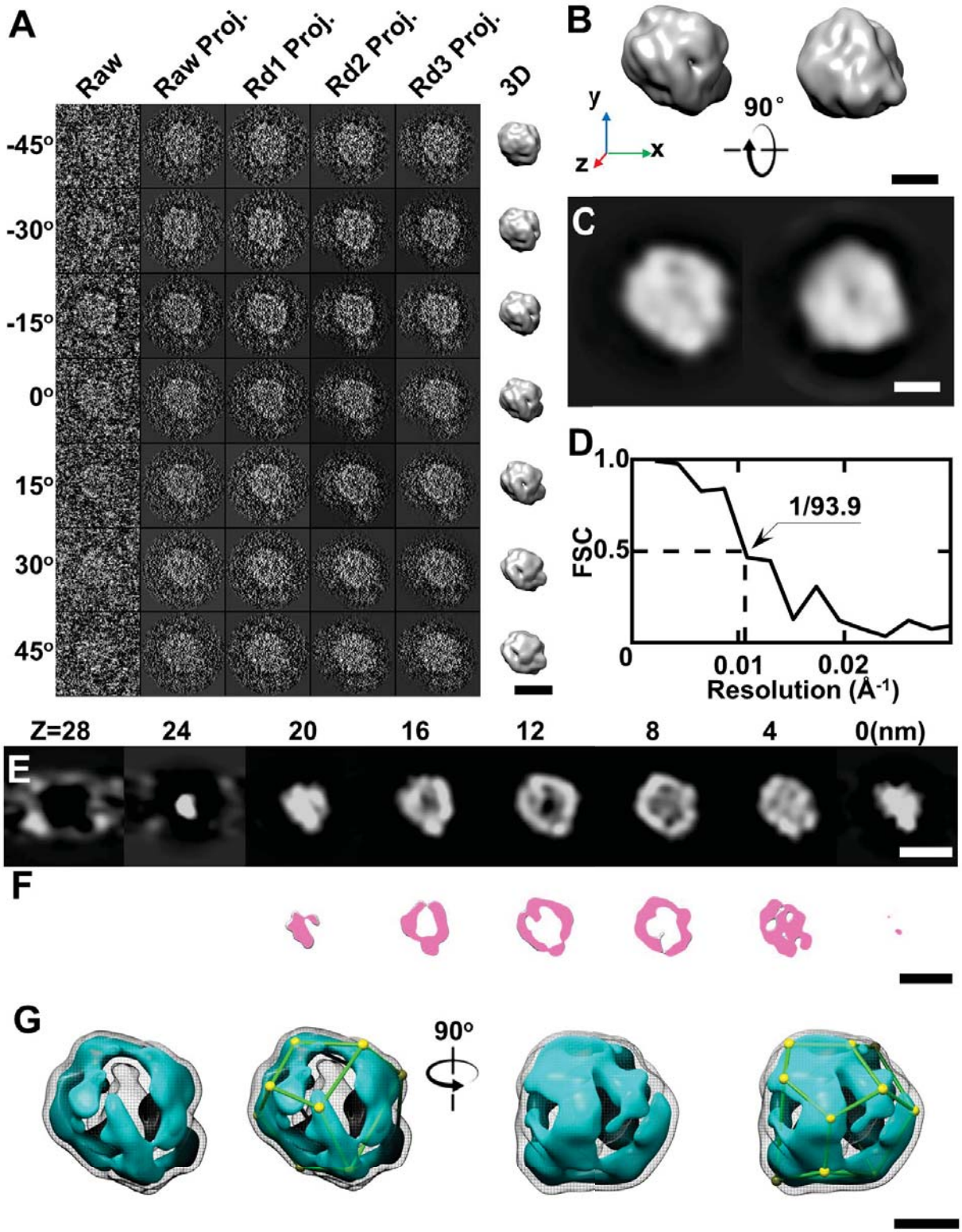

Supplementary Figure S7 | 3D reconstruction of the eighth IDL by IPET (**A**) Seven representative tilt images (image contrast reversed) of the eighth targeted individual IDL particle are displayed in the first column on the left. The tilt images were gradually aligned to a common center via an iterative refinement process to achieve a 3D reconstruction by using IPET. The projections of the raw,

intermediate and final 3D reconstructions are shown based on their corresponding tilt angles. (**B**) Two orthogonal views of the final 3D reconstruction (low-pass filtered at 8 nm). (**C**) 2D projections of the final 3D reconstruction in the same view directions as in subfigure B. (**D**) The resolution of the IPET reconstruction was ~9.4 nm by FSC analyses (based on two density maps reconstructed from odd- and even-numbered tilt images). (**E**) Projection of the 3D map at different Z heights. (**F**) Iso-surface of the 3D map at different Z heights. (**G**) The final map displayed at two different contour levels (high contour level in cyan and low contour level in gray). Scale bars: 20 nm in A, E and F; 10 nm in B, C and G.

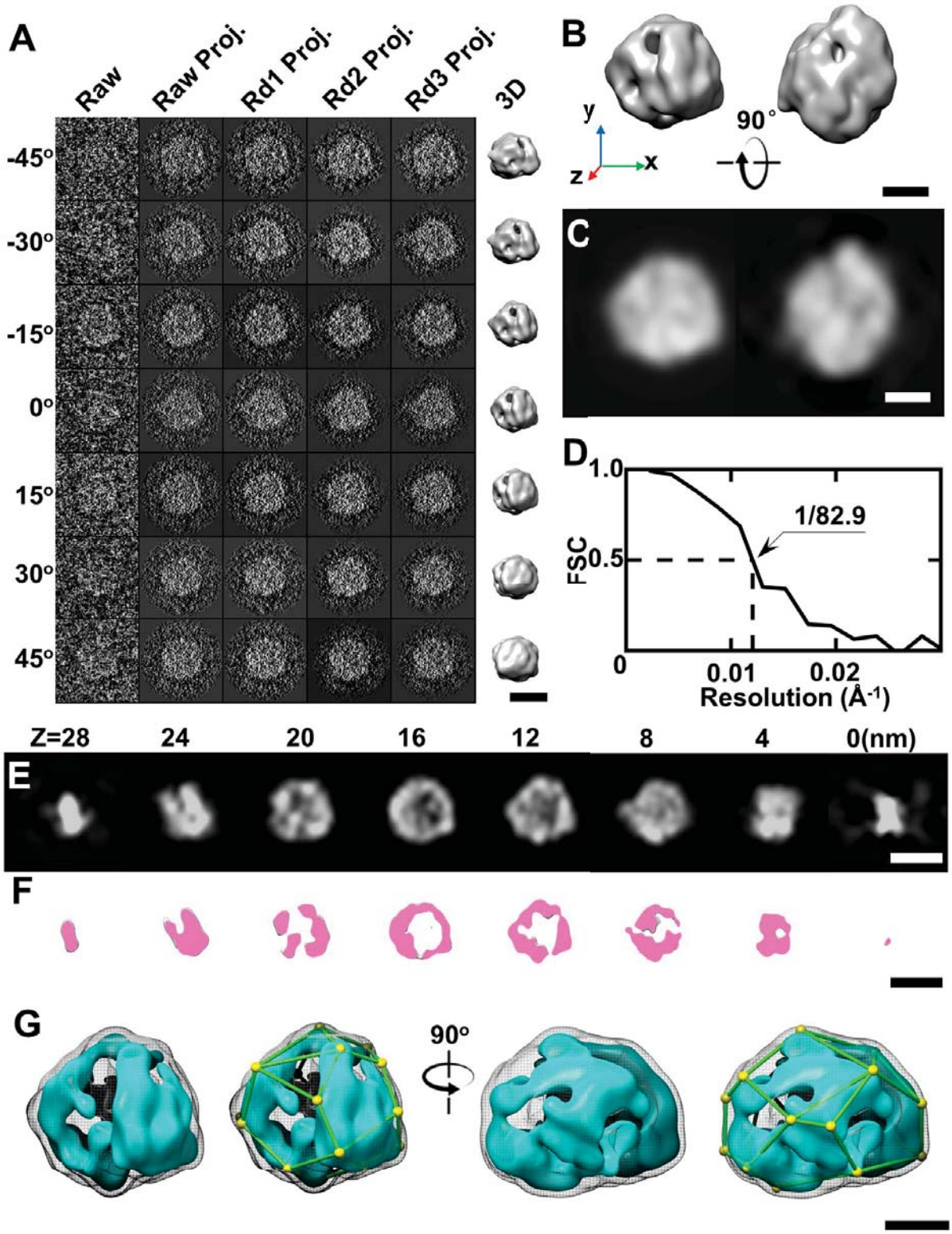

Supplementary Figure S8 | 3D reconstruction of the ninth IDL by IPET (**A**) Seven representative tilt images (image contrast reversed) of the ninth targeted individual IDL particle are displayed in the first column on the left. The tilt images were gradually aligned to a common center via an iterative refinement process to achieve a 3D reconstruction by using IPET. The projections of the raw,

intermediate and final 3D reconstructions are shown based on their corresponding tilt angles. (**B**) Two orthogonal views of the final 3D reconstruction (low-pass filtered at 8 nm). (**C**) 2D projections of the final 3D reconstruction in the same view directions as in subfigure B. (**D**) The resolution of the IPET reconstruction was ~8.3 nm by FSC analyses (based on two density maps reconstructed from odd- and even-numbered tilt images). (**E**) Projection of the 3D map at different Z heights. (**F**) Iso-surface of the 3D map at different Z heights. (**G**) The final map displayed at two different contour levels (high contour level in cyan and low contour level in gray). Scale bars: 20 nm in A, E and F; 10 nm in B, C and G.

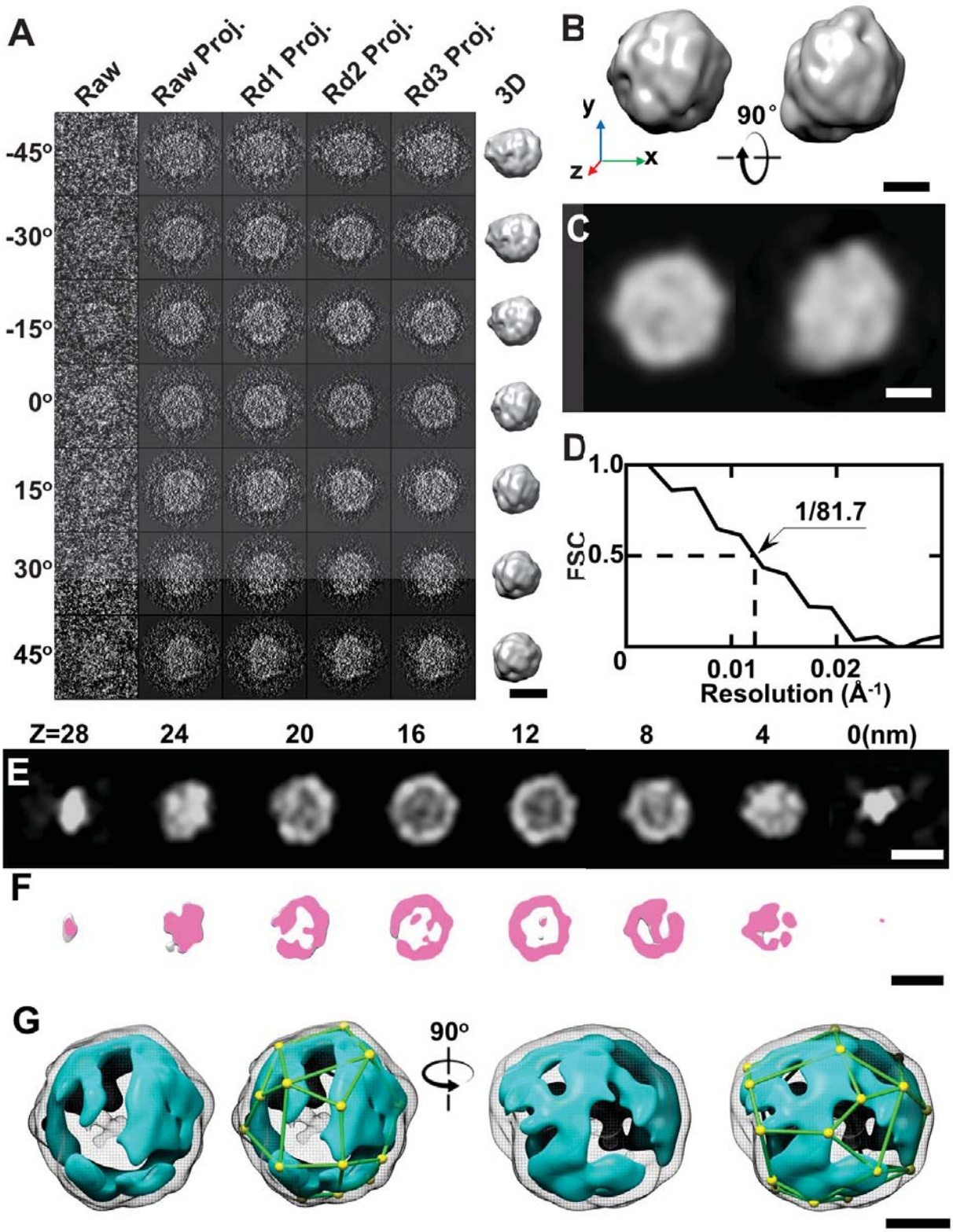

Supplementary Figure S9 | 3D reconstruction of the tenth IDL by IPET (**A**) Seven representative tilt images (image contrast reversed) of the tenth targeted individual IDL particle are displayed in the first column on the left. The tilt images were gradually aligned to a common center via an iterative

refinement process to achieve a 3D reconstruction by using IPET. The projections of the raw, intermediate and final 3D reconstructions are shown based on their corresponding tilt angles. (**B**) Two orthogonal views of the final 3D reconstruction (low-pass filtered at 8 nm). (**C**) 2D projections of the final 3D reconstruction in the same view directions as in subfigure B. (**D**) The resolution of the IPET reconstruction was ~8.2 nm by FSC analyses (based on two density maps reconstructed from odd- and even-numbered tilt images). (**E**) Projection of the 3D map at different Z heights. (**F**) Iso-surface of the 3D map at different Z heights. (**G**) The final map displayed at two different contour levels (high contour level in cyan and low contour level in gray). Scale bars: 20 nm in A, E and F; 10 nm in B, C and G.

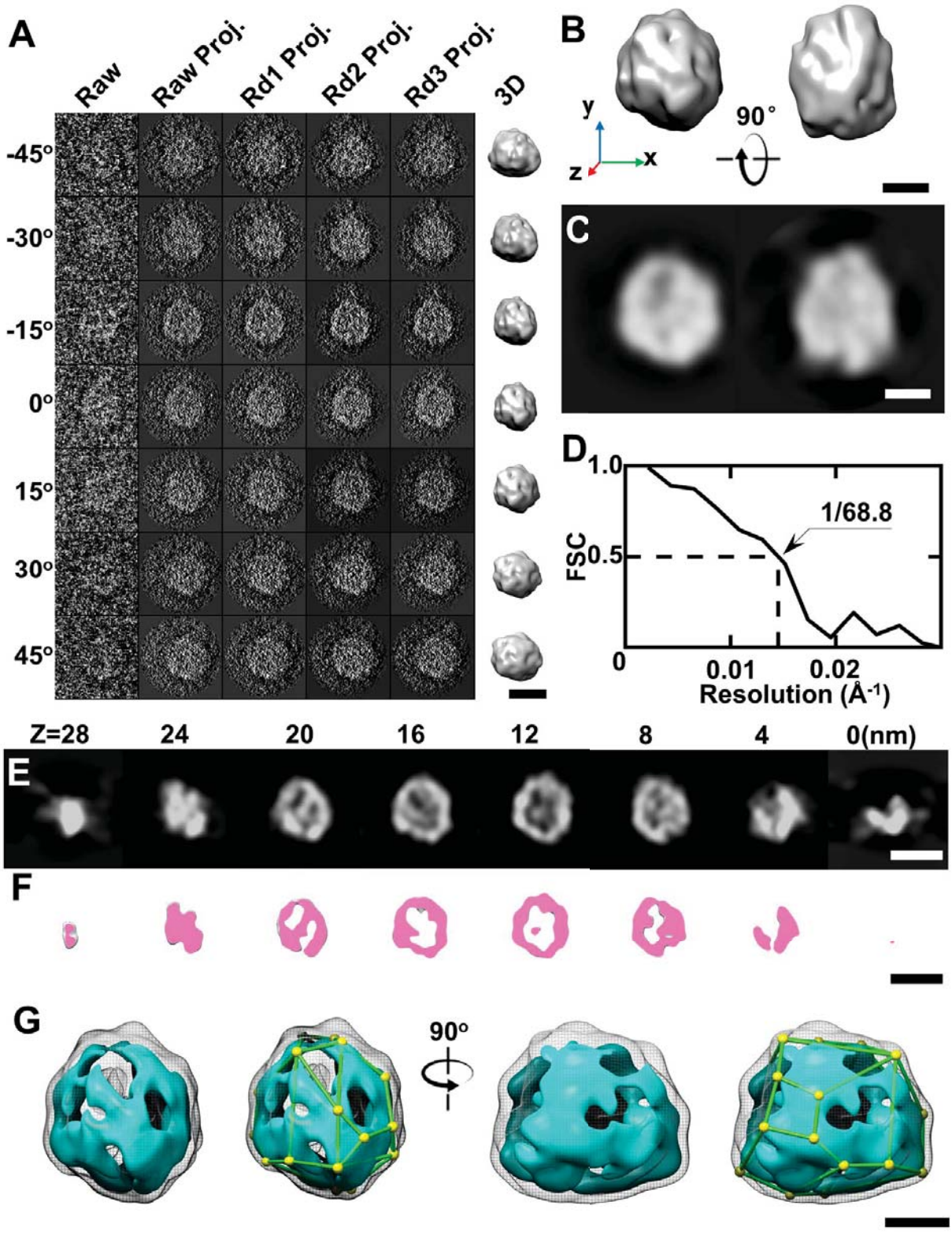

Supplementary Figure S10 | 3D reconstruction of the 11th IDL by IPET (**A**) Seven representative tilt images (image contrast reversed) of the 11th targeted individual IDL particle are displayed in the first column on the left. The tilt images were gradually aligned to a common center via an iterative

refinement process to achieve a 3D reconstruction by using IPET. The projections of the raw, intermediate and final 3D reconstructions are shown based on their corresponding tilt angles. (**B**) Two orthogonal views of the final 3D reconstruction (low-pass filtered at 8 nm). (**C**) 2D projections of the final 3D reconstruction in the same view directions as in subfigure B. (**D**) The resolution of the IPET reconstruction was ~6.9 nm by FSC analyses (based on two density maps reconstructed from odd- and even-numbered tilt images). (**E**) Projection of the 3D map at different Z heights. (**F**) Iso-surface of the 3D map at different Z heights. (**G**) The final map displayed at two different contour levels (high contour level in cyan and low contour level in gray). Scale bars: 20 nm in A, E and F; 10 nm in B, C and G.

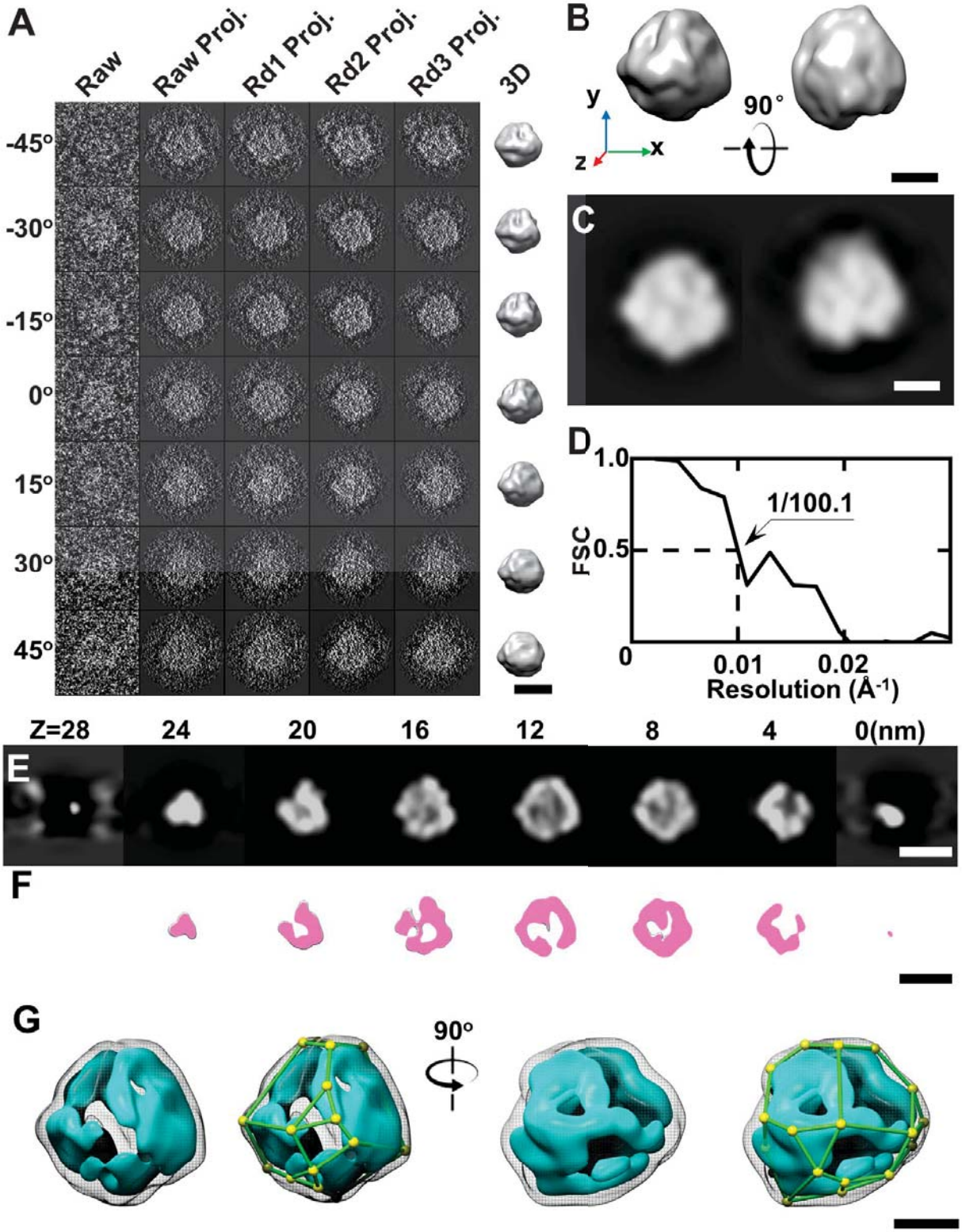

Supplementary Figure S11 | 3D reconstruction of the 12th IDL by IPET (**A**) Seven representative tilt images (image contrast reversed) of the 12th targeted individual IDL particle are displayed in the 12th column on the left. The tilt images were gradually aligned to a common center via an iterative

refinement process to achieve a 3D reconstruction by using IPET. The projections of the raw, intermediate and final 3D reconstructions are shown based on their corresponding tilt angles. (**B**) Two orthogonal views of the final 3D reconstruction (low-pass filtered at 8 nm). (**C**) 2D projections of the final 3D reconstruction in the same view directions as in subfigure B. (**D**) The resolution of the IPET reconstruction was ~10.0 nm by FSC analyses (based on two density maps reconstructed from odd- and even-numbered tilt images). (**E**) Projection of the 3D map at different Z heights. (**F**) Iso-surface of the 3D map at different Z heights. (**G**) The final map displayed at two different contour levels (high contour level in cyan and low contour level in gray). Scale bars: 20 nm in A, E and F; 10 nm in B, C and G.

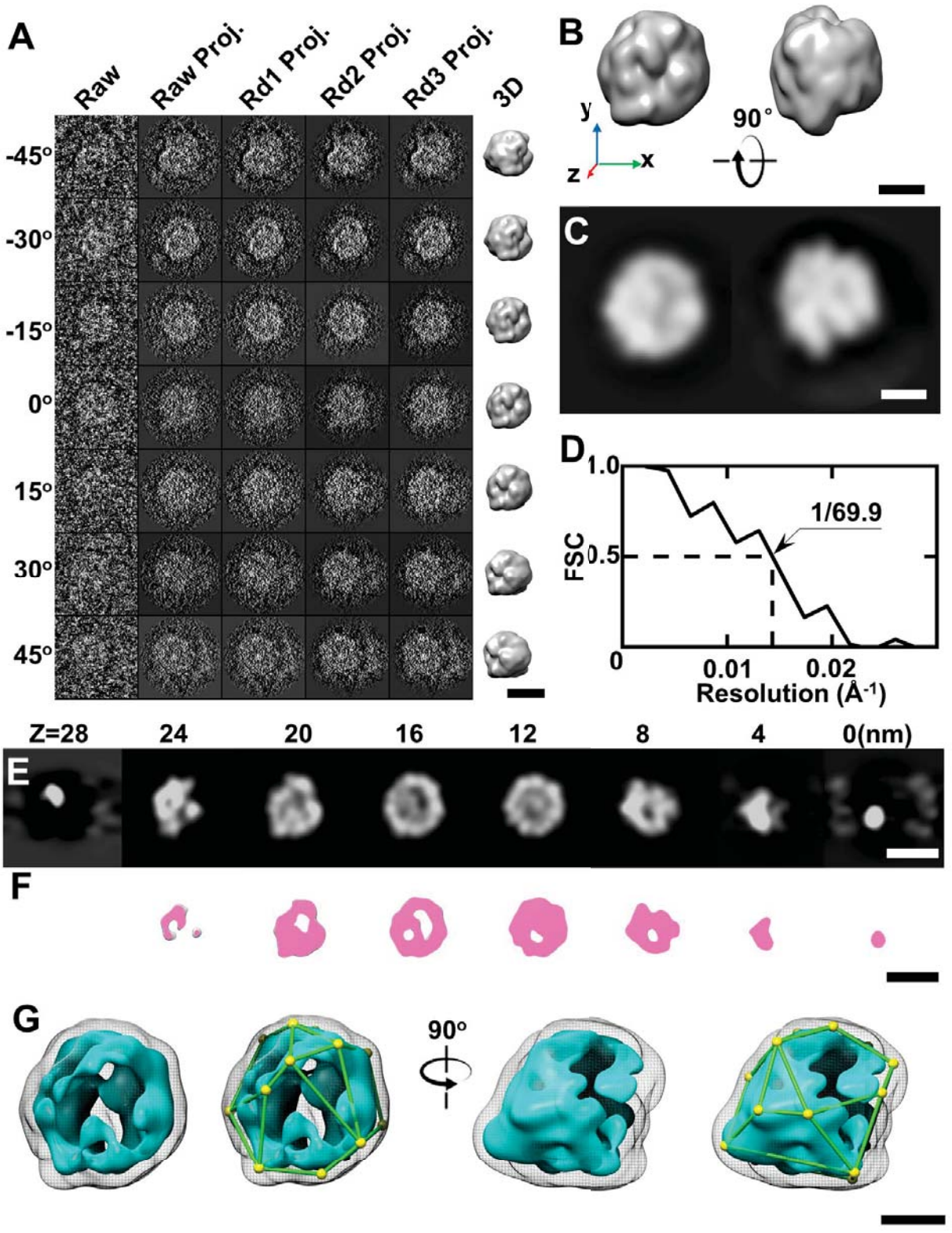

Supplementary Figure S12 | 3D reconstruction of the 13th IDL by IPET (**A**) Seven representative tilt images (image contrast reversed) of the 13th targeted individual IDL particle are displayed in the first column on the left. The tilt images were gradually aligned to a common center via an iterative refinement process to achieve a 3D reconstruction by using IPET. The projections of the raw,

intermediate and final 3D reconstructions are shown based on their corresponding tilt angles. (**B**) Two orthogonal views of the final 3D reconstruction (low-pass filtered at 8 nm). (**C**) 2D projections of the final 3D reconstruction in the same view directions as in subfigure B. (**D**) The resolution of the IPET reconstruction was ~7.0 nm by FSC analyses (based on two density maps reconstructed from odd- and even-numbered tilt images). (**E**) Projection of the 3D map at different Z heights. (**F**) Iso-surface of the 3D map at different Z heights. (**G**) The final map displayed at two different contour levels (high contour level in cyan and low contour level in gray). Scale bars: 20 nm in A, E and F; 10 nm in B, C and G.

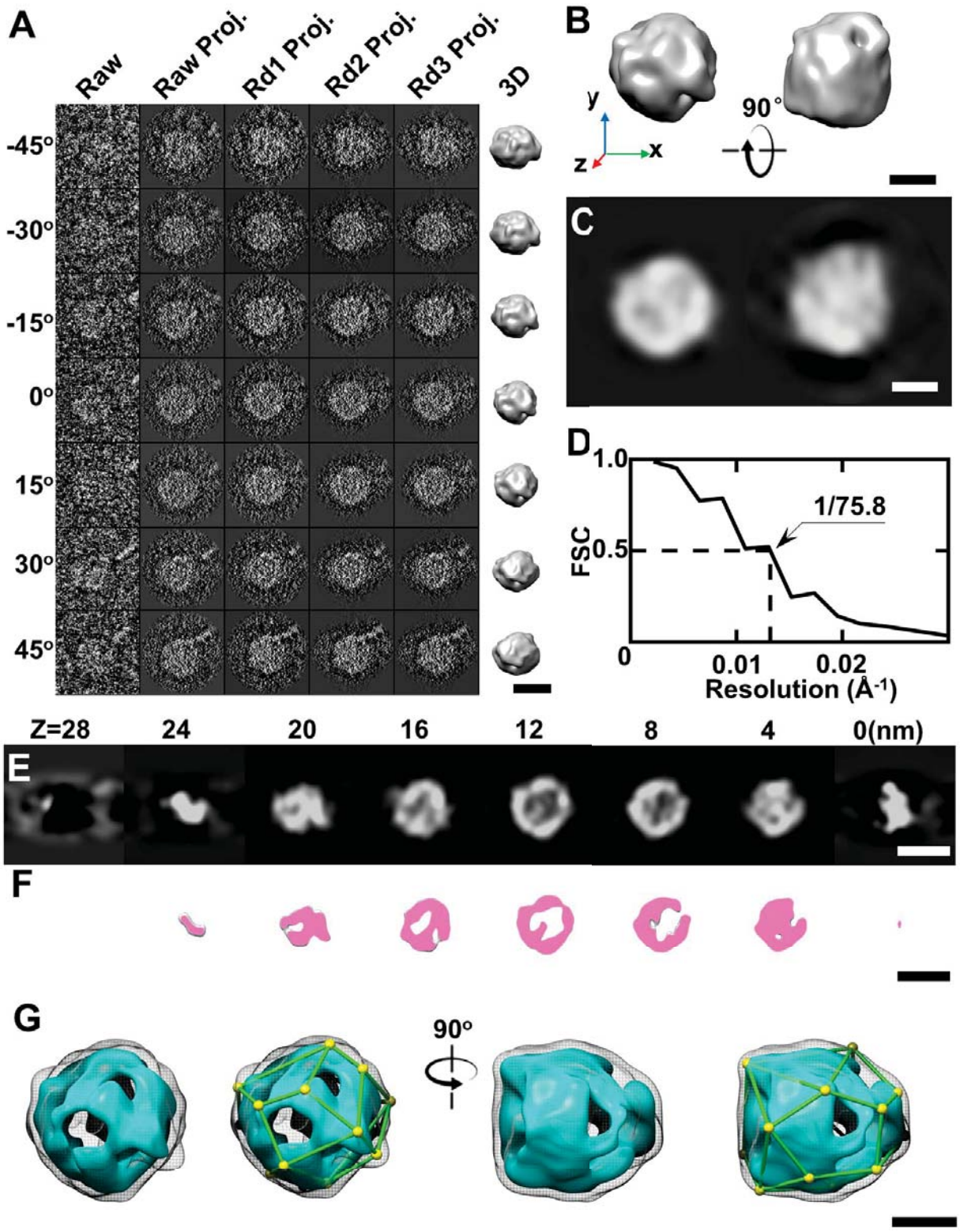

Supplementary Figure S13 | 3D reconstruction of the 14th IDL by IPET (**A**) Seven representative tilt images (image contrast reversed) of the 14th targeted individual IDL particle are displayed in the first column on the left. The tilt images were gradually aligned to a common center via an iterative refinement process to achieve a 3D reconstruction by using IPET. The projections of the raw,

intermediate and final 3D reconstructions are shown based on their corresponding tilt angles. (**B**) Two orthogonal views of the final 3D reconstruction (low-pass filtered at 8 nm). (**C**) 2D projections of the final 3D reconstruction in the same view directions as in subfigure B. (**D**) The resolution of the IPET reconstruction was ~7.6 nm by FSC analyses (based on two density maps reconstructed from odd- and even-numbered tilt images). (**E**) Projection of the 3D map at different Z heights. (**F**) Iso-surface of the 3D map at different Z heights. (**G**) The final map displayed at two different contour levels (high contour level in cyan and low contour level in gray). Scale bars: 20 nm in A, E and F; 10 nm in B, C and G.

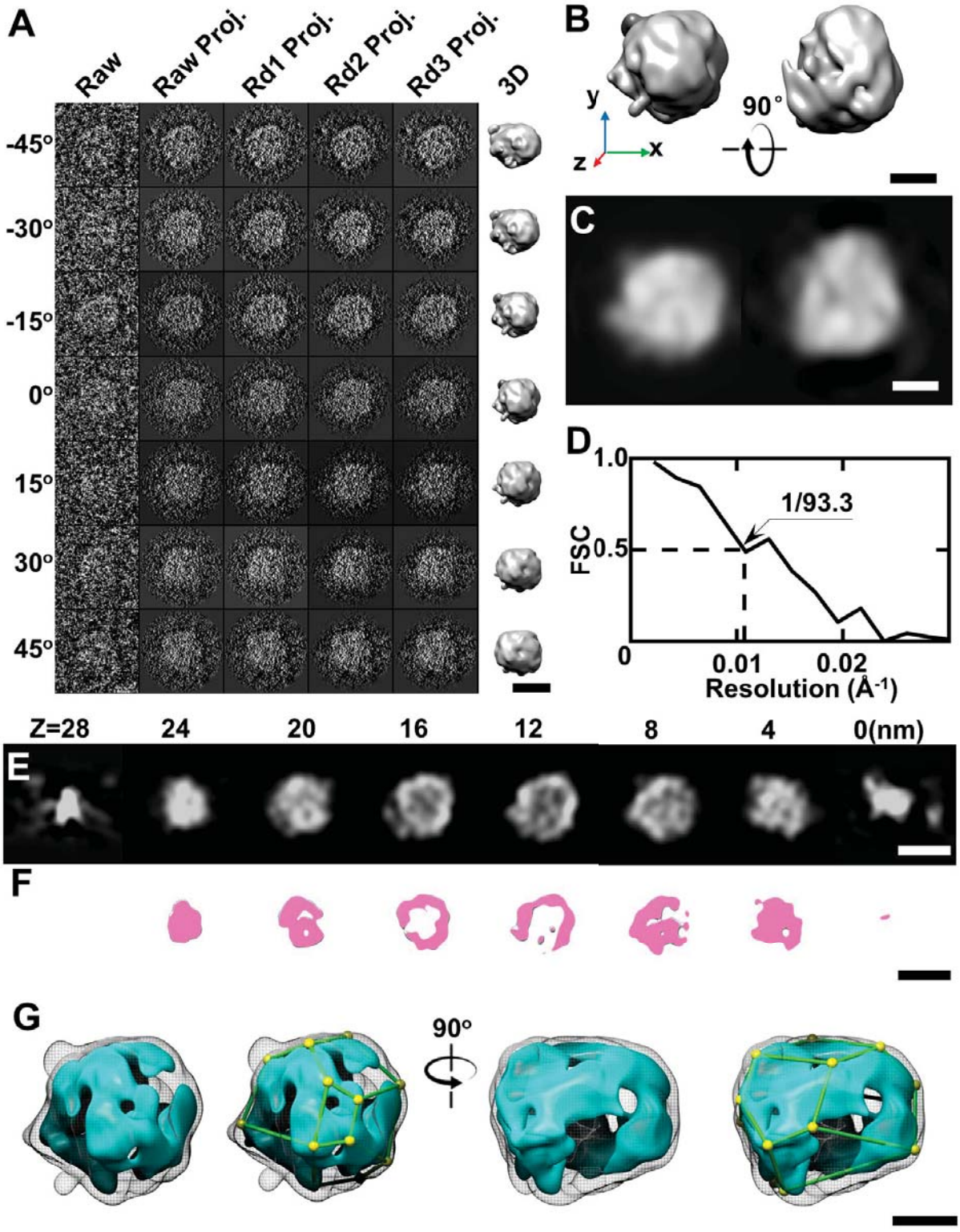

Supplementary Figure S14 | 3D reconstruction of the 15th IDL by IPET (**A**) Seven representative tilt images (image contrast reversed) of the 15th targeted individual IDL particle are displayed in the first column on the left. The tilt images were gradually aligned to a common center via an iterative refinement process to achieve a 3D reconstruction by using IPET. The projections of the raw,

intermediate and final 3D reconstructions are shown based on their corresponding tilt angles. (**B**) Two orthogonal views of the final 3D reconstruction (low-pass filtered at 8 nm). (**C**) 2D projections of the final 3D reconstruction in the same view directions as in subfigure B. (**D**) The resolution of the IPET reconstruction was ~9.3 nm by FSC analyses (based on two density maps reconstructed from odd- and even-numbered tilt images). (**E**) Projection of the 3D map at different Z heights. (**F**) Iso-surface of the 3D map at different Z heights. (**G**) The final map displayed at two different contour levels (high contour level in cyan and low contour level in gray). Scale bars: 20 nm in A, E and F; 10 nm in B, C and G.

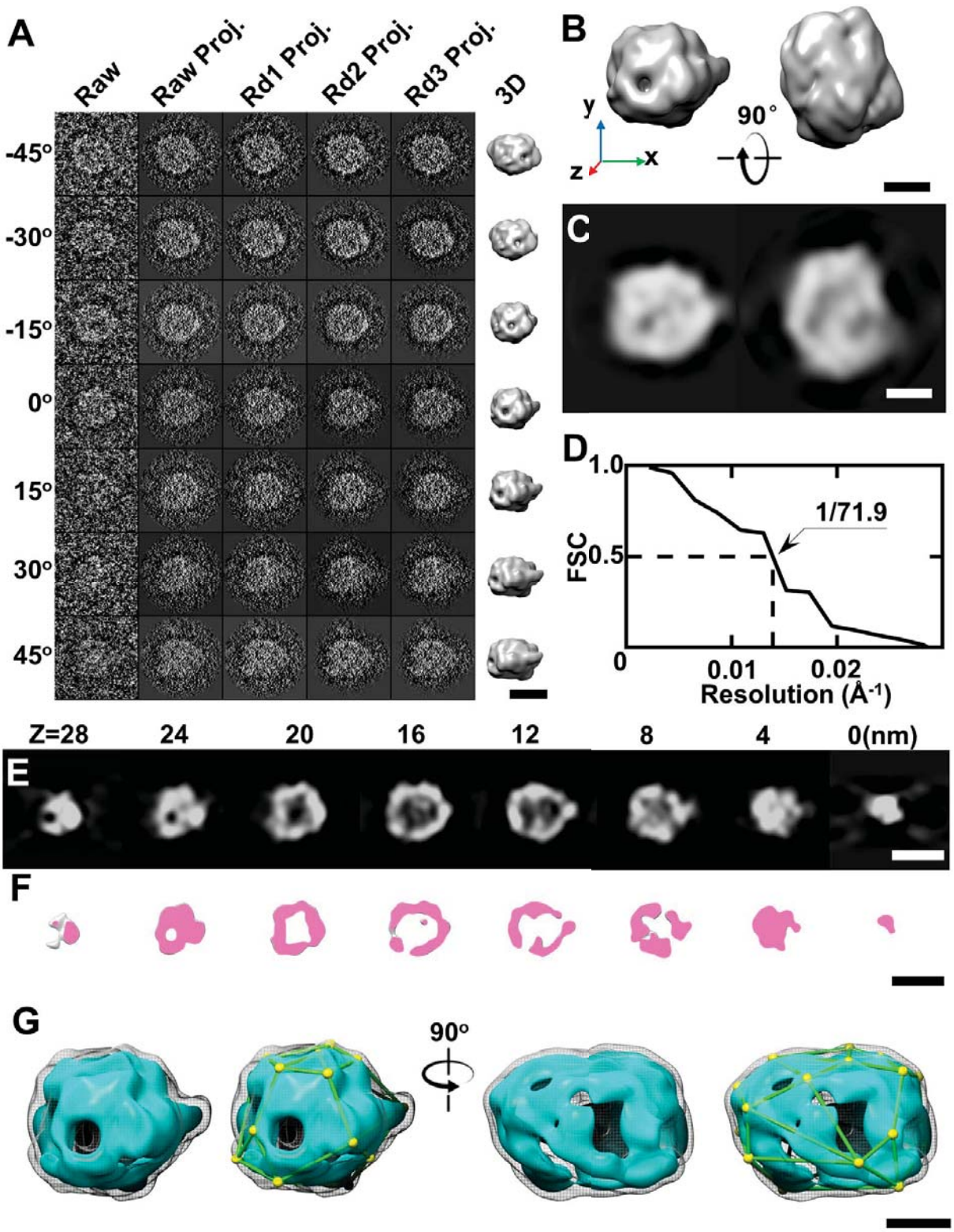

Supplementary Figure S15 | 3D reconstruction of the 16th IDL by IPET (**A**) Seven representative tilt images (image contrast reversed) of the 16th targeted individual IDL particle are displayed in the first column on the left. The tilt images were gradually aligned to a common center via an iterative refinement process to achieve a 3D reconstruction by using IPET. The projections of the raw,

intermediate and final 3D reconstructions are shown based on their corresponding tilt angles. (**B**) Two orthogonal views of the final 3D reconstruction (low-pass filtered at 8 nm). (**C**) 2D projections of the final 3D reconstruction in the same view directions as in subfigure B. (**D**) The resolution of the IPET reconstruction was ~7.2 nm by FSC analyses (based on two density maps reconstructed from odd- and even-numbered tilt images). (**E**) Projection of the 3D map at different Z heights. (**F**) Iso-surface of the 3D map at different Z heights. (**G**) The final map displayed at two different contour levels (high contour level in cyan and low contour level in gray). Scale bars: 20 nm in A, E and F; 10 nm in B, C and G.

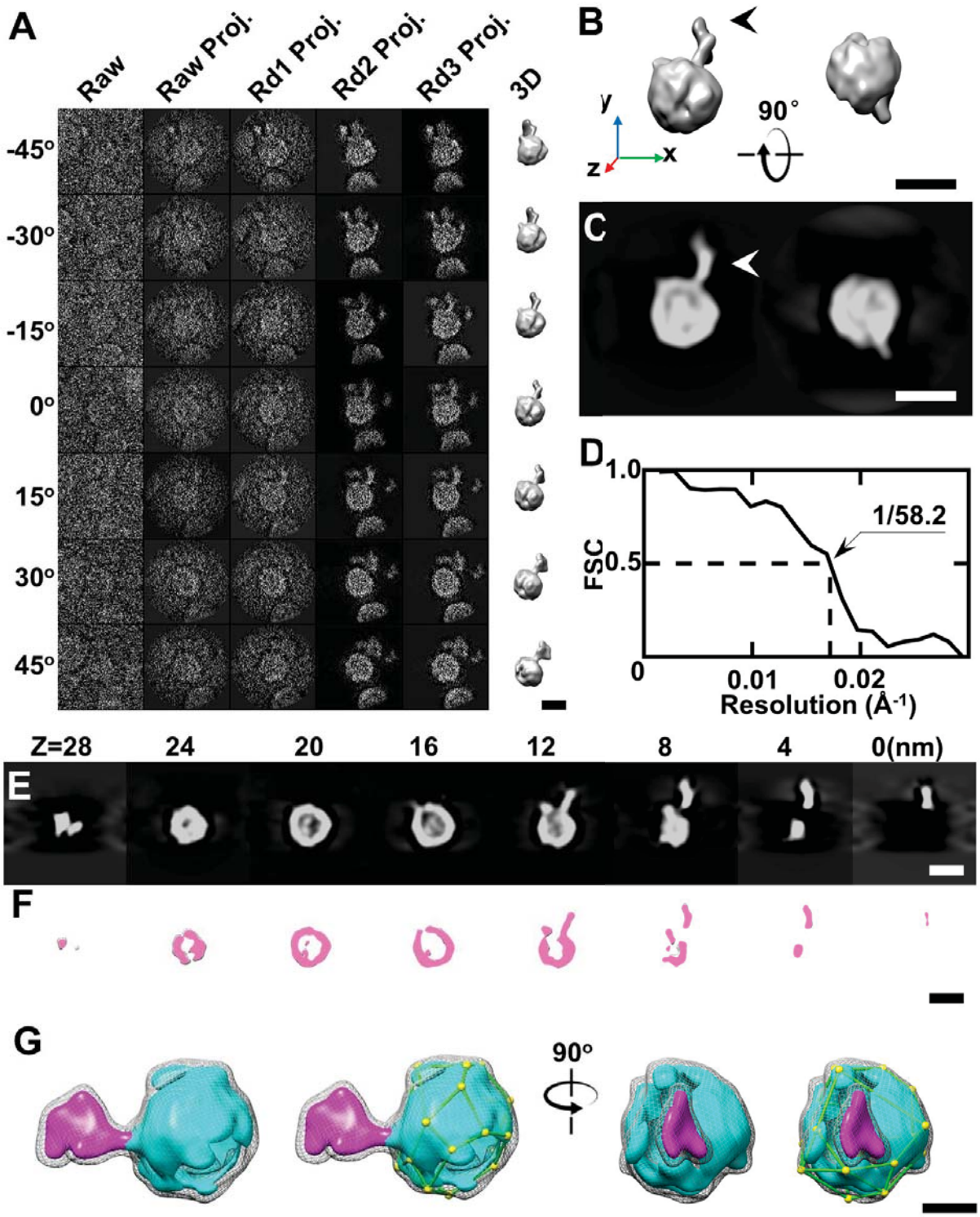

Supplementary Figure S16 | 3D reconstruction of the third IDL-antibody complex by IPET (**A**) Seven representative tilt images (image contrast reversed) of the third targeted individual IDL-antibody particle are displayed in the first column on the left. The tilt images were gradually aligned to a common center via an iterative refinement process to achieve a 3D reconstruction by using IPET. The projections of the raw, intermediate and final 3D reconstructions are shown based on their corresponding tilt angles. (**B**) Two orthogonal views of the final 3D reconstruction (low-pass filtered at 8 nm). (**C**) 2D projections

of the final 3D reconstruction in the same view directions as in subfigure B. (**D**) The resolution of the IPET reconstruction was ~5.8 nm by FSC analyses (based on two density maps reconstructed from odd- and even-numbered tilt images). (**E**) Projection of the 3D map at different Z heights. (**F**) Iso-surface of the 3D map at different Z heights. (**G**) The final map displayed at two different contour levels (high contour level in cyan and low contour level in gray); the antibody portion is shown in pink. Scale bars: 20 nm in A through C, E and F; 10 nm in G.

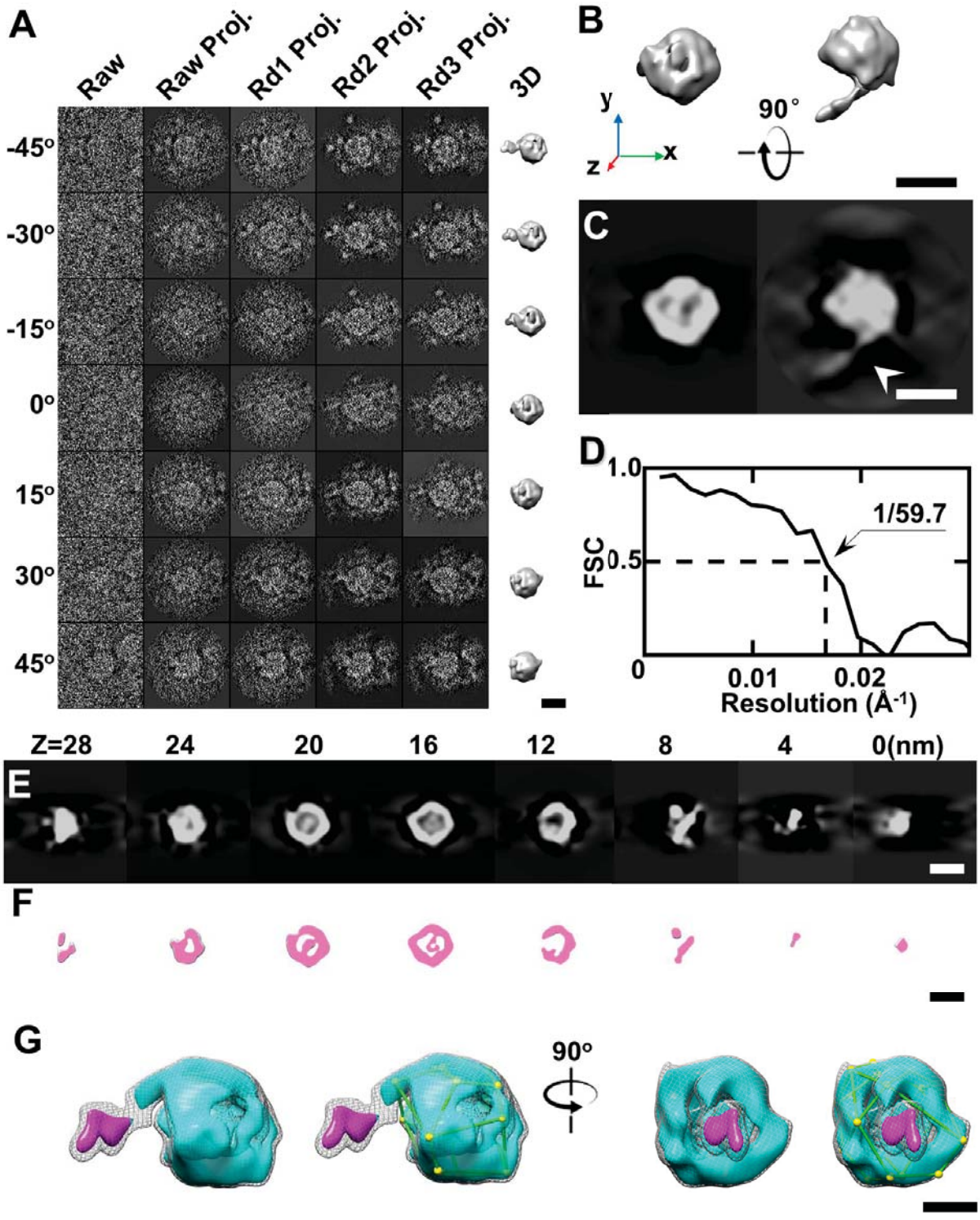

Supplementary Figure S17 | 3D reconstruction of the fourth IDL-antibody complex by IPET (**A**) Seven representative tilt images (image contrast reversed) of the fourth targeted individual IDL-antibody particle are displayed in the first column on the left. The tilt images were gradually aligned to a common center via an iterative refinement process to achieve a 3D reconstruction by using IPET. The projections of the raw, intermediate and final 3D reconstructions are shown based on their corresponding tilt angles. (**B**) Two orthogonal views of the final 3D reconstruction (low-pass filtered at 8 nm). (**C**) 2D projections

of the final 3D reconstruction in the same view directions as in subfigure B. (**D**) The resolution of the IPET reconstruction was ~6.0 nm by FSC analyses (based on two density maps reconstructed from odd- and even-numbered tilt images). (**E**) Projection of the 3D map at different Z heights. (**F**) Iso-surface of the 3D map at different Z heights. (**G**) The final map displayed at two different contour levels (high contour level in cyan and low contour level in gray); the antibody portion is shown in pink. Scale bars: 20 nm in A through C, E and F; 10 nm in G.

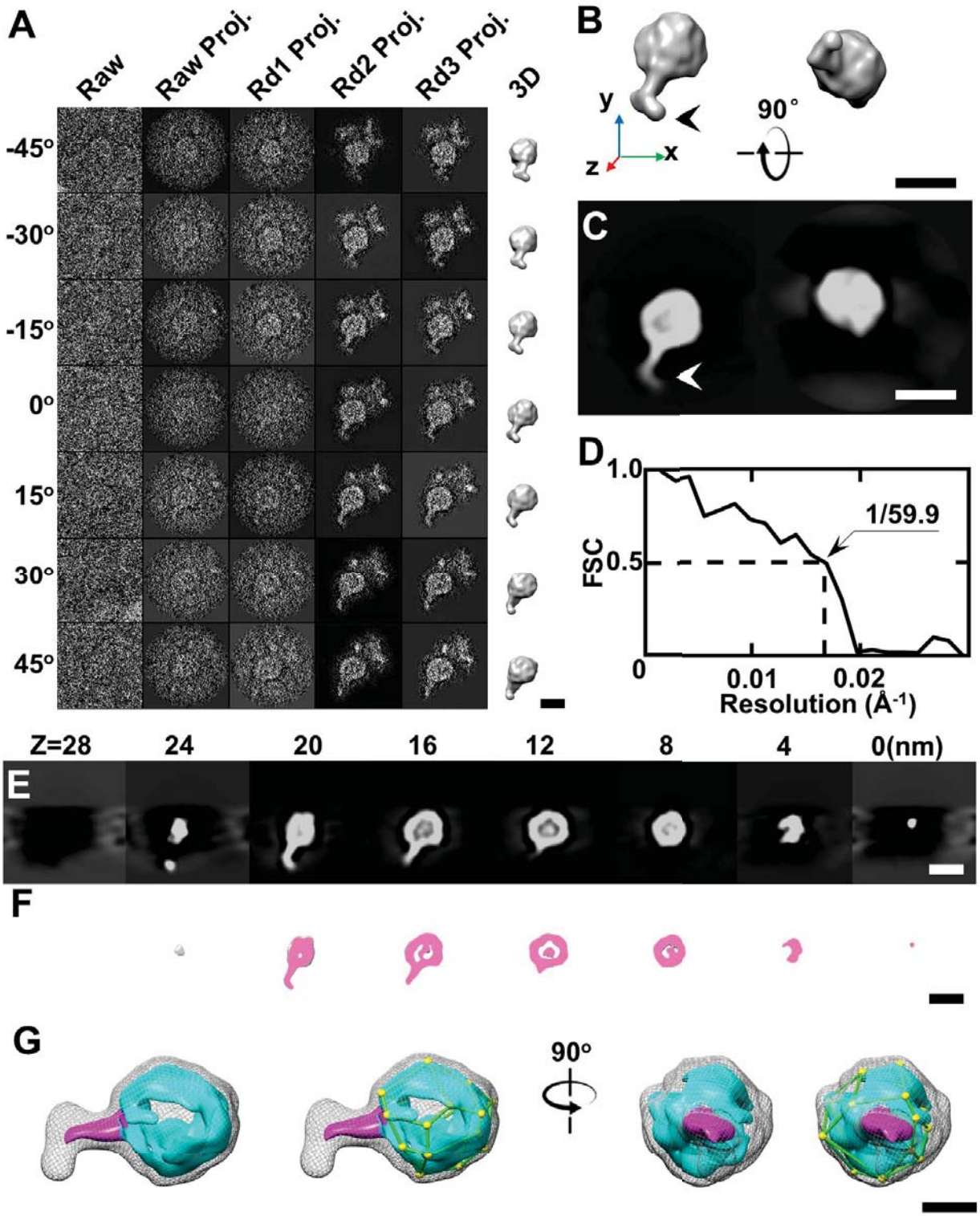

Supplementary Figure S18 | 3D reconstruction of the fifth IDL-antibody complex by IPET (**A**) Seven representative tilt images (image contrast reversed) of the fifth targeted individual IDL-antibody particle are displayed in the first column on the left. The tilt images were gradually aligned to a common center via an iterative refinement process to achieve a 3D reconstruction by using IPET. The projections of the raw, intermediate and final 3D reconstructions are shown based on their corresponding tilt angles.

(**B**) Two orthogonal views of the final 3D reconstruction (low-pass filtered at 8 nm). (**C**) 2D projections of the final 3D reconstruction in the same view directions as in subfigure B. (**D**) The resolution of the IPET reconstruction was ~6.0 nm by FSC analyses (based on two density maps reconstructed from odd- and even-numbered tilt images). (**E**) Projection of the 3D map at different Z heights. (**F**) Iso-surface of the 3D map at different Z heights. (**G**) The final map displayed at two different contour levels (high contour level in cyan and low contour level in gray); the antibody portion is shown in pink. Scale bars: 20 nm in A through C, E and F; 10 nm in G.

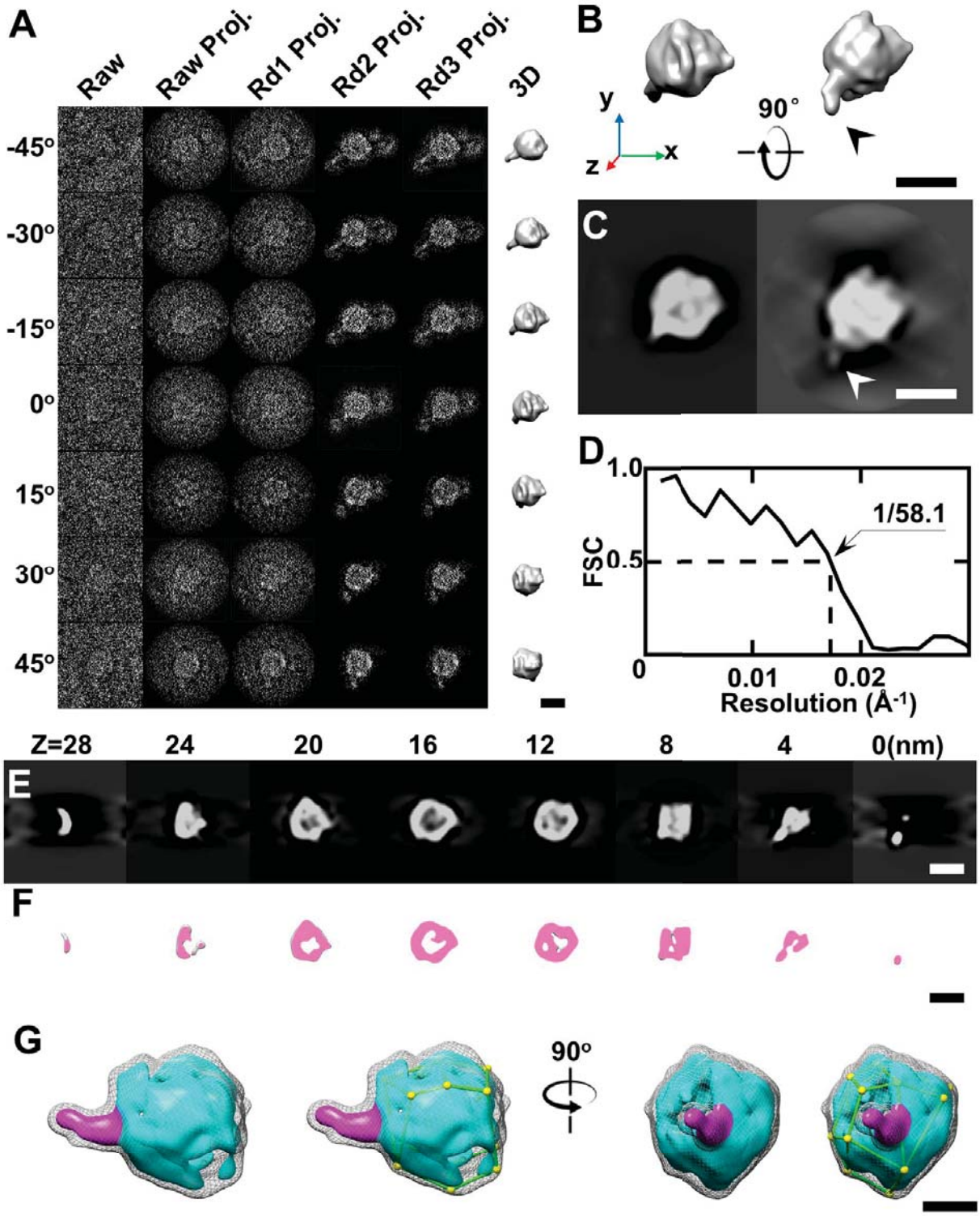

Supplementary Figure S19 | 3D reconstruction of the sixth IDL-antibody complex by IPET (**A**) Seven representative tilt images (image contrast reversed) of the sixth targeted individual IDL-antibody particle are displayed in the first column on the left. The tilt images were gradually aligned to a common center via an iterative refinement process to achieve a 3D reconstruction by using IPET. The projections of the raw, intermediate and final 3D reconstructions are shown based on their corresponding tilt angles.

(**B**) Two orthogonal views of the final 3D reconstruction (low-pass filtered at 8 nm). (**C**) 2D projections of the final 3D reconstruction in the same view directions as in subfigure B. (**D**) The resolution of the IPET reconstruction was ~5.8 nm by FSC analyses (based on two density maps reconstructed from odd- and even-numbered tilt images). (**E**) Projection of the 3D map at different Z heights. (**F**) Iso-surface of the 3D map at different Z heights. (**G**) The final map displayed at two different contour levels (high contour level in cyan and low contour level in gray); the antibody portion is shown in pink. Scale bars: 20 nm in A through C, E and F; 10 nm in G.

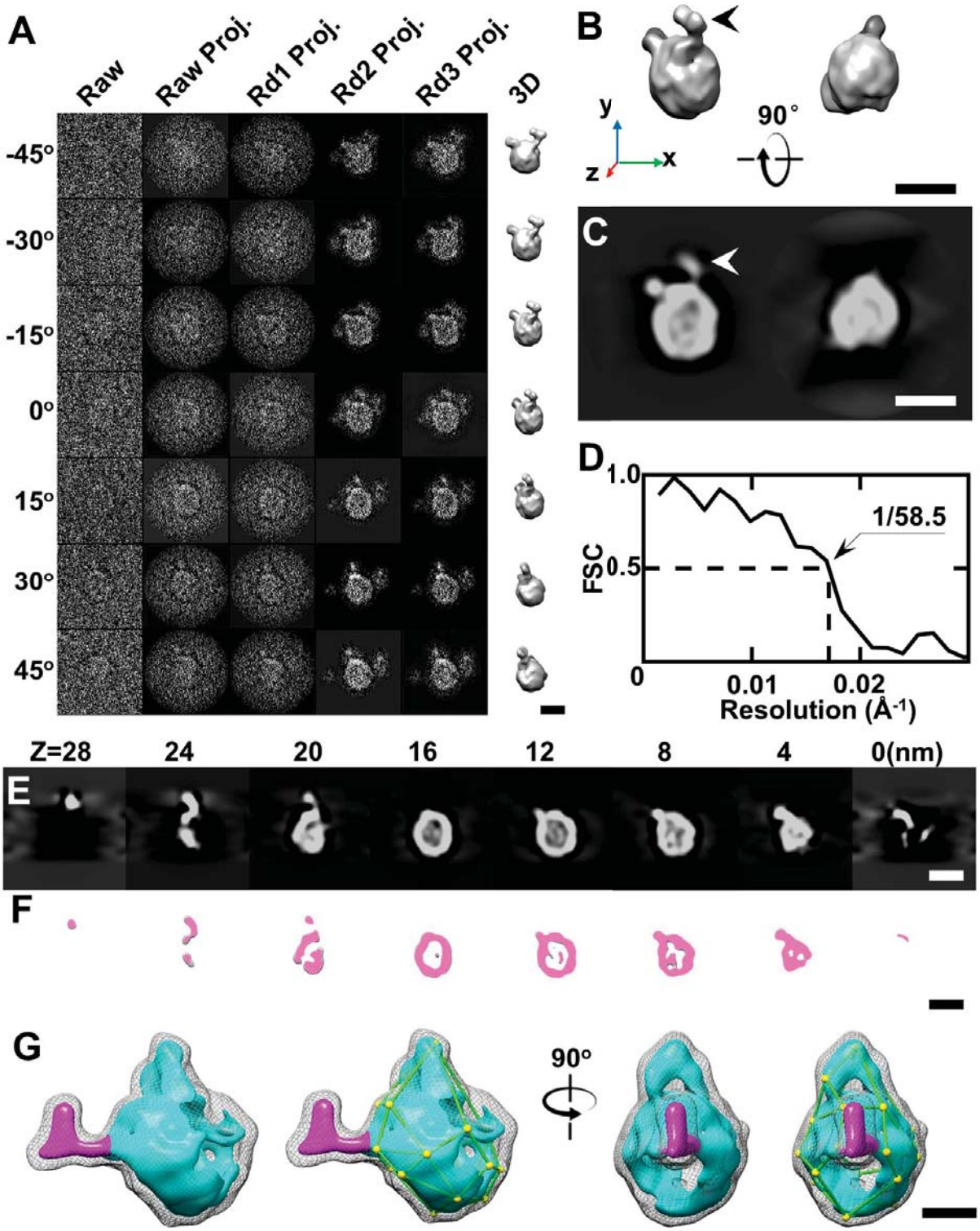

Supplementary Figure S20 | 3D reconstruction of the seventh IDL-antibody complex by IPET (**A**) Seven representative tilt images (image contrast reversed) of the seventh targeted individual IDL-antibody particle are displayed in the first column on the left. The tilt images were gradually aligned to a common center via an iterative refinement process to achieve a 3D reconstruction by using IPET. The projections of the raw, intermediate and final 3D reconstructions are shown based on their corresponding

tilt angles. (**B**) Two orthogonal views of the final 3D reconstruction (low-pass filtered at 8 nm). (**C**) 2D projections of the final 3D reconstruction in the same view directions as in subfigure B. (**D**) The resolution of the IPET reconstruction was ~5.9 nm by FSC analyses (based on two density maps reconstructed from odd- and even-numbered tilt images). (**E**) Projection of the 3D map at different Z heights. (**F**) Iso-surface of the 3D map at different Z heights. (**G**) The final map displayed at two different contour levels (high contour level in cyan and low contour level in gray); the antibody portion is shown in pink. Scale bars: 20 nm in A through C, E and F; 10 nm in G.

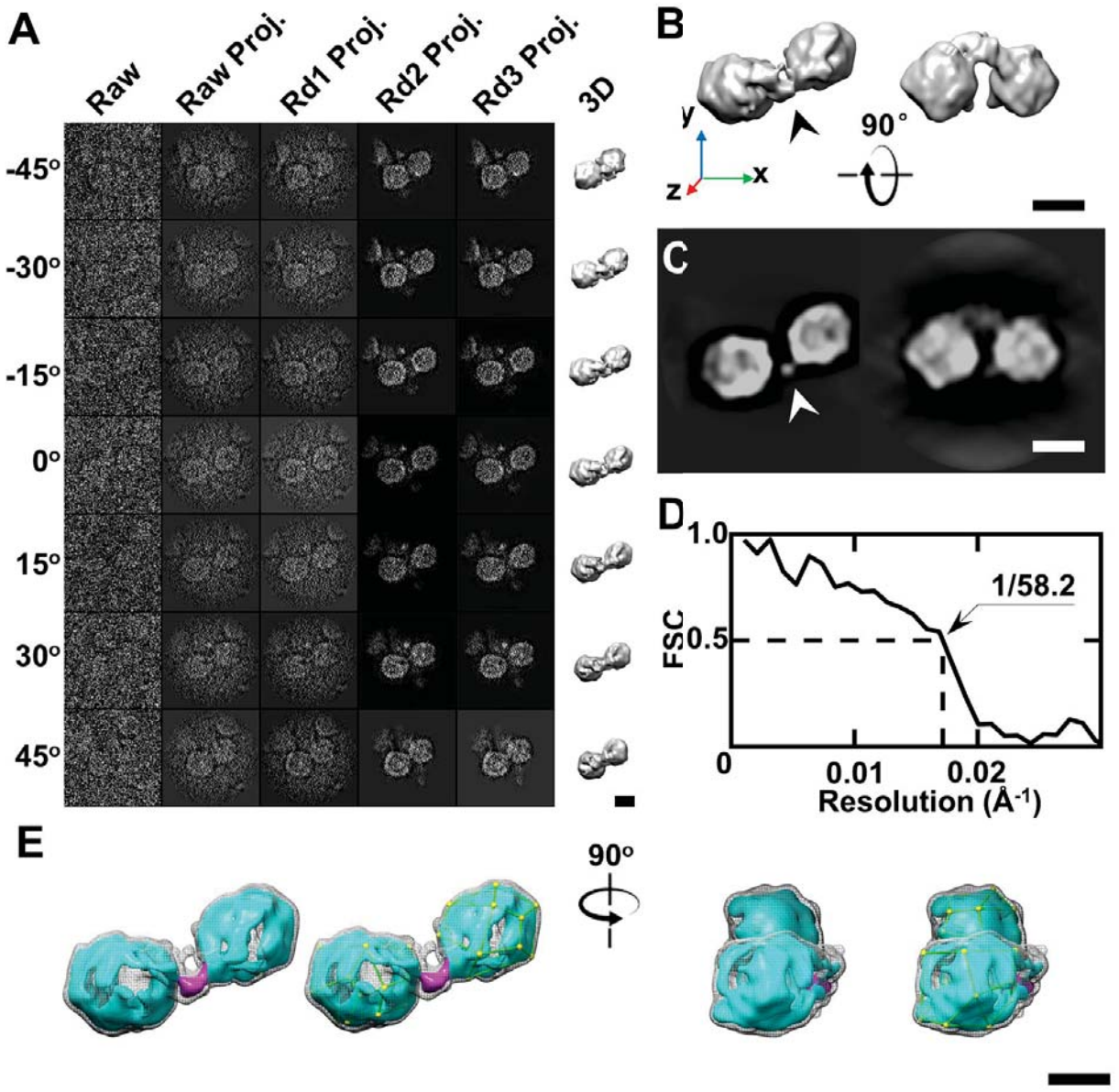

Supplementary Figure S21 | 3D reconstruction of the second IDL-antibody-IDL complex by IPET (**A**) Seven representative tilt images (image contrast reversed) of the second targeted individual IDL-antibody-IDL particle are displayed in the first column on the left. The tilt images were gradually aligned to a common center via an iterative refinement process to achieve a 3D reconstruction by using IPET. The projections of the raw, intermediate and final 3D reconstructions are shown based on their corresponding tilt angles. (**B**) Two orthogonal views of the final 3D reconstruction (low-pass filtered at 8 nm). (**C**) 2D projections of the final 3D reconstruction in the same view directions as in subfigure B. (**D**) The resolution of the IPET reconstruction was ~5.8 nm by FSC analyses (based on two density maps reconstructed from odd- and even-numbered tilt images). (**E**) The final map displayed at two different contour levels (high contour level in cyan and low contour level in gray); the antibody portion is shown in pink. Scale bars: 20 nm in A through C; 10 nm in E.

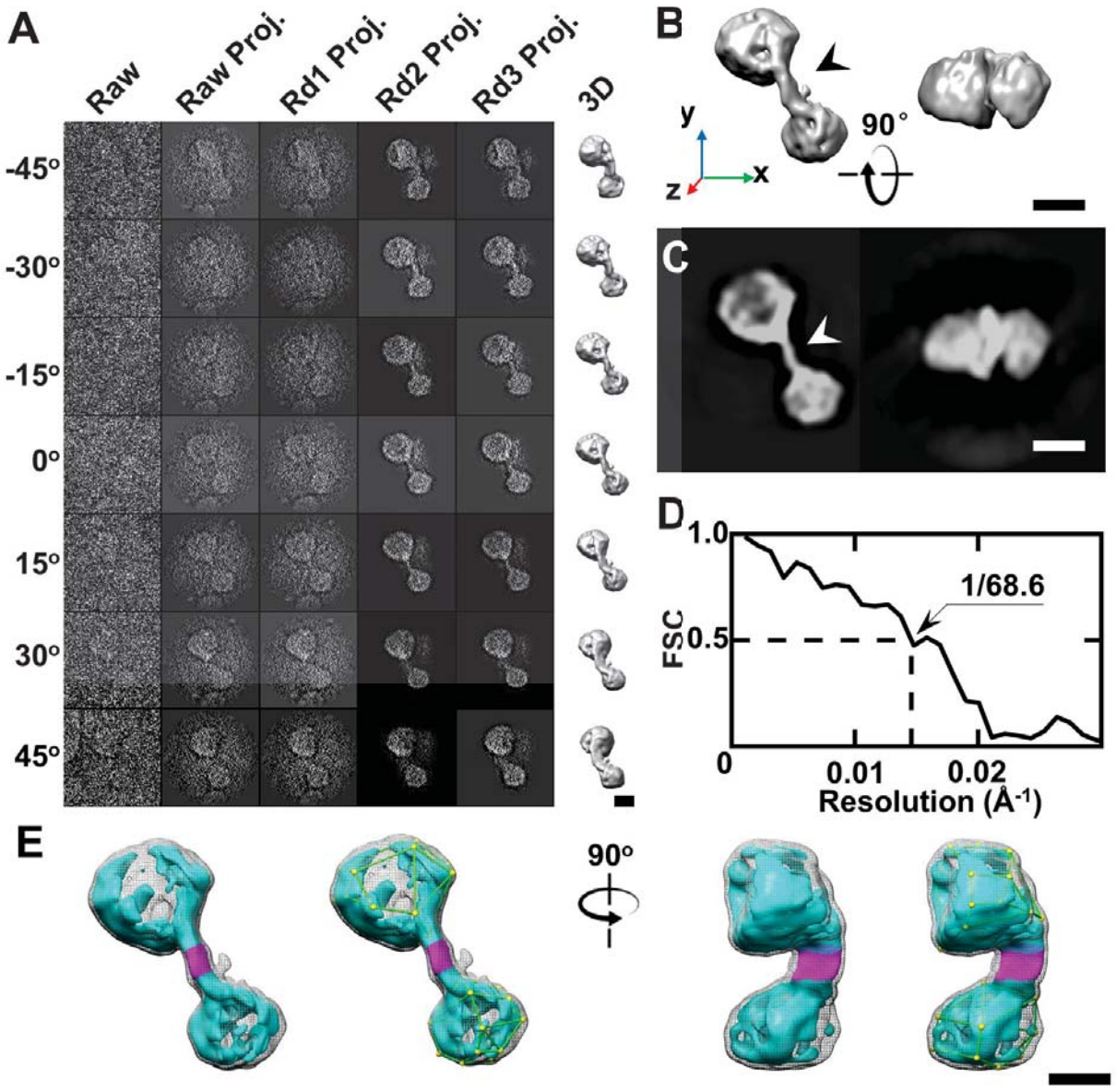

Supplementary Figure S22 | 3D reconstruction of the third IDL-antibody-IDL complex by IPET (**A**) Seven representative tilt images (image contrast reversed) of the third targeted individual IDL-antibody-IDL particle are displayed in the first column on the left. The tilt images were gradually aligned to a common center via an iterative refinement process to achieve a 3D reconstruction by using IPET. The projections of the raw, intermediate and final 3D reconstructions are shown based on their corresponding tilt angles. (**B**) Two orthogonal views of the final 3D reconstruction (low-pass filtered at 8 nm). (**C**) 2D projections of the final 3D reconstruction in the same view directions as in subfigure B. (**D**) The resolution of the IPET reconstruction was ~6.9 nm by FSC analyses (based on two density maps reconstructed from odd- and even-numbered tilt images). (**E**) The final map displayed at two different contour levels (high contour level in cyan and low contour level in gray); the antibody portion is shown in pink. Scale bars: 20 nm in A through C; 10 nm in E.

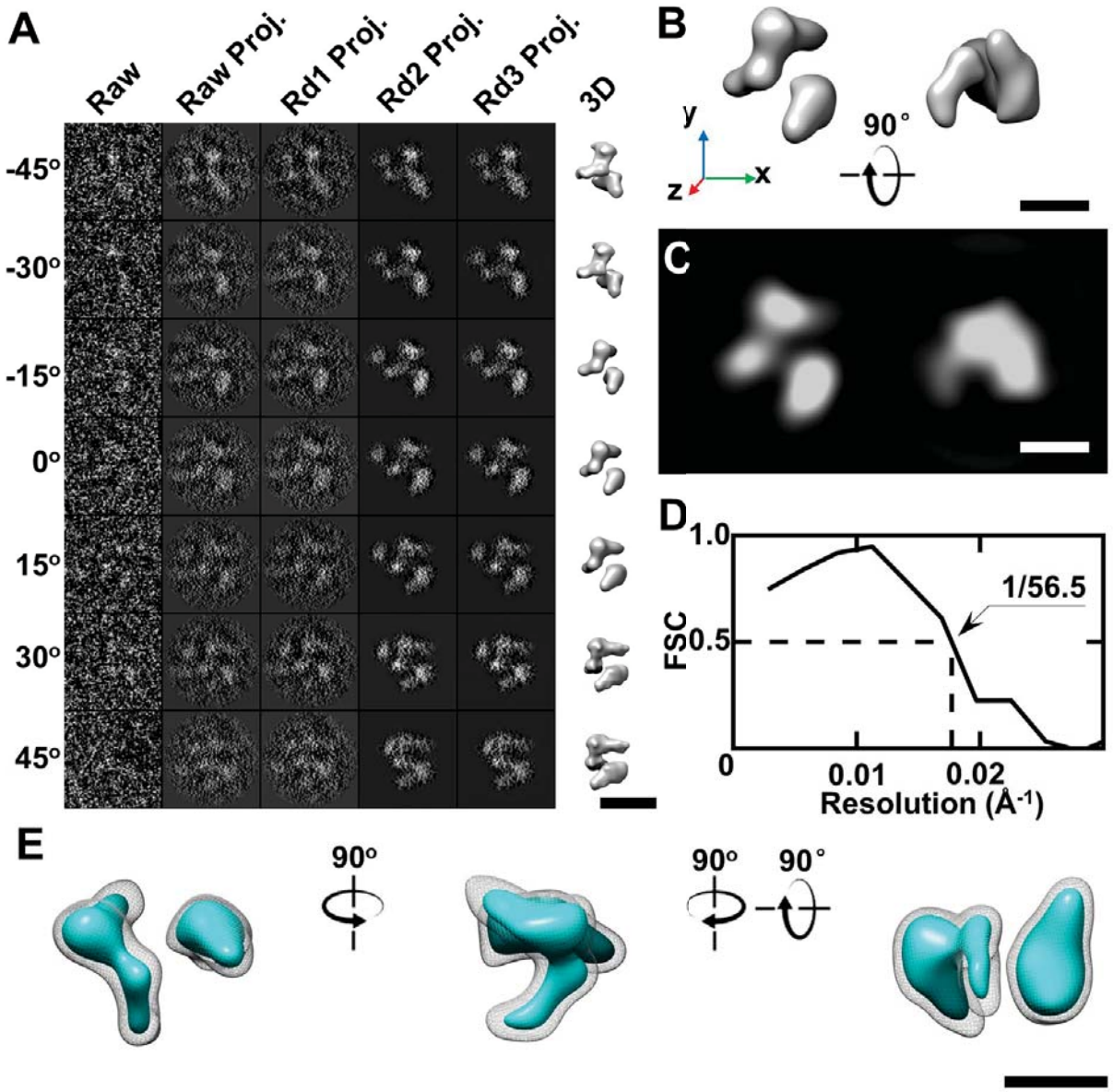

Supplementary Figure S23 | 3D reconstruction of the second antibody by IPET (**A**) Seven representative tilt images (image contrast reversed) of the second targeted individual antibody particle are displayed in the first column on the left. The tilt images were gradually aligned to a common center via an iterative refinement process to achieve a 3D reconstruction by using IPET. The projections of the raw, intermediate and final 3D reconstructions are shown based on their corresponding tilt angles. (**B**) Two orthogonal views of the final 3D reconstruction (low-pass filtered at 8 nm). (**C**) 2D projections of the final 3D reconstruction in the same view directions as in subfigure B. (D) The resolution of the IPET reconstruction was ~5.7 nm by FSC analyses (based on two density maps reconstructed from odd- and even-numbered tilt images). (**E**) The final map displayed at two different contour levels (high contour level in cyan and low contour level in gray). Scale bars: 20 nm in A; 10 nm in B, C and E.

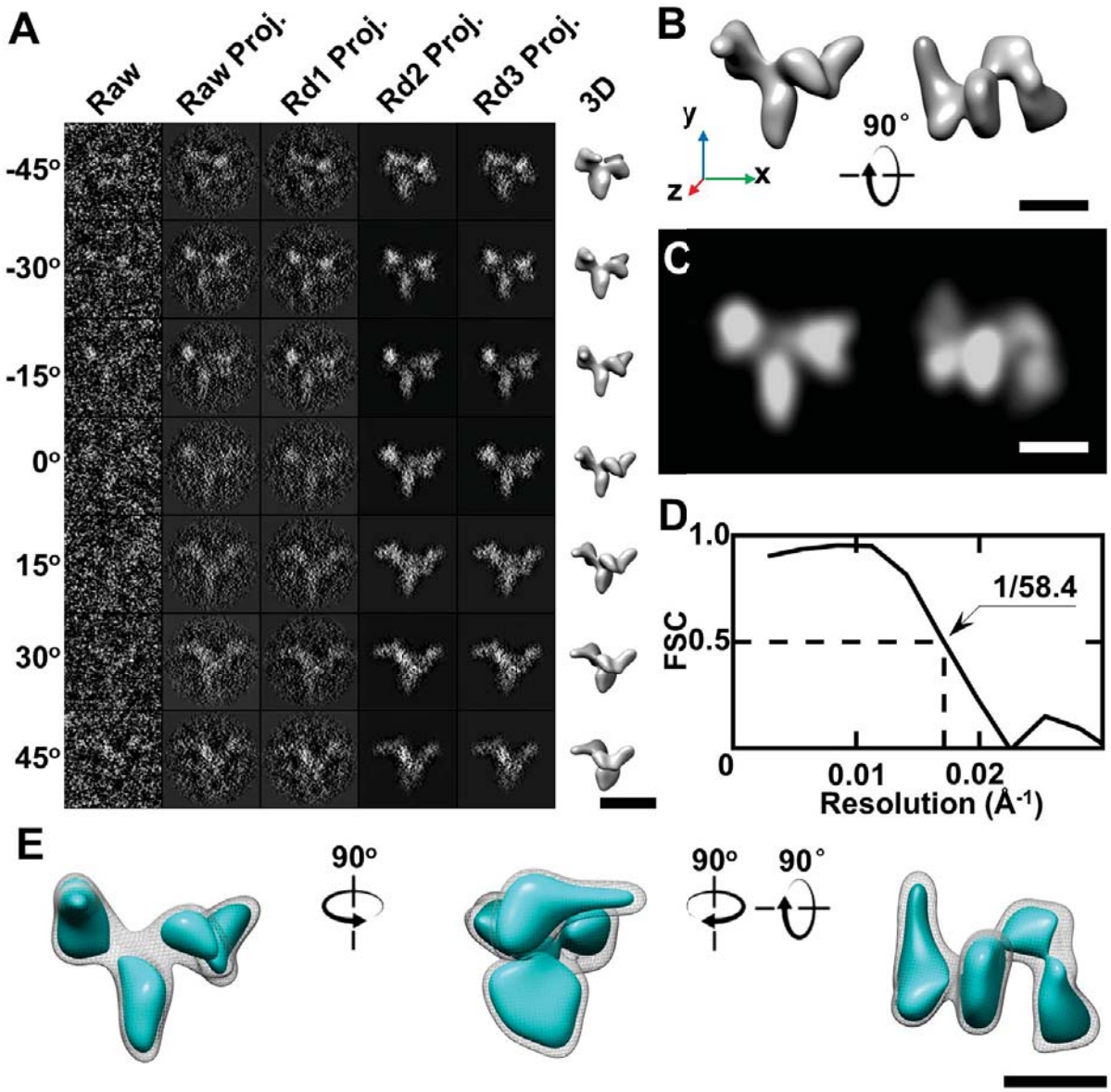

Supplementary Figure S24 | 3D reconstruction of the third antibody by IPET (**A**) Seven representative tilt images (image contrast reversed) of the third targeted individual antibody particle are displayed in the first column on the left. The tilt images were gradually aligned to a common center via an iterative refinement process to achieve a 3D reconstruction by using IPET. The projections of the raw, intermediate and final 3D reconstructions are shown based on their corresponding tilt angles. (**B**) Two orthogonal views of the final 3D reconstruction (low-pass filtered at 8 nm). (**C**) 2D projections of the final 3D reconstruction in the same view directions as in subfigure B. (**D**) The resolution of the IPET reconstruction was ~5.8 nm by FSC analyses (based on two density maps reconstructed from odd- and even-numbered tilt images). (**E**) The final map displayed at two different contour levels (high contour level in cyan and low contour level in gray). Scale bars: 20 nm in A; 10 nm in B, C and E.

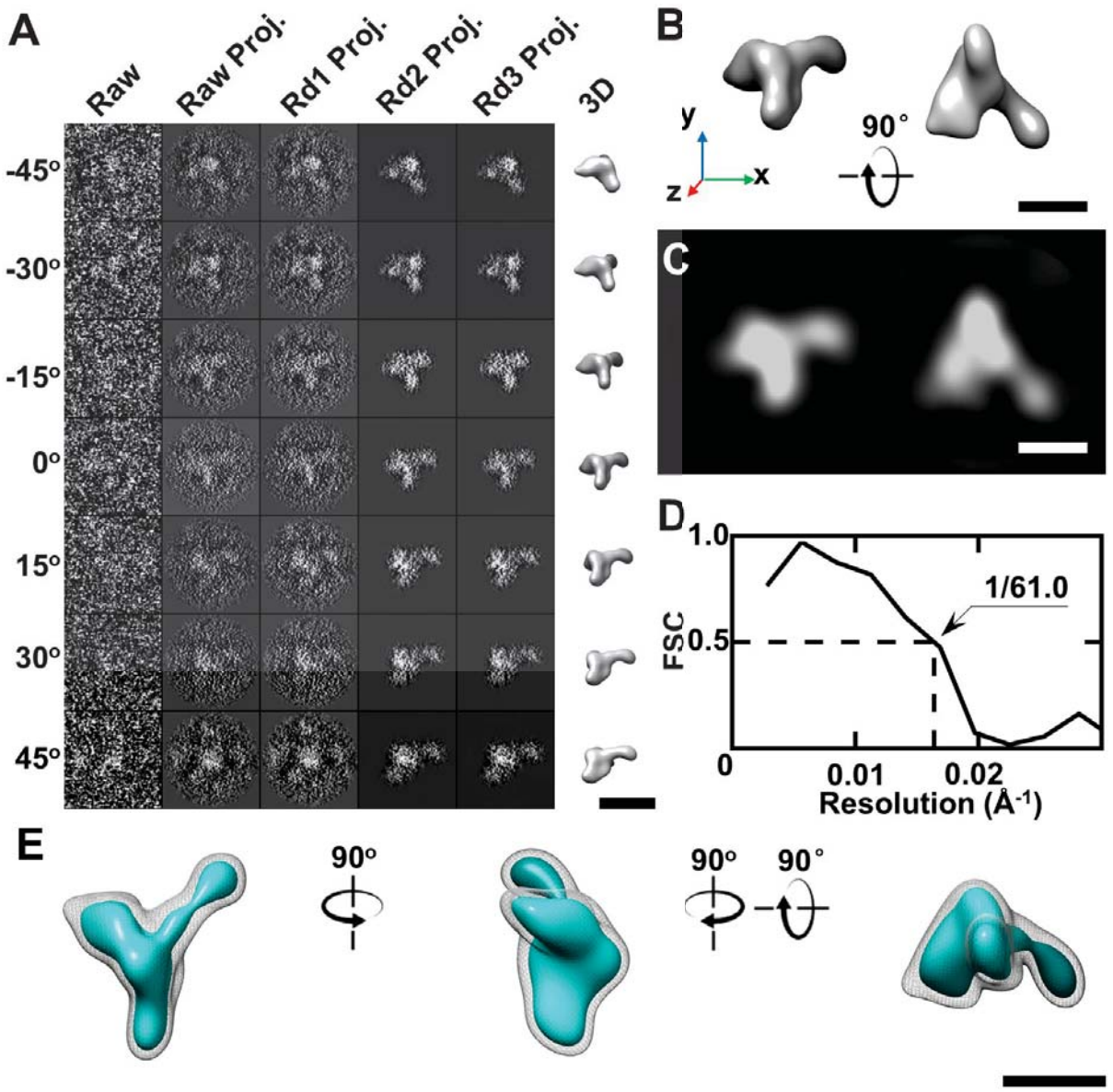

Supplementary Figure S25 | 3D reconstruction of the fourth antibody by IPET (**A**) Seven representative tilt images (image contrast reversed) of the fourth targeted individual antibody particle are displayed in the first column on the left. The tilt images were gradually aligned to a common center via an iterative refinement process to achieve a 3D reconstruction by using IPET. The projections of the raw, intermediate and final 3D reconstructions are shown based on their corresponding tilt angles. (**B**) Two orthogonal views of the final 3D reconstruction (low-pass filtered at 8 nm). (**C**) 2D projections of the final 3D reconstruction in the same view directions as in subfigure B. (**D**) The resolution of the IPET reconstruction was ~6.1 nm by FSC analyses (based on two density maps reconstructed from odd- and even-numbered tilt images). (**E**) The final map displayed at two different contour levels (high contour level in cyan and low contour level in gray). Scale bars: 20 nm in A; 10 nm in B, C and E.

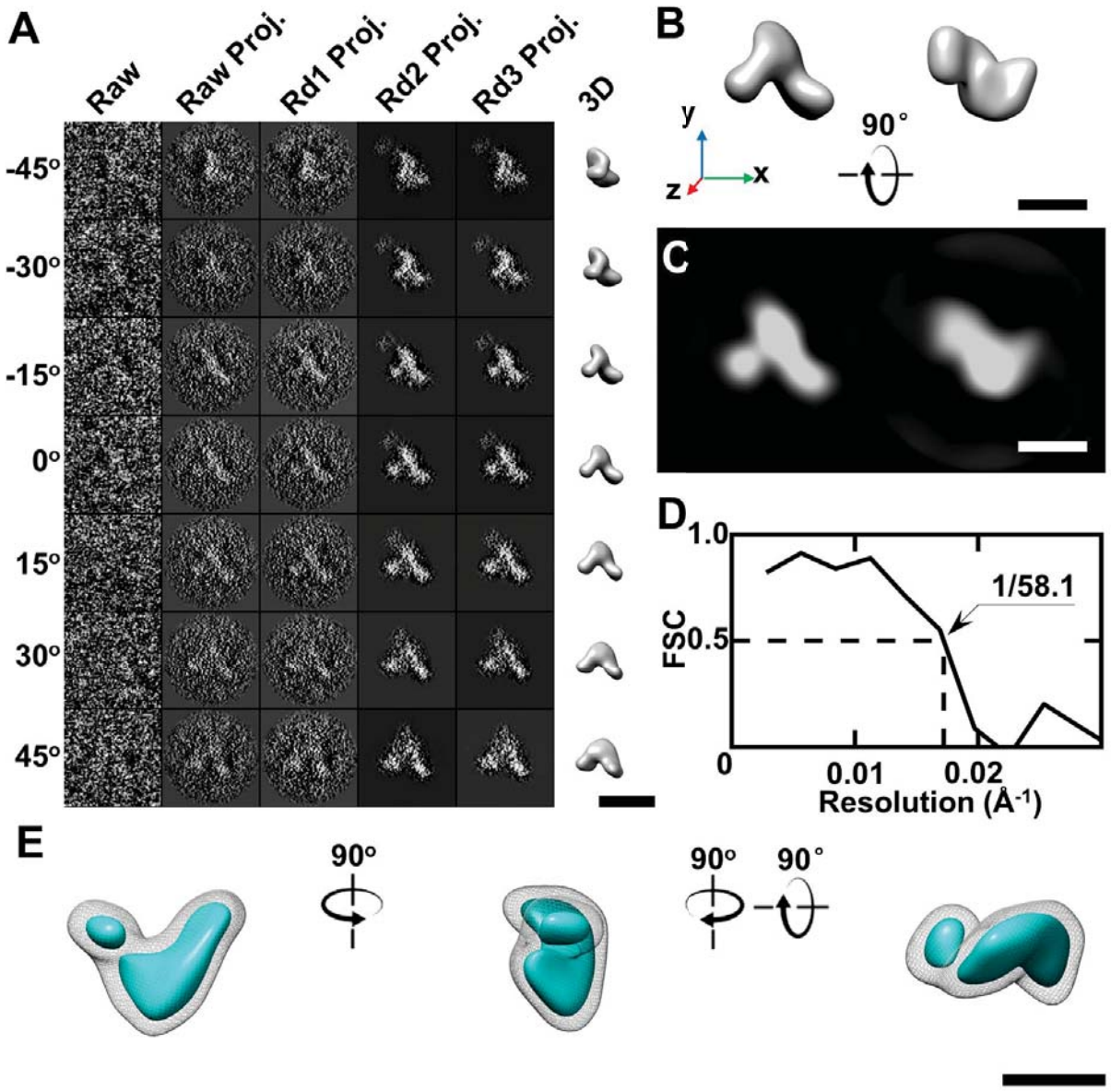

Supplementary Figure S26 | 3D reconstruction of the fifth antibody by IPET (**A**) Seven representative tilt images (image contrast reversed) of the fifth targeted individual antibody particle are displayed in the first column on the left. The tilt images were gradually aligned to a common center via an iterative refinement process to achieve a 3D reconstruction by using IPET. The projections of the raw, intermediate and final 3D reconstructions are shown based on their corresponding tilt angles. (**B**) Two orthogonal views of the final 3D reconstruction (low-pass filtered at 8 nm). (**C**) 2D projections of the final 3D reconstruction in the same view directions as in subfigure B. (**D**) The resolution of the IPET reconstruction was ~5.8 nm by FSC analyses (based on two density maps reconstructed from odd- and even-numbered tilt images). (**E**) The final map displayed at two different contour levels (high contour level in cyan and low contour level in gray). Scale bars: 20 nm in A; 10 nm in B, C and E.

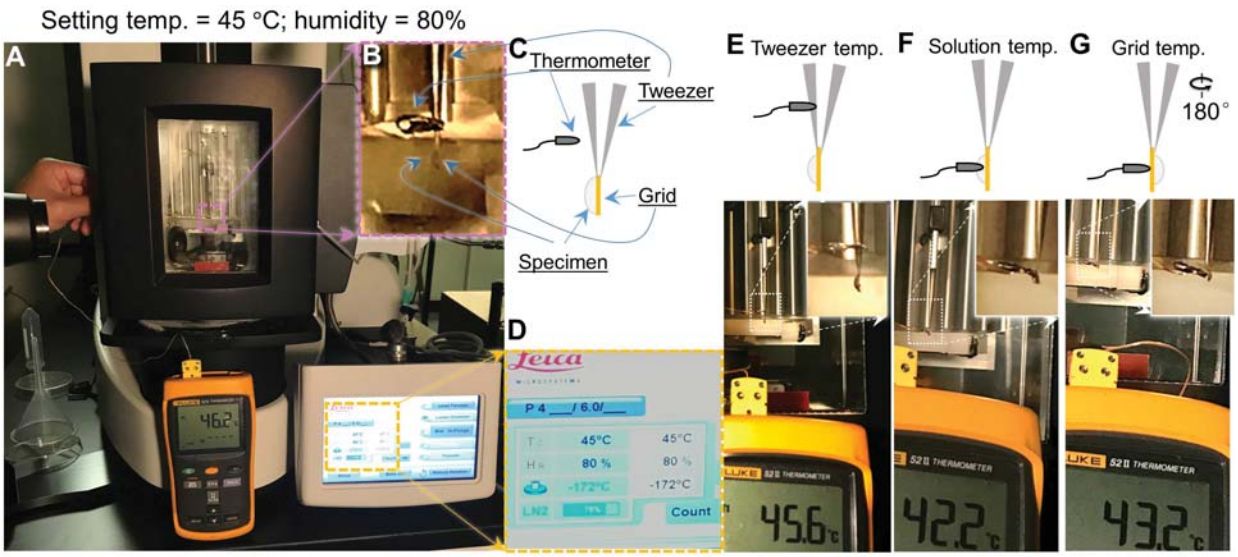

Supplementary Figure S27 | Measuring the temperatures under setting temperature of 45 °C and the humidity of 80% prior to vitrification (**A**) The chamber of Leica EM automatic plunge freezer was set at the targeted temperature of 45 °C and the humidity of 80%. **(B)** A thermometer was used to physically touch to the targeted area to measure the local temperature. **(C)** The schematics of the thermometer touching a targeted area, such as the tweezer. **(D)** After the chamber achieved its setting temperature and humidity, the temperatures were measured via a thermometer. **(E)** The temperature near the tweezer tip was measured as 45.6 °C. **(F)** The temperature of the specimen (sample solution) was measured as 42.2 °C, while **(G)** the temperature of the EM grid was measured as 43.2 °C.

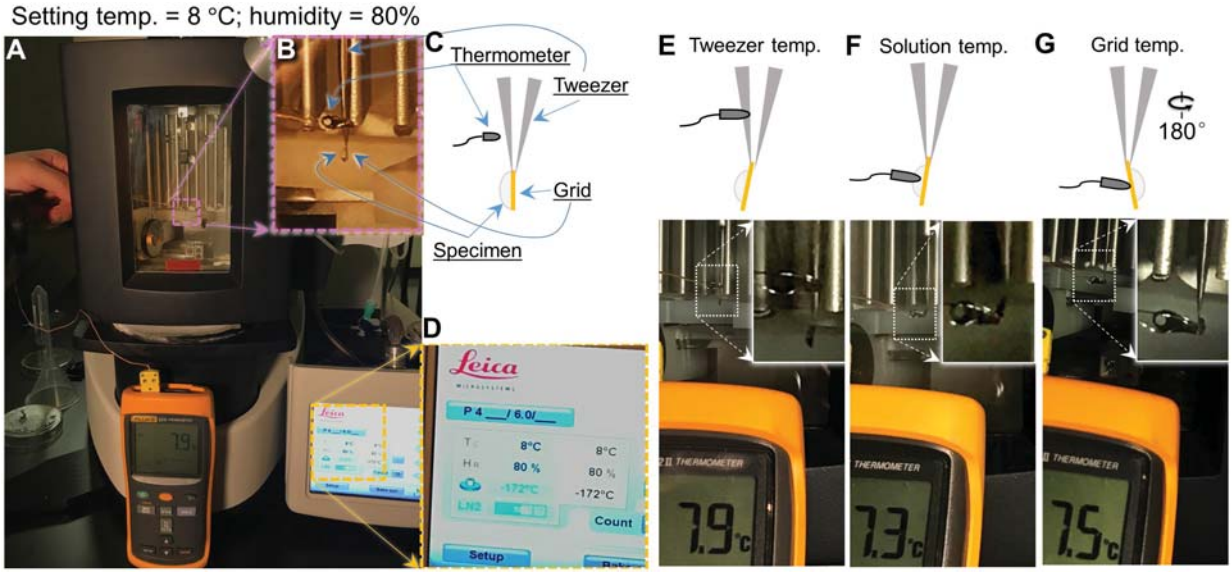

Supplementary Figure S28 | Measuring the temperatures under setting temperature of 8 °C and the humidity of 80% prior to vitrification (**A**) The chamber of Leica EM automatic plunge freezer was set at the targeted temperature of 8 °C and the humidity of 80%. **(B)** A thermometer was used to physically touch to the targeted area to measure the local temperature. **(C)** The schematics of the thermometer touching a targeted area, such as the tweezer. **(D)** After the chamber achieved its setting temperature and humidity, the temperatures were measured via a thermometer. **(E)** The temperature near the tweezer tip was measured as 7.9 °C. **(F)** The temperature of the specimen (sample solution) was measured as 7.3 °C, while **(G)** the temperature of the EM grid was measured as 7.5 °C.

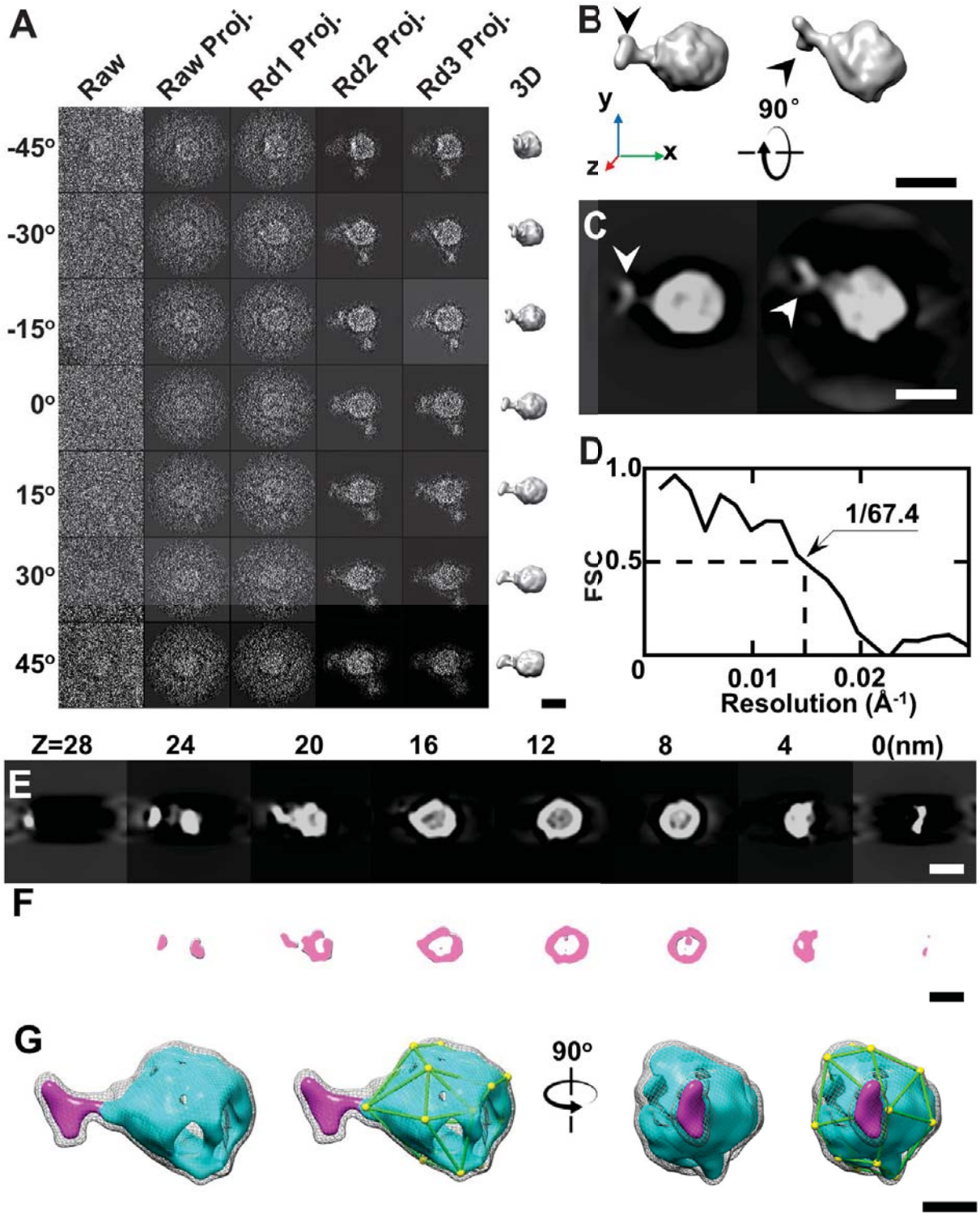

Supplementary Figure S29 | 3D reconstruction of the first IDL-antibody complex by IPET with CTF amplitude corrections (**A**) Seven representative tilt images (image contrast reversed) of the first targeted individual IDL-antibody particle (after CTF amplitude correction by the Wiener filter under two parameters of 0.5 and 0.25 using TOMOCTF software) are displayed in the first column on the left. The tilt images had been submitted to CTF amplitude and phase correction before IPET 3D reconstruction.

The projections of the raw, intermediate and final 3D reconstructions are shown based on their corresponding tilt angles. (**B**) Two orthogonal views of the final 3D reconstruction (low-pass filtered at 8 nm). (**C**) 2D projections of the final 3D reconstruction in the same view directions as in subfigure B. (**D**) The resolution of the IPET reconstruction was ~6.7 nm by FSC analyses (based on two density maps reconstructed from odd- and even-numbered tilt images). (**E**) Projection of the 3D map at different Z heights. (**F**) Iso-surface of the 3D map at different Z heights. (**G**) The final map displayed at two different contour levels (high contour level in cyan and low contour level in gray mesh); the antibody portion is shown in pink. Scale bars: 20 nm in A through C, E and F; 10 nm in G.

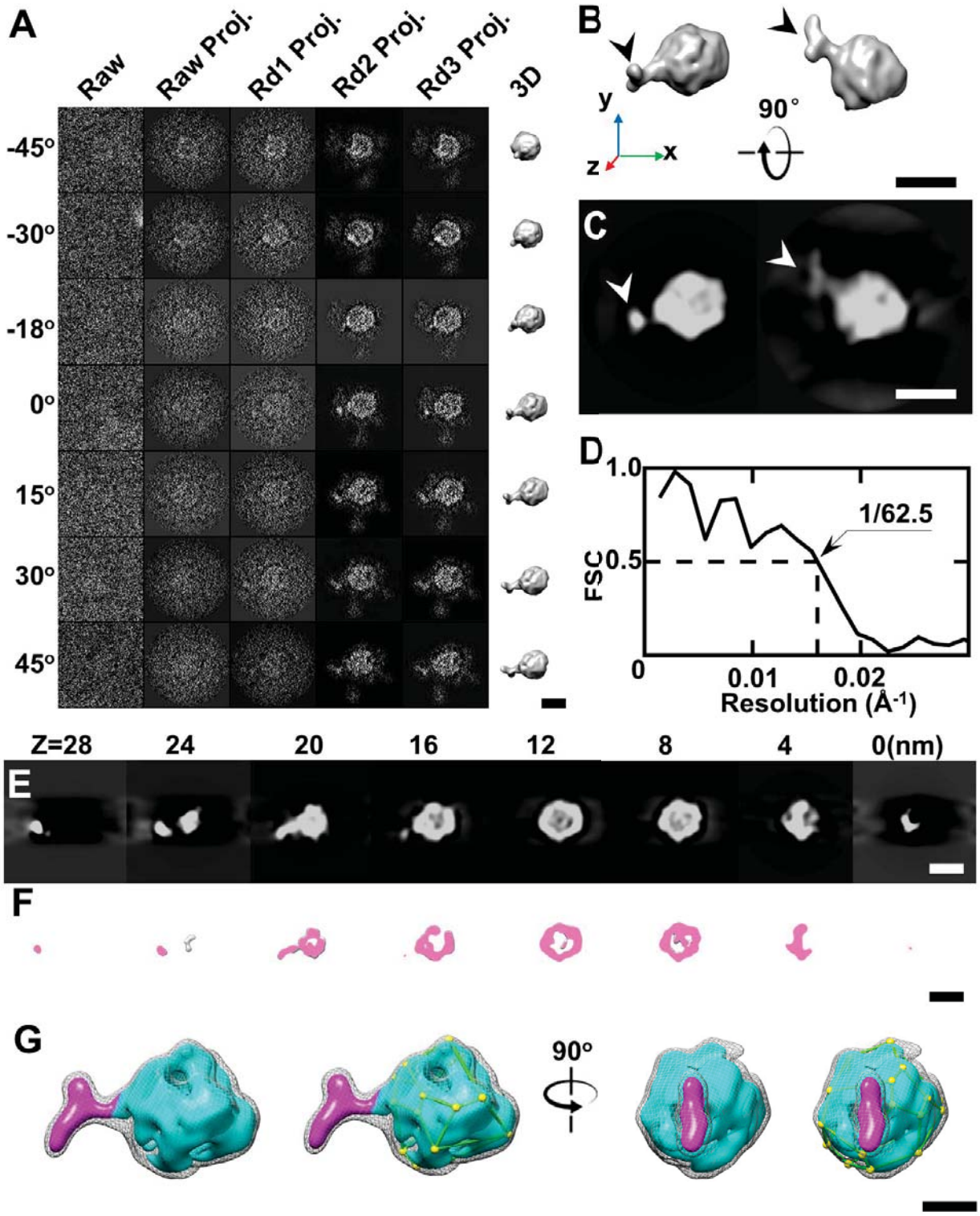

Supplementary Figure S30 | 3D reconstruction of the second IDL-antibody complex by IPET with CTF amplitude corrections (**A**) Seven representative tilt images (image contrast reversed) of the second targeted individual IDL-antibody particle (after CTF amplitude correction by the Wiener filter under two parameters of 0.5 and 0.25 using TOMOCTF software) are displayed in the first column on the left. The tilt images had been submitted to CTF amplitude and phase correction before IPET 3D

reconstruction. The projections of the raw, intermediate and final 3D reconstructions are shown based on their corresponding tilt angles. (**B**) Two orthogonal views of the final 3D reconstruction (low-pass filtered at 8 nm). (**C**) 2D projections of the final 3D reconstruction in the same view directions as in subfigure B. (**D**) The resolution of the IPET reconstruction was ~6.3 nm by FSC analyses (based on two density maps reconstructed from odd- and even-numbered tilt images). (**E**) Projection of the 3D map at different Z heights. (**F**) Iso-surface of the 3D map at different Z heights. (**G**) The final map displayed at two different contour levels (high contour level in cyan and low contour level in gray mesh); the antibody portion is shown in pink. Scale bars: 20 nm in A through C, E and F; 10 nm in G.

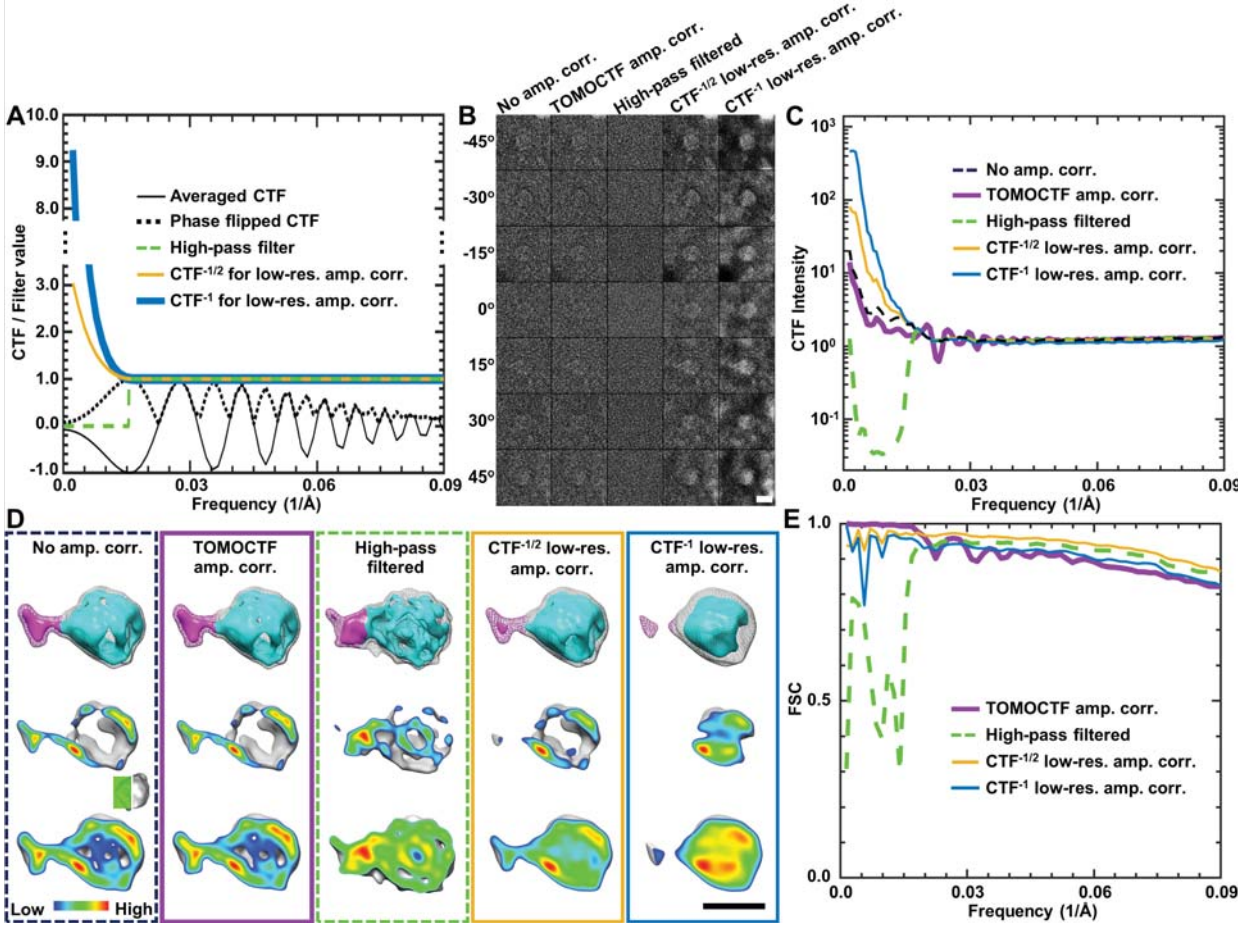

Supplementary Figure S31 | 3D reconstruction of the first IDL-antibody complex based on different CTF amplitude corrections (**A**) The averaged CTF, and high-pass, $CTF^{-1/2}$ and CTF^{-1} filters for modifying the low-resolution amplitude before the first CTF peak of the first targeted IDL-antibody particle. **(B)** Seven representative tilt images (image contrast reversed) under different CTF amplitude modifications: (i) no CTP amplitude modification (only the phase flipped, first column); (ii) a CTF amplitude correction by the Wiener filter using TOMOCTF (second column); (iii) a high-pass filter at the first peak of CTF (third column); (iv) a low resolution amplitude correction by multiplying the images amplitudes by the reciprocal of the square root of low resolution averaged CTF (fourth column); (v) a low resolution amplitude correction by multiplying the image amplitudes by the reciprocal of the low resolution averaged CTF (fifth column). The images were phase flipped before any CTF amplitude modification. (**C**) The power spectrum of resulted images. (**D**) The 3D maps reconstructed from the images. The maps are displayed at two different contour levels in the first row (high contour level in cyan and low contour level in gray mesh), with antibody portion shown in pink. The cut-away surface views of the maps at the two contour levels are shown in the second and third rows. (**E**) The FSC curves between the maps without and with amplitude modifications. Scale bars: 20 nm.

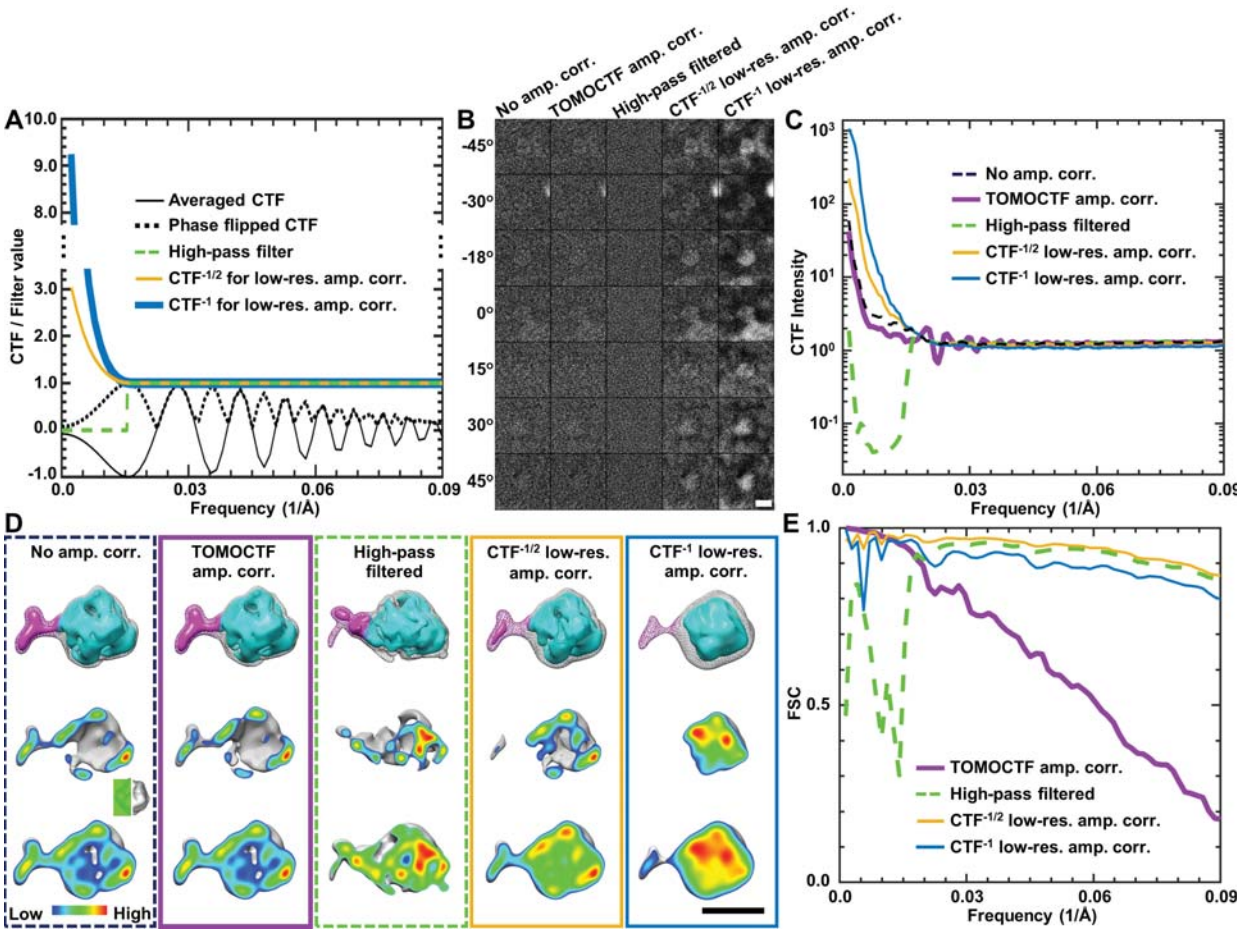

Supplementary Figure S32 | 3D reconstruction of the second IDL-antibody complex based on different CTF amplitude corrections (**A**) The averaged CTF, and high-pass, $CTF^{-1/2}$ and CTF^{-1} filters for modifying the low-resolution amplitude before the first CTF peak of the second targeted IDL-antibody particle. **(B)** Seven representative tilt images (image contrast reversed) under different CTF amplitude modifications: (i) no CTP amplitude modification (only the phase flipped, first column); (ii) a CTF amplitude correction by the Wiener filter using TOMOCTF (second column); (iii) a high-pass filter at the first peak of CTF (third column); (iv) a low resolution amplitude correction by multiplying the images amplitudes by the reciprocal of the square root of low resolution averaged CTF (fourth column); (v) a low resolution amplitude correction by multiplying the image amplitudes by the reciprocal of the low resolution averaged CTF (fifth column). The images were phase flipped before any CTF amplitude modification. (**C**) The power spectrum of resulted images. (**D**) The 3D maps reconstructed from the images. The maps are displayed at two different contour levels in the first row (high contour level in cyan and low contour level in gray mesh), with antibody portion shown in pink. The cut-away surface views of the maps at the two contour levels are shown in the second and third rows. (**E**) The FSC curves between the maps without and with amplitude modification. Scale bars: 20 nm.

#	EMDB#[1]	TEM[2]	CCD[3]	Mag.	Apix[4] (Å)	Dose/img.[5] ($e^-/Å^2$)	Dose/set[6] ($e^-/Å^2$)	Acq. angle range[7]	Total img.[8]	Reconst. angle range[9]	Cont.[10]	Resol.[11] (nm)	Fig. [12]
1	EMD-9069	Zeiss 120	UltraScan	50 kX	2.4	1.38	56.38	-60˚ to +60˚	41	-48˚ to +54˚	0.016	9.7	Fig. 2
2	EMD-9070	Zeiss 120	UltraScan	50 kX	2.4	1.45	59.51	-60˚ to +60˚	41	-48˚ to +54˚	0.016	9.6	Fig. 2
3	EMD-9071	Zeiss 120	UltraScan	50 kX	2.4	1.40	57.55	-60˚ to +60˚	41	-48˚ to +54˚	0.009	8.3	Fig S2
4	EMD-9072	Zeiss 120	UltraScan	50 kX	2.4	1.39	56.90	-60˚ to +60˚	41	-48˚ to +54˚	0.135	8.6	Fig S3
5	EMD-9073	Zeiss 120	UltraScan	50 kX	2.4	1.39	56.80	-60˚ to +60˚	41	-48˚ to +54˚	0.012	8.3	Fig S4
6	EMD-9074	Zeiss 120	UltraScan	50 kX	2.4	1.37	56.02	-60˚ to +60˚	41	-48˚ to +54˚	0.014	8.6	Fig S5
7	EMD-9075	Zeiss 120	UltraScan	50 kX	2.4	1.44	59.04	-60˚ to +60˚	41	-48˚ to +54˚	0.018	6.3	Fig. S6
8	EMD-9076	Zeiss 120	UltraScan	50 kX	2.4	1.41	57.82	-60˚ to +60˚	41	-48˚ to +54˚	0.147	9.4	Fig. S7
9	EMD-9077	Zeiss 120	UltraScan	50 kX	2.4	1.36	55.62	-60˚ to +60˚	41	-48˚ to +54˚	0.015	8.3	Fig. S8
10	EMD-9078	Zeiss 120	UltraScan	50 kX	2.4	1.39	56.85	-60˚ to +60˚	41	-48˚ to +54˚	0.010	8.2	Fig. S9
11	EMD-9079	Zeiss 120	UltraScan	50 kX	2.4	1.39	57.00	-60˚ to +60˚	41	-48˚ to +54˚	0.098	6.9	Fig. S10
12	EMD-9080	Zeiss 120	UltraScan	50 kX	2.4	1.37	56.26	-60˚ to +60˚	41	-48˚ to +54˚	0.109	10.0	Fig. S11
13	EMD-9081	Zeiss 120	UltraScan	50 kX	2.4	1.42	58.35	-60˚ to +60˚	41	-48˚ to +54˚	0.076	6.7	Fig. S12
14	EMD-9082	Zeiss 120	UltraScan	50 kX	2.4	1.44	59.16	-60˚ to +60˚	41	-48˚ to +54˚	0.011	7.6	Fig. S13
15	EMD-9083	Zeiss 120	UltraScan	50 kX	2.4	1.43	58.52	-60˚ to +60˚	41	-48˚ to +54˚	0.015	9.3	Fig. S14
16	EMD-9084	Zeiss 120	UltraScan	50 kX	2.4	1.43	58.50	-60˚ to +60˚	41	-48˚ to +54˚	0.010	7.2	Fig. S15
17	EMD-9085	FEI TF20	K2 Summit	19 kX	3.7	1.12	90.49	-60˚ to +60˚	81	-60˚ to +60˚	0.234	6.7	Fig. 4
18	EMD-9086	FEI TF20	K2 Summit	19 kX	3.7	1.11	89.86	-60˚ to +60˚	81	-60˚ to +60˚	0.287	6.2	Fig. 4
19	EMD-9087	FEI TF20	K2 Summit	19 kX	3.7	1.11	90.06	-60˚ to +60˚	81	-60˚ to +60˚	0.270	5.8	Fig. S16
20	EMD-9088	FEI TF20	K2 Summit	19 kX	3.7	1.13	91.24	-60˚ to +60˚	81	-60˚ to +57˚	0.213	6.0	Fig. S17
21	EMD-9089	FEI TF20	K2 Summit	19 kX	3.7	1.12	90.76	-60˚ to +60˚	81	-60˚ to +60˚	0.100	6.0	Fig. S18
22	EMD-9090	FEI TF20	K2 Summit	19 kX	3.7	1.12	91.00	-60˚ to +60˚	81	-60˚ to +60˚	0.134	5.8	Fig. S19
23	EMD-9091	FEI TF20	K2 Summit	19 kX	3.7	1.12	90.75	-60˚ to +60˚	81	-60˚ to +60˚	0.157	5.9	Fig. S20
24	EMD-9092	FEI TF20	K2 Summit	19 kX	3.7	1.12	90.53	-60˚ to +60˚	81	-60˚ to +60˚	0.193	6.1	Fig. 5
25	EMD-9093	FEI TF20	K2 Summit	19 kX	3.7	1.11	90.30	-60˚ to +60˚	81	-60˚ to +58.5˚	0.143	5.8	Fig. S21
26	EMD-9094	FEI TF20	K2 Summit	19 kX	3.7	1.11	89.82	-60˚ to +60˚	81	-60˚ to +45˚	0.154	6.9	Fig. S22
27	EMD-9095	FEI TF20	K2 Summit	19 kX	1.85	1.12	90.87	-60˚ to +60˚	81	-54˚ to +54˚	0.247	6.0	Fig. 5
28	EMD-9096	FEI TF20	K2 Summit	19 kX	1.85	1.13	91.66	-60˚ to +60˚	81	-51˚ to +58.5˚	0.216	5.7	Fig. S23
29	EMD-9097	FEI TF20	K2 Summit	19 kX	1.85	1.12	90.55	-60˚ to +60˚	81	-49.5˚ to +45˚	0.216	5.8	Fig. S24
30	EMD-9098	FEI TF20	K2 Summit	19 kX	1.85	1.10	89.48	-60˚ to +60˚	81	-52.5˚ to +48˚	0.239	6.1	Fig. S25
31	EMD-9099	FEI TF20	K2 Summit	19 kX	1.85	1.11	89.60	-60˚ to +60˚	81	-51˚ to +49.5˚	0.214	5.8	Fig. S26
#	EMDB#[1]	TEM[2]	CCD[3]	Mag.	Apix[4] (Å)	Dose/img.[5] ($e^-/Å^2$)	Dose/set[6] ($e^-/Å^2$)	Acq. angle range[7]	Total img.[8]	Reconst. angle range[9]	Cont.[10]	Resol.[11] (nm)	Fig. [12]

[1] EMDB Index: https://www.ebi.ac.uk/pdbe/emdb/
[2] TEM model: FEI TF20 stands for FEI TF200 TEM; Zeiss 120 stands for Zeiss Libra 120 Plus TEM
[3] CCD: K2 Summit stands for Gatan K2 Summit Direct Detector; UltraScan stands for Gatan UltraScan 4000 4Kx4K CCD
[4] Angstrom per pixel
[5] Dose used for each CCD frame
[6] Dose used for whole tilt series
[7] Data acquisition angle range
[8] Total images in the tilt series
[9] Reconstruction angle range
[10] Contour used for display
[11] IPET 3D reconstruction resolution
[12] The process of IPET 3D reconstruction shown in Figure